Optimization Based Analysis of Desalination Technologies for Unconventional Oil and Gas Produced Water Treatment

by

Elmira Mohammadi Shamlou

B.S. Mining Engineering, University of Tehran, 2010

M.S. Mining Engineering, University of Tehran, 2014

Submitted to the Graduate Faculty of the

Swanson School of Engineering in partial fulfillment

of the requirements for the degree of

Doctor of Philosophy

University of Pittsburgh

2022

UNIVERSITY OF PITTSBURGH

SWANSON SCHOOL OF ENGINEERING

This dissertation was presented

by

Elmira Mohammadi Shamlou

It was defended on

November 23, 2021

and approved by

Mahmoud M. El-Halwagi, Ph.D., Professor, Department of Chemical Engineering, Texas A&M University

Carla Ng, Ph.D., Assistant Professor, Department of Civil and Environmental Engineering, University of Pittsburgh

Radisav Vidic, Ph.D., Professor, Department of Civil and Environmental Engineering, University of Pittsburgh

Dissertation Director: Vikas Khanna, Ph.D., Associate Professor, Department of Civil and Environmental Engineering, University of Pittsburgh

Optimization Based Analysis of Desalination Technologies for Unconventional Oil and Gas Produced Water Treatment

Elmira Mohammadi Shamlou, PhD

University of Pittsburgh, 2022

Hydraulic fracturing of shale oil and gas reservoirs is associated with significant environmental sustainability issues regarding water management. Large volume of water, known as produced water, with relatively high total dissolved solids (TDS), is produced during well production. Difficult to treat, these hypersaline brines could contaminate surface freshwater resources and ground water reservoirs. Advanced desalination technologies offer a promising way to provide fresh water while treating the hypersaline produced water. However, the overall performance of desalination systems operating with hypersaline brines has not been thoroughly studied using systems-level approaches. As such, it is necessary to address this knowledge gap by comprehensive analysis of technologies deemed suitable for produced water treatment.

This work investigates the technoeconomic feasibility of several well-established as well as novel technologies for treatment of produced water. This is accomplished through module scale mathematical modeling of thermodynamic processes and technoeconomic nonlinear programming optimization. The technologies studied include 1) air gap, direct contact, permeate gap, conductive gap, sweeping gas, and vacuum membrane distillation (MD) systems, 2) single effect, backward feed, forward feed, and parallel feed multi-effect mechanical vapor recompression (MVR) systems, and 3) brine reflux, consecutive loops, split feed, and cascading osmotically assisted reverse osmosis (OARO) systems.

This work show that air gap MD has the lowest treatment cost of all MD configurations when the gap size is small, and the Reynolds number is low. For OARO systems, brine-reflux configuration outperforms all others in terms of cost, energy consumption, and design simplicity. Additionally, single effect MVR outperforms multi-effect MVR when the temperature difference across the evaporator is well constrained. Across the studied technologies, brine reflux OARO has the smallest work of separation, followed by air gap MD and MVR. However, brine reflux OARO requires significant investment and replacement of large-area membranes, whereas airgap MD is the least expensive in terms of capital costs. MVR is also associated with high capital costs of compressor and evaporator. Under ideal operating conditions, air gap MD has the lowest cost for produced water treatment. Furthermore, when operational complexities are considered, or feed is at lower salinities, alternative technologies may offer more viable options.

Table of Contents

List of Tables

List of Figures

Dedicated to

my beloved parents, Maryam and Alireza

and my lovely husband, Arash

Acknowledgements

First and foremost, I must thank Dr. Vikas Khanna for being the best advisor a PhD student could hope for. He allowed me to be independent in my research while always keeping an eye on my progress. He always encouraged and supported my curiosity to investigate various desalination technologies, and his detailed and insightful comments on my papers significantly improved my work. Then I'd like to thank Dr. Radisav Vidic for introducing me to the fascinating world of desalination technologies. When I applied for this PhD, I had no idea about membrane distillation or other advanced desalination systems. During my first semester at Pitt, Dr. Vidic introduced me to their joint group with Dr. Khanna working on membrane distillation, and he has remained an excellent mentor since then.

I'd also like to thank Dr. Mahmoud El-Halwagi for excellent collaboration on the RAPID project, which taught me a great deal and opened another door for further exploration of the desalination world. Additionally, I would like to thank Dr. Carla Ng for her insightful comments and inquiries on my PhD proposal, which pushed me to improve the work.

My heartfelt gratitude goes to my mother and father, Maryam Miresmaeili and Alireza Shamlou for their unwavering love and support over the years. A huge thank you to my brilliant mother, the strongest woman I know, who supported me throughout these years while she fought and defeated cancer without ever telling me anything about her situation and without having me by her side. She has always been a source of inspiration for me. Huge thanks to my father for his extraordinary support of my mother every step of the way she battled her disease. I also owe a debt of gratitude to my brilliant and intelligent father for instilling in me a computer programming and algorithm mindset since childhood which I’m still benefiting from today. I'd also like to thank my

beautiful and loving sister, Elnaz Shamlou, and my amazing brother-in-law, Pourya Saati, for always being there for me. A special thanks also goes to my adorable little nephew, Aria Saati, whose birth has made the world a more beautiful place. Finally, a heartfelt thank you to my love and my best friend, my beloved husband, Arash Samiei, for making me smile everyday, for his never-ending encouragement and for standing by my side throughout these years. I love you all.

Nomenclature

Acronyms

AF	Amortization factor	
BF	Backward feed	
ERD	Energy recovery device	
BPE	Boiling point elevation	℃
FF	Forward feed	
GOR	Gain output ratio	
CC	Capital cost	$\frac{\text{USD}}{\text{m}^3}$
OC	Operating cost	$\frac{\text{USD}}{\text{m}^3}$
LMTD	Log mean temperature difference	
MEE	Multiple effect evaporator	
PF	Parallel feed	
SE	Single effect	
SEC	Specific energy consumption	$\frac{\text{kWh}}{\text{m}^3}$

Roman symbols

A	Area	m^2
a_w	Membrane water permeability coefficient	$\frac{\text{m}^3}{\text{h.m}^2\text{.bar}}$

a_s	Membrane water permeability coefficient	$\frac{m^3}{h.m^2}$
B	MD membrane Permeability	$\frac{kg}{s.m^2.Pa}$
B_0	MD membrane Permeability coefficient	$\frac{kg}{s.m.Pa}$
C	Concentration	$\frac{g}{L}$
C_p	Heat capacity.	$\frac{kJ}{kg.K}$
D	Solute diffusion coefficient	$\frac{m^2}{s}$
D_{ab}	Vapor diffusion coefficient into air	$\frac{m^2}{s}$
d_f	Spacer filament diamater	m
d_h	Membrane channel hydraulic diameter	m
h	enthalpy	$\frac{kJ}{kg}$
h_{conv}	Convection heat transfer coefficient	$\frac{kW}{K.m^2}$
J	MD water flux	$\frac{kg}{s.m^2}$
J_w	OARO water flux	$\frac{m^3}{h.m^2}$
J_s	OARO salt flux	$\frac{kg}{h.m^2}$
L	Membrane length	m
k_{mass}	Mass transfer coefficient	$\frac{m}{s}$

M	Mass flow rate	$\frac{kg}{s}$
m	Molality	$\frac{mol}{kg}$
n	Molar flowrate	$\frac{mol}{s}$
Nu	Nusselt number	
P	Partial pressure	Pa
OP	Osmotic pressure	bar
P_h	hydraulic pressure	bar
P_T	Total pressure	Pa
PD	Pressure drop	$\frac{bar}{m}$
Pr	Prandtl number	
q	Heat flux	$\frac{kW}{m^2}$
R	Universal gas constant	$\frac{J}{mol.K}$
Re	Reynolds number	
Sc	Schmidt number	
Sh	Sherwood number	
T	Temperature	°C
U_{hx}	Overall heat transfer coefficient	$\frac{kW}{Km^2}$
V	Velocity	$\frac{m}{s}$
W	Membrane width	m

X	Salinity (weight percent)	%

Greek symbols

ρ	Density	$\frac{kg}{m^3}$
μ	Viscosity	Pa.s
ΔT	Temperature difference	°C
ΔA	Slice area	m^2
α	Activity coefficient	
δ	Thickness	m
γ	Heat capacity ratio	
η	Efficiency	%
ϵ	Porosity	%
θ	Terminal temperature differences in heat exchangers	°C
φ	Osmotic coefficient	

Subscripts

a	Air side
ave	Average
b	Bulk (for MD and OARO) / Top brine temperature (for MVR)
c	Cold side in MD/ concentrating side in OARO
b	Top brine temperature (effects)
comp	compressor

d	vapor generated in effect (for MVR)/ diluting side (for OARO)
db	vapor generated via boiling
df	vapor generated via flash
evap	evaporator
ch	Chiller
cond	Conduction
conv	Convection
cw	Cooling wall
e	Evaporation
f	Make up feed
ff	Falling film
g	Gap
h	Hot side
hx	Heat exchanger
in	Inlet
l	Liquid
m	Membrane surface
Mix	Mixture of makeup feed and recycle stream
out	Outlet
p	Permeate
pg	Purge
px	Pressure exchanger

rec	Recycle stream
rej	Reject stream
sat	Saturation
sl	Saturated liquid
sp	Spacer
sv	Saturated vapor
v	Vapor
vac	Vacuum side

superscripts

i	Stage number
firsti	First stage
firstz	First slice
lastz	Last slice
lasti	Last stage
z	Slice number

1.0 Introduction

1.1 Shale Oil and Gas Produced Water

Shale oil and gas refers to low-permeability reservoirs that were previously unprofitable to extract prior to development and application of unconventional extraction techniques. In the early 2000s, the introduction of horizontal drilling and advances in hydraulic fracturing transformed the shale oil and gas industry. Horizontal drilling expanded producers' access to reservoirs, and advanced hydraulic fracturing increased oil and gas flow, enabling economically viable shale oil and gas extraction.

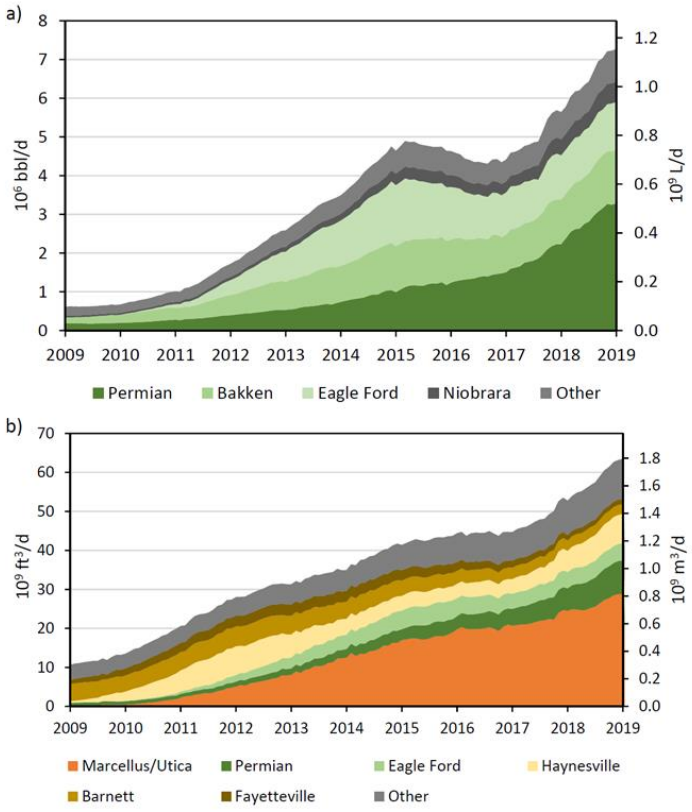

Figure 1. a) Tight oil and b) shale gas production in major US reservoirs [1]

Figure 1 illustrates the explosive growth of shale oil and gas production over the last decade. Unlocking vast quantities of trapped shale oil and gas, US became a net gas exporter in 2015 and the world's largest oil producer in 2018 [2, 3]. Despite significant economic growth, the shale oil and gas industry faces serious sustainability concerns regarding water management, which, if not addressed, could jeopardize future production and result in environmental degradation.

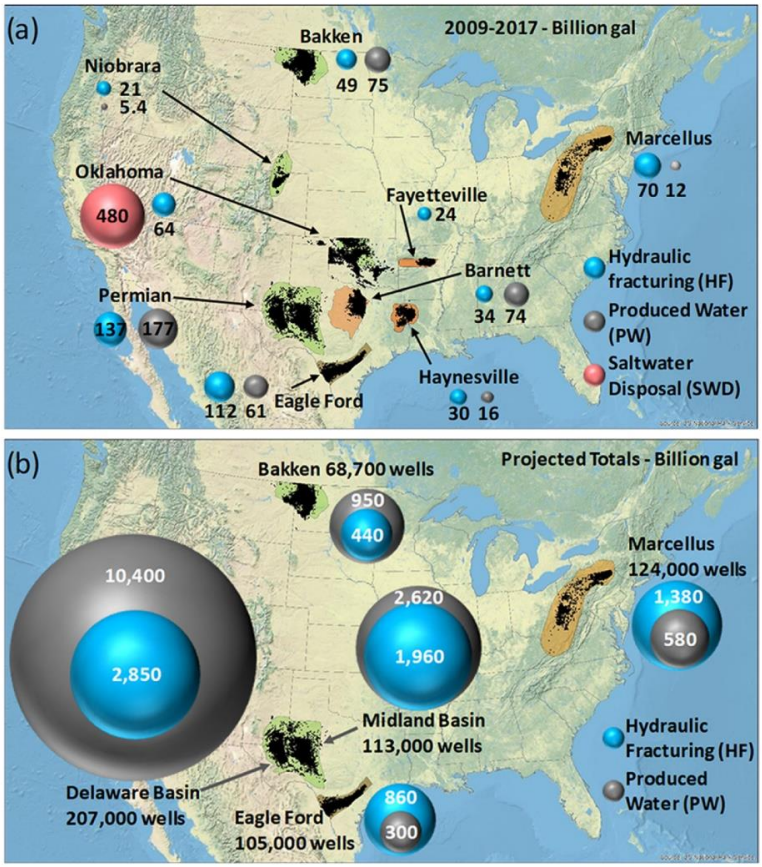

Figure 2. a) Total volume of hydraulic fracturing (HF) and produced water (PW) from major tight oil and shale gas reservoirs during 2009-2017, b) Projected HF and PW from development of remaining technically recoverable resources. [1]

Hydraulic fracturing process utilizes high-pressure fracking water mixed with various additives to crack gas/oil-bearing rock formations, allowing for the flow of gas and brine to the surface [4]. The injected water partially returns to the surface along with the formation water, which is categorized as flowback water and produced water. Flowback water rises to the surface a few days after the fracturing operation begins, initially at a high flow rate and low TDS, and primarily containing injected water components [5]. The water flowrate gradually drops in the months following the start of gas production and continues throughout the well production lifetime; This water is referred to as produced water containing primarily chemicals, organic and inorganic compounds of shale formation rock [6, 7]. Produced water typically has a high salt concentration ranging from 70,000 to 350,000 mg/L of total dissolved solids (TDS) originating from rock formation salts [8].

Figures 2a and 2b depict the current and projected total volume of hydraulic fracturing and produced water resulting from unconventional shale gas and oil resources. For major US plays, the total volume of hydraulic fracturing water ranges from 21 to 137 billion gallons from 2009 to 2017, with a projected increase between 440 to 2850 billion gallons over the production years of remaining technically recoverable resources. This large volume of hydraulic fracturing water could put a strain on freshwater resources and deplete groundwater resources in semi-arid and arid regions. Similarly, the total volume of produced water from 2009 to 2017 ranges between 12 to 177 billion gal and is expected to rise to 300 to 10,400 billion gal during remaining resource production [1]. If not properly managed, this massive amount of produced water with high salinity and toxicity could contaminate aquifers, negatively impact ecological species, soil, and vegetation, and impede the sustainable development of shale oil and gas reservoirs [9-11].

1.2 Produced Water Management Strategies

The current dominant strategy of produced water management is injection into disposal wells. However, this strategy is accompanied by environmental concerns and geological constraints. Reinjecting a large volume of produced water into disposal wells raises pressure within the pores of the rock formation, causing earthquakes in areas where the injection level is connected to the faults. This has been observed most prominently in areas such as Oklahoma, where large amounts of produced water are injected into deep wells [12]. Additionally, in areas with a scarcity of disposal wells, such as the Marcellus shale play, produced water must be transported to areas with a greater density of disposal wells, such as Ohio, incurring a high transportation cost [13, 14].

Recycling and reusing produced water as hydraulic fracturing water is an alternative method of addressing the issues associated with hydraulic fracturing water sourcing and produced water management. In this method, minimally treated produced water is combined with fresh water for re-use in hydraulic fracturing. This option has been utilized in areas such as Marcellus shale play with lower produced water to hydraulic fracturing water ratios [1, 14]. However, as shown in Figure 2, in major shale plays like the Permian, the ratio of produced water to hydraulic fracturing is high, and alternative management strategies are needed alongside a recycling strategy. Furthermore, recycling is accompanied with storage limitation for future reuse, especially when drilling activities are slowed down due to uncertain gas price, or fast depletion of the reservoirs of the region. Additionally, this option is viable if numerous fracking wells are in close proximity to one another so that the produced water can be recycled and reused. Otherwise, distribution of the produced water would be complicated with associated high risk of contamination from spills.

Advanced treatment via desalination technologies may be a viable option as regulations surrounding disposal and recycling tighten and existing strategies become economically and

environmentally unsustainable. Desalination technologies can also provide fresh water for surface discharge or beneficial uses such as irrigation and industrial purpose. Furthermore, desalination can reduce the volume of produced water to that of reject brine making it easier for transportation and disposal via injection. Desalination systems can be used in conjunction with crystallizers to further reduce brine volume and precipitate solid salts, a process known as zero liquid discharge (ZLD). ZLD, which is gaining momentum in academia and industry, has the potential to alleviate environmental concerns associated with industrial wastewater, such as produced water [15, 16].

1.3 Desalination of Hypersaline Brine

While desalination may be a viable option for addressing the high salinity shale gas wastewater problem, the high salinity of the produced water precludes the use of conventional desalination technologies [17]. Conventional distillation methods (e.g. multi-stage flash and multi-effect distillation) are less suitable for small-scale plants with hypersaline feed because of their large footprint, expensive equipment, and high corrosion risk [18, 19]. Similarly, reverse osmosis (RO) is not an effective technology for treating hypersaline brine due to the inability of RO membranes to withstand the required high pressure, as well as the high cost of high pressure pumps and vessels for hypersaline wastewater treatment [20]. Therefore, along with evaluating different management options, there is a need to evaluate applicable existing and emerging desalination technologies to assess their technoeconomic potential for produced water management.

1.3.1 Membrane Distillation (MD)

MD is a desalination technology with a modular design that can treat hypersaline wastewater without the drawbacks associated with most commonly used desalination technologies. MD is a hybrid thermal-membrane separation process that makes use of the difference in vapor pressure caused by temperature gradient across a hydrophobic membrane. The low operating temperature of MD (typically between 40-90^{o}C) makes it ideal for integration with waste heat sources such as flared gas, as well as low temperature and underutilized geothermal energy sources [21-23]. Additionally, MD can achieve rejection factors of 99.9% for salts and 99.5% for organic materials [24-29]. There are several MD configurations (including air gap, permeate gap, and conductive gap, direct contact, vacuum, sweeping gas, and multi effect) as well as several operation modes (single stage and multistage continuous recirculation, batch, and semi batch) that can be used for the desalination process, each with its own distinct set of advantages and disadvantages. Despite some existing published studies on each of the aforementioned configurations, there is a lack of comprehensive analysis for assessing and comparing the performance and technoeconomic feasibility of various MD configurations for produced water management.

1.3.2 Osmotically Assisted Reverse Osmosis (OARO)

Osmotically assisted reverse osmosis (OARO) systems are emerging RO configurations that enable the pressure driven membranes to treat hypersaline solutions [30, 31]. OARO overcomes the problem of excessive hydraulic pressures by introducing a saline solution stream on the low-pressure side of the membrane leading to reduction in transmembrane osmotic pressure

difference [30, 32-34]. Several OARO configurations, such as consecutive loops, split feed, and cascading osmotically mediated reverse osmosis, are commonly discussed in the literature [35-37], each with their own set of advantages, limitations, and complexities. However, detailed investigation of the potential of OARO technology, improvement in configurations, and comparisons with other technologies such as MD is needed.

1.3.3 Mechanical Vapor Recompression (MVR)

MVR is the industry's gold standard for treating hypersaline brines due to its high energy efficiency when compared to conventional thermal desalination processes. MVR recovers heat from the produced vapor via compression and distillation, and thus does not require external heat sources. Additionally, unlike conventional thermal desalination methods, MVR does not require an external condenser or cooling tower and is capable of operating at low vacuum temperatures and pressures [38]. Additionally, MVR can be configured in a variety of multiple effect configurations (backward feed, forward feed, and parallel feed) primarily for the purpose of increasing capacity. Few studies have been published comparing various MVR configurations; however, these studies lack a fair comparison of single- and multi-effect configurations due to their failure to adjust the temperature difference between each individual evaporator within the system. Additionally, there is no study that compares MVR performance to that of other emerging technologies such as MD and OARO for produced water management in a consistent framework.

1.4 Research Objective and Thesis Layout

The main goal of this research is to investigate opportunities for application of emerging technologies in hypersaline produced water desalination. This goal is achieved through techno-economic optimization that provides comprehensive understanding of several desalination technologies and their optimum operating conditions. By setting unit cost of treatment as the optimization objective function, we assess the tradeoffs between capital cost and energy consumption of various systems thus providing a basis to compare performance of these emerging technologies for hypersaline produced water treatment. Through the development of thermodynamic and economic models as well as sensitivity analysis, this work addresses the gaps in the literature regarding the effective parameters on operating condition and performance of these emerging desalination technologies. In addition, this research proposes modifications to configurations to improve the performance of the aforementioned technologies for produced water treatment.

Chapter 2 evaluates and compares the technical and economic performance of direct contact, air gap, permeate gap, conductive gap, sweeping gas, and vacuum MD configurations for shale gas produced water treatment in a single stage continuous recirculation mode. This is accomplished by developing module-scale optimization models for each of the configurations. Additionally, an in-depth analysis of various performance metrics for selected configurations is provided, as well as a discussion of theoretically optimal versus practically relevant MD system design.

Chapter 3 develops optimization models for multi-stage continuous recirculation for all gap types, DCMD, and VMD configurations, taking interstage heating and recirculation into account. The developed optimization models are used to compare and analyze the treatment costs

and energy consumption of various multi-stage MD designs for treating produced water from unconventional reservoirs, as well as ZLD operations. Analyses also provide implications for why recirculation should not be eliminated in multi-stage mode.

Chapter 4 presents brine reflux osmotically assisted RO (BR-OARO) and compares it to commonly discussed configurations. To accomplish this, mathematical models of all OARO configurations are developed at the module scale and their performance is compared using an optimization-based framework in terms of maximum achievable recovery, energy consumption, cost, and membrane requirement for ZLD operation.

Chapter 5 develops mathematical and optimization models for single and multi-effect MVR systems in order to compare treatment costs and energy consumption for produced water treatment. The effect of temperature difference (across the evaporator and the compressor) on the performance of studied configurations is also investigated. Additionally, the impact of recirculating reject brine within the system on energy performance and cost is also examined.

Chapter 6 summarizes the major findings from the optimization analysis conducted in the preceding chapters and compares the energy consumption, treatment cost, and equipment size of MVR, MD, and OARO systems, as well as provides a discussion of the best options for hypersaline brine treatment.

2.0 Optimization-based Economic Comparison of Membrane Distillation Configurations for Application in Shale Gas Produced Water Treatment

Membrane distillation (MD) is an emerging membrane technology with great potential for treatment of hypersaline wastewater generated by unconventional (shale) oil and gas reservoirs. However, the low energy efficiency of this technology makes the operating cost of MD systems relatively high, especially in the absence of waste heat. There are several MD configurations with inherent advantages and disadvantages and varying performance. As such, there is a need for thermo-economic optimization of MD systems in a systematic manner to assess their economic performance. We present an optimization framework to model and compare the performance of six MD configurations (DCMD, AGMD, PGMD, CGMD, SGMD, and VMD) in continuous recirculation mode for treatment of hypersaline wastewater. The optimization results show that AGMD with small gap size operated at low stream Reynolds number outperforms all other configurations with treatment cost of 4.57 US $/m^3 of feed. However, restricting the system design to more practically relevant operating conditions, such as higher Reynolds number and larger gap size, diminishes the cost superiority of AGMD over other configurations. We also observed that treatment cost using PGMD configuration approaches those of CGMD and DCMD, particularly when modules with small gaps are used.

2.1 Introduction

Desalination technologies offer great promise to provide fresh water where natural resources are limited and for treatment of wastewaters and groundwaters of varying salinities while simultaneously protecting the environment and available freshwater reservoirs. Two broad and popular categories of desalination technologies include thermal distillation (e.g. multi-stage flash distillation, multi-effect evaporation) and membrane-based desalination (e.g. reverse osmosis, forward osmosis) [39]. Large footprint, high equipment costs, and risk of material corrosion make conventional thermal distillation methods less suitable for small scale plants with high salinity feed [18, 19]. Similarly, inability of reverse osmosis to handle the high salinity of certain streams (e.g., unconventional oil and gas wastewater) makes it impractical for such applications [20]. High salt concentration, usually between 70,000 and 350,000 mg/L total dissolved solids (TDS) is characteristic of produced water generated by the unconventional oil and gas industry [40]. Flowback and produced water volume from unconventional reservoirs in the United States range between 0.5- 3.8 million gallons per well over the first 5–10 years of production [41]. If not properly managed, wastewater from shale gas production could contaminate aquifers and negatively impact biological species, soil, and vegetation due to elevated level of salinity and toxicity [9-11]. The current dominant strategy in the US for managing shale gas wastewater is injection into underground disposal wells [42, 43]. However, this strategy has limited potential in areas with insufficient disposal wells (e.g. Marcellus shale in Pennsylvania) and has also been linked to induced seismicity [44-46] . As such, there is a need to explore and evaluate technologies for treatment of high salinity wastewaters to ensure the long-term sustainability of this industry. Membrane Distillation (MD) technology is one such promising technology for treatment of high salinity wastewaters [18].

MD is a desalination technology capable of modular design and the ability to treat hypersaline wastewater without the aforementioned drawbacks of most commonly used desalination technologies. MD combines thermal and membrane processes to utilize the difference in vapor pressure induced by a temperature gradient across a hydrophobic membrane. The vapors produced from the preheated feed (usually between 40-90^{o}C) traverse through the microporous membrane and are collected and condensed in various ways depending on the MD configurations [23]. The lower operating temperature of MD compared to other thermal desalination technologies makes it uniquely suited for integration with waste heat sources [14]. Despite the unique advantages of MD, it suffers from low single pass recovery (i.e., maximum of 10% [47]) that impacts the operational mode and design of the system. Batch recirculation and continuous recirculation modes of operation can overcome this limitation [47-49]. With batch operation mode, a certain amount of feed in the circulation tank is sent to the membrane multiple times until the salinity of the feed in the tank reaches a desired level. Although batch operation mode is shown to have better energy efficiency than other recirculation modes [48], such unsteady state operation may not be suitable for large scale or continuous operations [49]. Continuous recirculation is a steady state operation mode in which input feed (makeup) to the system is mixed with comparatively large portion of the membrane reject brine (recycle stream) and the resulting mixed stream is sent to the membrane unit for water recovery. The ratio of recycle stream flowrate to makeup feed flowrate, recycle ratio, is dependent on membrane configuration, design, and energy performance of the system.

Lokare et. al [47] estimated the recycle ratio of the DCMD system for various recoveries and showed that operating in continuous recirculation mode significantly increases the thermal energy demand to heat both the makeup feed and the large volume of recycle stream. In another

study [48], Swaminathan and coworkers demonstrated that the performance of MD systems is negatively impacted by vapor pressure depression caused by the system's increased operating salinity in continuous recirculation mode. Thus, when analyzing MD systems for high recovery applications (e.g., produced water desalination or zero liquid discharge (ZLD)), it is critical to analyze their performance in continuous recirculation mode instead of single pass in order to obtain accurate estimate of the desalination system's cost and energy performance.

MD configurations commonly discussed in the literature include Direct contact (DCMD), air gap (AGMD), permeate gap (PGMD), conductive gap (CGMD), sweeping gas (SGMD), and vacuum (VMD) membrane distillation [50-52]. Each configuration has its own set of advantages and disadvantages that vary according to the application and operating conditions of the process. Multiple previous studies have reported performance metrics in comparative evaluations of MD configurations [53-60]. However, most studies have focused primarily on the effect of system operating conditions on energy efficiency, flux, or energy consumption, without accounting for the tradeoffs between cost and the aforementioned parameters in order to achieve optimal MD design. Several studies have also assessed MD systems from a technoeconomic perspective as a function of feed salinity and water recovery [61-68]. These studies have evaluated the economic and energetic performance of specific types of MD configurations without a formal comparison of different configurations under consistent specifications (e.g., input salinity, water recovery, operation mode, membrane and plant characteristics). Because the estimation of an MD system's economic and technical performance is highly dependent on the assumptions made in a study, a formal optimization-based comparison is required to evaluate the technoeconomic feasibility of various MD configurations within a consistent framework.

We present an optimization-based model to evaluate the technical and economic performance of DCMD, AGMD, PGMD, CGMD, VMD, and SGMD configurations in continuous recirculation mode. The developed optimization models are utilized to compare the treatment costs and energy consumption of different MD configurations for treatment of hypersaline feed and high water recovery applications, such produced water from unconventional reservoirs and ZLD processes. Additionally, we provide an in-depth analysis of various performance metrics for selected configurations along with discussion of theoretically optimal versus practically relevant design of MD systems. Finally, we investigate the effect of feed and concentrate (i.e., reject brine) salinity, inlet temperature, feed channel turbulence, gap size in gap type MD systems, and membrane thickness on the performance of various MD configurations. To the best of our knowledge, this is the first optimization-based study to provide a comprehensive comparative evaluation of all MD configurations from a cost, energy, and practical perspective.

2.2 Methodology

Process Description- Permeation, condensation, recirculation, cooling, preheating, and heating are the five stages in a typical membrane distillation process and are discussed below.

Permeation. Figure 3(a-d) illustrates the continuous recirculation mode of operation for DCMD, AGMD, PGMD, CGMD, SGMD, and VMD. The hot feed from the heater enters the membrane's hot channel. Water vapor permeates the hydrophobic membrane pores due to the vapor pressure difference across the membrane. The vapor pressure on the membrane surface on the hot channel side is a function of the vapor saturation temperature in all configurations. In DCMD, PGMD, and CGMD, the vapor pressure difference is a function of the vapor saturation

temperature gradient across the membrane. Similarly, the vapor pressure differential in AGMD is proportional to the difference in vapor saturation temperature between the hot channel membrane surface and the cooling wall surface. However, in SGMD, the vapor pressure in the air channel depends on the vapor content (humidity ratio) of the air, which may or may not be saturated. *It should be noted that in this study, sweeping gas is assumed to be air, and the terms will be used interchangeably throughout this manuscript*. In VMD, the vapor pressure in the vacuum channel is equal to the applied vacuum pressure.

Condensation. In DCMD, permeated water condenses on the water surface on the cold channel since there is no gap between the cold channel and the membrane. The permeated vapor in AGMD passes through the airgap and condenses on the cooling surface, forming a condensing film. Because the gap in PGMD and CGMD is filled with water, the permeated vapor condenses on the water in contact with the membrane surface as soon as it exits the membrane pores. In SGMD and VMD, moist air and vapor flow to an external condenser for permeate condensation.

***Recirculation*.** In continuous recirculation mode, a significant portion of the brine leaving the membrane unit is recirculated and mixed with the incoming feed, while a small portion exits the system as reject brine.

***Cooling*.** In DCMD, the pure water flow exiting the module's cold channel enters a heat exchanger followed by a chiller to maintain the temperature difference across the membrane. In gap type MD configurations, the recirculating brine is cooled before entering the cold channel via a chiller to maintain the required temperature difference for permeation and condensation. Similarly, the recirculating brine in SGMD passes through a chiller before entering the condenser to provide the required cooling for condensation. In VMD, coolant exiting the condenser enters the chiller to meet the condenser's cooling demand.

Preheating and heating. In DCMD, only pure water may be used as a coolant because permeate condenses on the cold channel, necessitating the use of an external heat exchanger to recover heat from the heated coolant thereby pre-heating the feed. Similarly, in SGMD, the recirculating brine and makeup feed are preheated by routing them through an external condenser. Because all gap type membranes (AGMD, PGMD, CGMD) have separate permeate and cold channels, the feed (a mixture of cooled recirculating brine and makeup feed) can be used as the coolant in the cold channel, recovering heat directly from the hot side of the membrane. In VMD, the temperature of the recycle stream at the module's exit is always greater than the temperature of the vapor on the vacuum side. As a result, no effective heat recovery is possible in the external condenser for the recycle stream and only the low-temperature makeup feed will recover some heat by passing through the external condenser. The VMD's recirculating brine bypasses the chiller and flows directly into the heater.

a)

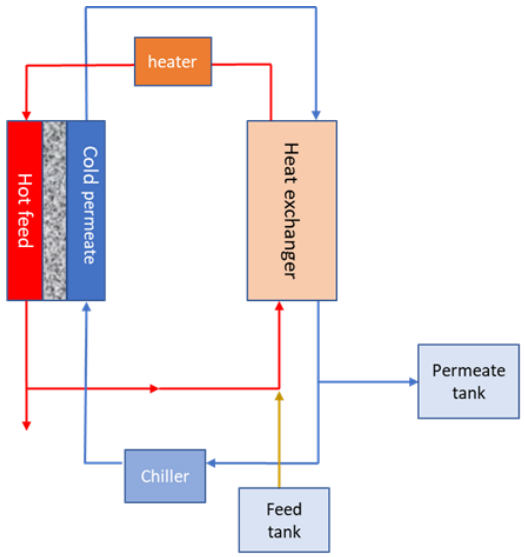

b)

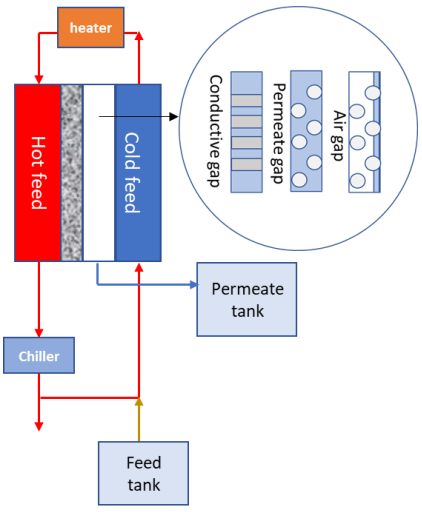

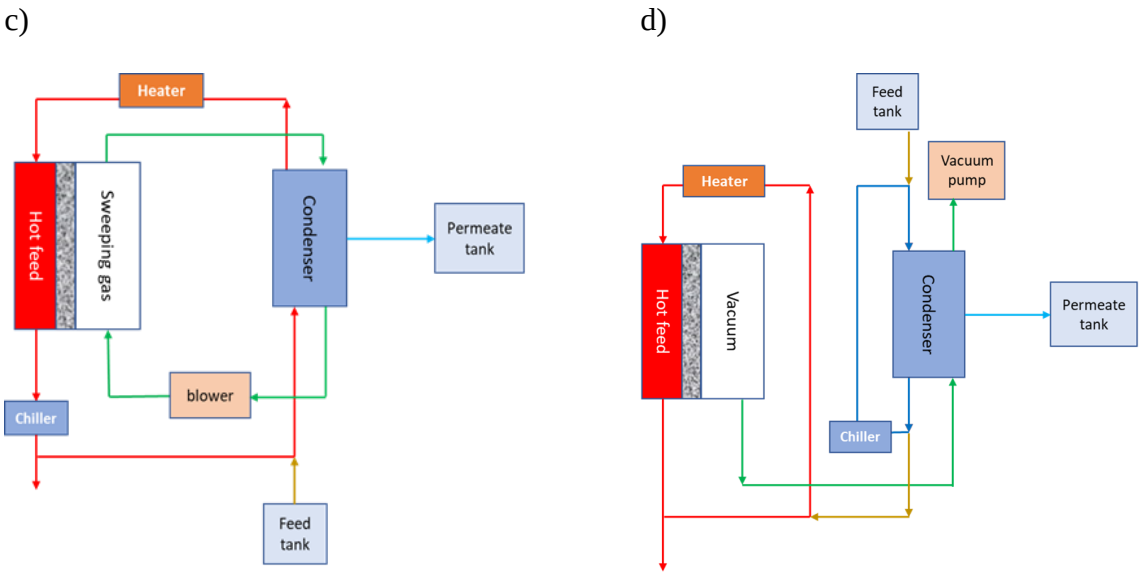

Figure 3. Membrane distillation configurations in single stage continuous recirculation operation mode: a) DCMD, b) Gap type MD, c) SGMD, d) VMD

Optimization model description- For each membrane configuration, the optimization model incorporates the governing thermodynamic processes as equality and inequality constraints. This model is expressed as a nonlinear programming problem with the objective of minimizing the total cost of treated produced water for a given recovery:

$$\min \mathrm{TUC}\,(y), y = (T, M, X)^{T} \in \mathbb{R}$$

$$\text{s.t.} \quad \varphi(y) = 0$$

$$\psi(y) \leq 0$$

Temperature, salinity, and flowrate of all streams are independent variables to optimize, while recirculation ratio, total membrane area, module length and width, heat exchanger and condenser total area, required heating steam, chilling energy, and pumping energy are dependent variables. It should be noted that in our initial optimization models, we entered membrane thickness as a constant parameter and used one of the commercially available membranes with a

known permeability coefficient [69]. However, in order to investigate the effect of membrane thickness on treatment costs, we performed a second round of optimization with membrane thickness as one of the variables to be optimized:

$$\min \mathrm{TUC}\,(y), y = (T, M, X, \delta_m)^T \in \mathbb{R}$$

$$s.t. \quad \varphi(y) = 0$$

$$\psi(y) \leq 0$$

We assume that all configurations operate at steady state and heat loss in equipment is negligible. It is assumed that permeate exits the membrane pores with zero salinity. Additionally, we assume that film gravitational condensation occurs in the airgap for AGMD configuration. The optimization problem in this study is solved using the General Algebraic Modeling (GAMS) software and the local solver CONOPT4 [70].

2.2.1 Modelling Membrane Distillation Process

To model large-scale modules, each membrane module is divided lengthwise into a number of slices and mass and energy balances are established for each slice. This section will outline the general structure of heat and mass transfer in the membrane distillation process. The detailed equations and correlations used to model each type of MD configuration are summarized in the appendix in tables 6- 8.

The permeability coefficient and pressure difference across the membrane determine the mass flux through each slice (Equation 1).

$$J^z = B\Delta p^z \qquad \forall z \in Z \tag{1}$$

The mass change along each slice of the hot channel is proportional to the area of the slice and the mass flux (Equation 2).

$$\Delta M^z = -J^z \Delta A^z \qquad \forall\, z \in Z \tag{2}$$

The mass change along the cold channel is determined by whether or not the cold channel receives permeate. The flowrate along the cold channel does not change in the gap MD configuration, but it changes in the DCMD, VMD, and SGMD configurations as shown in Equation 3.

$$\Delta M^z = J^z \Delta A^z \qquad \forall\, z \in Z \tag{3}$$

As no salt passes through the membrane, the absolute mass of salt along the hot channel remains constant while concentration varies from the inlet to exit (Equation 4).

$$\Delta M^z X^z = 0 \qquad \forall\, z \in Z \tag{4}$$

Convection heat transfer occurs through cold and hot channels, while various combination of evaporation and conduction heat transfer occurs through intermediate channels. The convective heat transfer coefficient is used to estimate convective heat flux, and the thermal conductivity and thickness of the heat transfer medium are used to calculate conduction heat flux (Equations 5 and 6).

$$q^z_{conv} = h^z(\Delta T^z) \qquad \forall\, z \in Z \tag{5}$$

$$q^z_{cond} = \frac{k}{\delta}(\Delta T^z) \qquad \forall\, z \in Z \tag{6}$$

The evaporative heat flux is proportional to the mass flux and enthalpy of evaporation (Equation 7)

$$q_v^z(T) = J^z H_v^z(T) \qquad \forall\, z \in Z \tag{7}$$

where,

$$H_v^z(T) = H_{sl}^z(T) + H_e^z(T) \qquad \forall\, z \in Z \tag{8}$$

The enthalpy change along each slice of the cold and hot channel is proportional to the convective heat flux and area of the slice (equation 9)

$$M^z \Delta H^z = q_{conv}^z \Delta A^z \qquad \forall\, z \in Z \tag{9}$$

2.2.2 Performance Measurement Criteria

Several performance criteria are used in this work to compare the performance of various MD configurations and are described below.

Gain output ratio, thermal efficiency, and energy recovery. The gain output ratio (GOR) is a measure of a desalination system's thermal energy performance. It is defined as the ratio of the total heat of permeate evaporation to the total heat of consumed steam (Equation 10).

$$GOR = \frac{\sum_z q_{v_z}}{Q_s} = \frac{\sum_z M_{p_z} h_{v_z}}{M_s h_{v_s}} \tag{10}$$

GOR is dependent on the thermal efficiency (η_{th}) and heat recovery ratio (HR) of MD systems. The thermal efficiency (Equation 11) of a membrane is defined as the ratio of the total enthalpy of the permeated vapor to the total heat transferred across the membrane (Q_t):

$$\eta_{th} = \frac{\sum_z q_{v_z}}{Q_t} = \frac{\sum_z q_{v_z}}{\sum_z (M_{p_z} h_{v_z} + q_{v_z})} \quad (11)$$

The overall heat recovery ratio is defined as the ratio of total heat recovered within the MD system to total heat consumed for separation (which is the sum of heat recovered and external heat of steam):

$$HR_{overall} = \frac{Q_{HR}}{Q_{HR} + Q_s} \quad (12)$$

The heat recovery ratio within the MD module is defined as the ratio of heat recovered by the MD's cold channel flow to total heat consumed for separation:

$$HR_{MD} = \frac{Q_t}{Q_{HR} + Q_s} \quad (13)$$

The heat recovered in AGMD, CGMD, and PGMD systems with direct heat recovery is equal to the total heat transferred through the membrane ($Q_{HR} = Q_t$, and $HR_{overall} = HR_{MD}$). In DCMD and SGMD systems with external heat exchangers for heat recovery, the heat recovered is equal to the heat transferred through the heat exchanger. ($Q_{HR} = Q_{hx}$, and $HR_{overall} = HR_{MD} \frac{Q_{hx}}{Q_t}$). For systems with insignificant heat recovery, such as VMD configuration considered in this study, the total heat transferred through the membrane is almost equal to the total heat of steam ($Q_t \sim Q_s$). This is especially true when the recycle stream flowrate is high in comparison to the makeup feed flowrate in VMD. By combining equations 10- 13, and defining the external heat recovery factor as ($f_{hx} = \frac{Q_{hx}}{Q_t}$)we obtain the following:

$$GOR = \eta_{th} \frac{Q_t}{Q_s} \quad (14)$$

$$\mathrm{GOR}\begin{cases} = \eta_{th}\frac{HR}{1-HR} & \text{for AGMD, PGMD, and CGMD} \\ = \eta_{th}\frac{HR_{MD}}{1-f_{hx}HR_{MD}} & \text{for DCMD and SGMD} \\ \sim \eta_{th} & \text{for VMD} \end{cases} \quad (15)$$

In the remainder of this analysis, we will refer to the overall heat recovery ratio as the heat recovery ratio, and the above equations were developed solely to illustrate the relationship between the GOR, the heat recovery ratio, and the thermal efficiency.

Recovery Ratio and single pass recovery ratio: The recovery ratio (RR) is defined as the ratio of permeate production to the system's makeup feed flowrate (Equation 16). Single pass recovery (SPR) is defined as the ratio of permeate production to total input feed to the MD module, i.e. recycle stream plus makeup feed (Equation 17).

$$RR = \frac{\sum_z M_{p_z}}{M_f} \quad (16)$$

$$SPR = \frac{\sum_z M_{p_z}}{M_f + M_{rec}} \quad (17)$$

Recycle ratio is defined as the ratio of the recycle stream to the input makeup feed (Equation 18).

$$RecR = \frac{M_{rec}}{M_f} \quad (18)$$

The specific area of a membrane is defined as the area of the membrane per unit mass of feed entering the MD module (Equation 19).

$$A_s = \frac{A_t}{M_{rec} + M_{rec}} \quad (19)$$

2.3 Results and Discussion

The optimization model is applied for a hypothetical produced water treatment plant with a treatment capacity of 10 kg/s (~0.25 million gallons per day), concentrating produced water with 10% (100,000 mg/Liter) TDS to brine with 30% TDS corresponding to saturation conditions to make the system capable of integration with crystallizers for ZLD operation. The model input parameters, including plant characteristics, membrane properties, and capital and operating cost data, are provided in Tables 1 to 5 in the Appendix.

Treatment cost. Figure 4a shows a comparison of the produced water treatment cost obtained from the optimization model for the studied MD configurations. AGMD outperforms all other configurations with \$4.57/m^3_{feed} treatment cost followed by CGMD, DCMD, VMD, SGMD, and PGMD with 7.8, 8.7, 9.8, 11.63, and 24.11\$/m^3_{feed}, respectively. The operating cost accounts for the majority of the total treatment cost and is the primary reason for treatment cost differences across configurations. Energy costs for heating and cooling are the two largest components of operating costs (Appendix Table 9). DCMD and SGMD have the highest capital costs, followed by PGMD, CGMD, AGMD, and VMD. The high capital cost of DCMD and SGMD is primarily due to the large surface area external heat exchanger and condenser, respectively. DCMD also has a relatively high installation cost because it has two separate loops with high flowrates for the cold and hot sides. The chiller and installation costs account for the largest share of the PGMD relatively high capital cost because of the high recycle stream flowrate. The membrane cost is a significant component of the AGMD and CGMD capital costs with AGMD requiring large area and CGMD with expensive conductive material. Among all configurations, VMD with small membrane area, small condenser surface area, and low recycle stream flowrate has the lowest capital cost. It is worth noting that we assumed that complete condensation occurs in the external condenser of the

VMD. As a result, the vacuum pump removes only non-condensable gases, resulting in a negligible vacuum pump operating and capital cost in comparison to other cost components.

It is worth noting that we assumed the price used for heat exchanger to be applicable to the conductive material filling per unit of area. Accurate cost estimate for conductive materials suitable for CGMD application is necessary and should be studied in the future. Conductive filling materials include metal mesh, metal foam, and finned plate. Metal mesh is ineffective because it does not increase conductivity to the levels considered in this study. Metal foams are also extremely costly and the conductive material assumed in this study is finned plate and has been tested previously [51]. Furthermore, the material and cost of the condenser in SGMD and VMD are assumed to be identical to those of the metal plate and frame heat exchanger. Alternative materials (e.g. plastics) and dehumidifiers with innovative designs [71, 72] could offer the potential to lower costs and should be investigated in future studies.

Flux and total membrane area. The operating flux and total membrane area of the studied membrane configurations corresponding to their lowest treatment cost are shown in Figure 4b. With the largest membrane area, AGMD has the lowest flux of 2.1 L/hr/m^2 (LMH), while VMD and DCMD with lowest membrane areas have the highest fluxes of 14.6 and 12.8 LMH, respectively. The maximum salinity at the membrane interface is set to 30 % for modeling purposes to prevent oversaturation due to concentration polarization. As a result, the maximum operating flux of each MD configuration is constrained by the concentration polarization, which is determined by the hot channel flow Reynolds number. This is particularly important in applications where MD works at high salinities, such as the ZLD condition studied here.

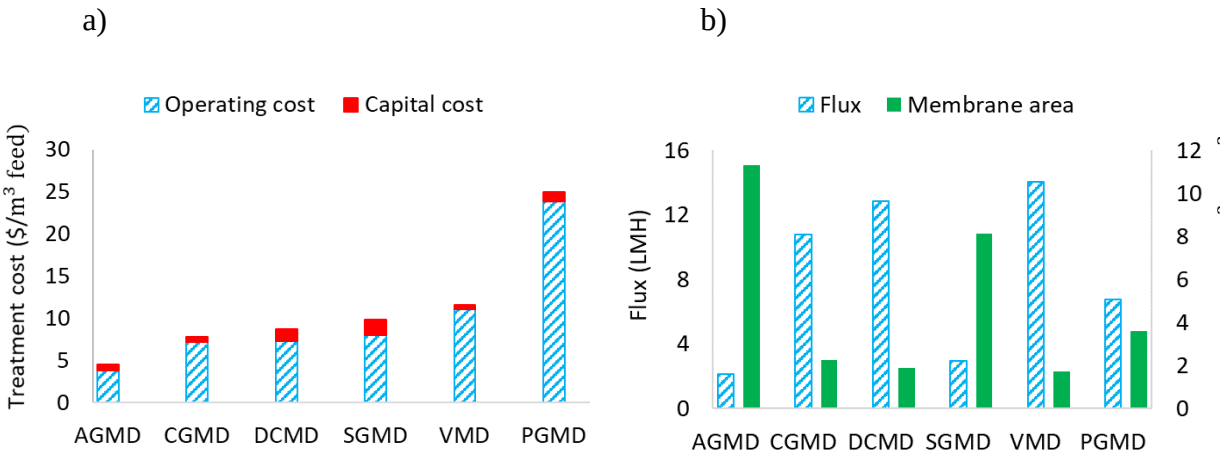

Figure 4. Treatment cost, flux and total membrane area for cost optimal design

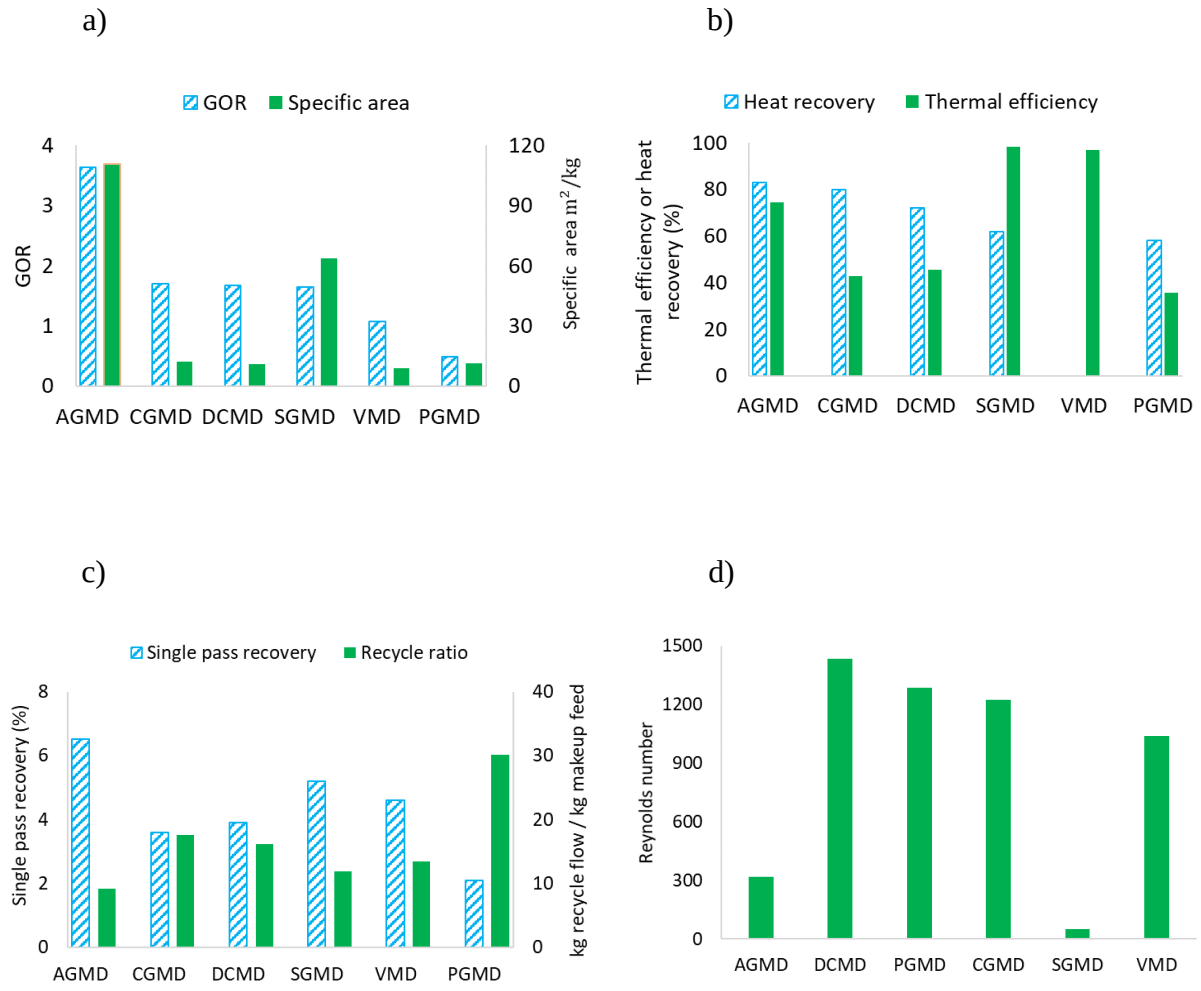

Figure 5. Performance metrics for cost optimal design: a) GOR and specific area, b) Thermal efficiency and heat recovery, c) Single pass recovery and recycle ratio, d) Hot channel Reynolds number

GOR and specific area. The GOR and specific area for the studied MD configurations are shown in Figure 5a. The energy consumption in MD systems is directly proportional to their GOR, and systems with higher GOR have lower heating and cooling costs. AGMD with a GOR of 3.6 has the best energy performance, while PGMD with a GOR of 0.5 shows the lowest energy performance among all MD configurations. The GOR is governed by the thermal efficiency and energy recovery of the MD systems, both of which depend on the membrane specific area and heat and mass transfer resistance through membrane channels. Specific area is an indicator of optimum

area for heat and mass transfer per unit mass flowrate through the hot channel. Unlike total membrane area, specific area is unaffected by plant capacity or recycle ratio, making it easier to compare the energy performance of different MD systems. For example, despite having a significantly larger total membrane area than DCMD, CGMD, and VMD, PGMD has roughly the same specific area as these configurations. Except for the VMD configuration, higher specific area results in greater energy recovery and lower thermal efficiency, resulting in a specific area with a unique combination of thermal efficiency and energy recovery that yields the highest GOR [54]. When minimizing the total unit cost of the system, the obtained optimum specific area is influenced by the tradeoff between membrane cost, pump cost (or blower cost in the case of SGMD), and GOR (corresponding to steam cost).

Thermal efficiency and heat recovery. Figure 5b shows the thermal efficiency and overall heat recovery for the lowest treatment cost for the six MD configurations. As previously stated, there is insignificant heat recovery in the VMD module when operating in single stage continuous recirculation mode, and its GOR is approximately equal to the system's thermal efficiency. The highest thermal efficiency is achieved by VMD, SGMD, and AGMD due to their air and vacuum channels, which limit heat conduction. Although both AGMD and SGMD have air channels, AGMD has slightly lower thermal efficiency than SGMD because: 1) AGMD has larger membrane area with lower average temperature difference across the module, 2) sweep gas in SGMD is not always saturated along the module, and evaporation in this module is not always a function of saturation temperature, which is affected by module size, and 3) SGMD has lower mass transfer resistance than AGMD because of the sweep gas flow.

The design of an AGMD system is primarily affected by the trade-off between membrane cost, pumping cost, and steam cost. The high thermal efficiency and mass transfer resistance in

AGMD make it possible to operate with large specific area and low flux, resulting in relatively high energy recovery and the highest GOR among other configurations.

Because CGMD and DCMD have lower mass transfer resistance and lower thermal efficiency than AGMD, these configurations achieve slightly lower heat recovery with relatively smaller specific areas and higher flux. The higher thermal efficiency of AGMD compared to CGMD and DCMD also results in a significantly higher GOR, more than twice that of CGMD and DCMD.

DCMD has slightly higher thermal efficiency with slightly lower heat recovery than CGMD, but they both produce roughly the same GOR. The conductive gap channel causes slight temperature increase on the condensation surface in CGMD, resulting in lower thermal efficiency compared to DCMD. In comparison to CGMD, DCMD suffers from an external heat exchanger with large surface area (∼4 times the membrane area in this study) and high capital cost, resulting in lower heat recovery ratio. However, DCMD has two advantages that compensate for the limited heat recovery in the external heat exchanger, resulting in the same GOR as CGMD for the cost-optimal design: 1) The hot brine at the module exit is not cooled by a chiller in DCMD resulting in a lower total heat (external steam plus recovered heat) required for the separation process, and 2) Unlike gap type MD configurations, DCMD has a degree of freedom on the cold (permeate) side flowrate, which need not be equal to the hot side stream flowrate. It has been argued previously that for single pass DCMD, the ratio of cold to the hot side flowrate has an important role in optimum performance of MD system [73]. Low flowrate ratios are associated with a rapid rate of temperature change on the cold side, limiting mass transfer along the DCMD module, while high flowrate ratios are associated with a slow rate of temperature change on the cold side, limiting heat recovery in the external heat exchanger. For the specified operating conditions in this study,

the analysis shows that the optimum cold side to hot side inlet flowrate ratio for DCMD in continuous recirculation mode is 0.79. Increasing the flowrate ratio from 0.79 to 1 for DCMD (as in gap MD configurations) has a negative impact on system performance, resulting in a 22% reduction in GOR and an 18% increase in total treatment cost. This is mainly because at higher flowrate ratio, the increase in cold side temperature is lower which results in smaller terminal temperature difference in the heat exchanger for higher heat recoveries. Further, the high capital cost of heat exchanger at higher flowrate ratio limits heat recovery in a cost-optimal design, resulting in lower GOR and higher cost.

While PGMD has comparable specific area to DCMD and CGMD, it has lower thermal efficiency and heat recovery. This is because the condensation surface in PGMD is at the interface of permeate gap and membrane. The permeate gap serves as an additional heat resistance layer between the condensation surface and the coolant channel. As a result, the saturation temperature and pressure on the PGMD condensation surface increase, while the average temperature difference across the membrane decreases, resulting in a reduction in both thermal efficiency and heat recovery. This also explains why adding conductive material to CGMD or eliminating the gap in DCMD improves thermal efficiency and heat recovery when compared to PGMD. Additionally, VMD with minimal heat recovery (exclusively via makeup feed) has a higher GOR than PGMD with heat recovery. This is because VMD has a significantly higher thermal efficiency across the module's length than PGMD. The detrimental effect of liquid gap on PGMD thermal efficiency is more pronounced at the studied reject brine salinity of 30% and membrane thickness of 60 micrometer. This is described in greater detail in the sub-section on brine salinity and thickness analysis.

While SGMD has a similar GOR to DCMD and CGMD at its lowest cost design, it has a higher treatment cost than DCMD and CGMD due to the condenser capital cost and blower operating cost. The optimum design of SGMD is primarily influenced by the tradeoff between blower, condenser, and steam costs. The amount of steam consumed is inversely proportional to the amount of heat recovered within the external condenser. Heat transfer and heat recovery in the condenser for SGMD configuration are dependent on the sweep gas temperature, which has a direct effect on the cost of the condenser via the terminal temperature difference. The convective heat transfer coefficient of air flow is low, and vapor flux condensation occurs primarily outside the membrane module in the condenser, resulting in slow temperature rise for air along the module. The amount of temperature rise in the sweep gas is determined by the membrane area and the air flow convective heat transfer coefficient, which is directly linked to the air flow Reynolds number. Higher Reynolds numbers for air flow, on the other hand, translate to higher blower costs. As a result, SGMD operate over large membrane areas and low air flow Reynolds numbers. This has the benefit of reducing steam consumption by allowing the air to be effectively humidified and heated while avoiding the high capital and operating costs associated with condensers and blowers.

We observe that the optimal ratio of hot channel (feed) to air channel flowrate is 4.6. Higher flowrate ratios than the optimum ratio will reduce GOR because the temperature change in the hot feed flow in both the module and the external condenser will be lower, limiting the heat recovery ratio in the SGMD. Lower flowrate ratios also have a negative impact on system cost by increasing the cooling requirement for external condensation due to the smaller volume of water.

Recycle ratio and single pass recovery. The recycle ratio for all configurations is determined by the single pass recovery (SPR) and the total desired water recovery. Figure 5c illustrates the optimal SPR and recycle ratio for each configuration in order to achieve the target

recovery of 67 percent (final brine salinity of 30 percent). All MD configurations have a very low SPR (maximum 6.5 percent for AGMD), and this translates into high recycle ratio to achieve the desired recovery. Additionally, the results indicate that the configurations with highest thermal efficiency AGMD, SGMD, and VMD have the highest single pass recovery and the lowest recycle ratio. Along with increased heating and cooling demand, a high recycle ratio increases the cost of pumping electricity as well as capital costs for equipment such as membranes, chillers, heat exchangers, and installation. This effect is noticeable in the capital and operating costs of the PGMD with the highest recycling ratio.

***Reynolds number*.** Different MD configurations operate at different Reynolds numbers (Figure 5d) at their theoretical minimum treatment cost. To achieve the lowest cost, SGMD and AGMD, operate at low Re of 50 and 317, respectively. While lower Re result in higher temperatures and concentration polarization, these configurations achieve their theoretical minimum treatment cost by operating under these flow conditions. Several studies, however, have shown a direct link between increased fouling and scaling and reduced flux when operating at low Re [74-76]. As a result, operating these configurations at such low Re may be impractical. To gain insights on practically relevant costs, we examined SGMD and AGMD systems at higher Re. Table 1 compares the obtained treatment costs for operation at Re's of 500, 1000, and 1500 to the ideal minimum cost associated with low Reynolds numbers.

Table 1. Treatment cost ($/m$^3_{feed}$) for various Reynolds number

Re	Optimum Re*	500	1000	1500
AGMD	4.57	4.65	5.55	7.22
SGMD	9.81	22.4	37.5	53.1

* The optimum Re values for AGMD and SGMD that result in the minimum cost (as specified in figure 5d) are 317 and 50, respectively.

Increasing the Reynolds number for AGMD from 317 (corresponding to lowest treatment cost) to 1500 results in a nearly 58 percent increase in the treatment cost. This is because AGMD requires large specific area (110.705 m^2/kg) to achieve the cost optimum GOR (Figure 5a). At such large specific areas, the required energy for pumping is highly dependent on the module's length to width ratio. As this ratio increases, the Reynolds number and module length increase, resulting in an increase in pressure drop and required energy for pumping. To achieve the lowest cost and high GOR while operating at large specific areas, the optimal design would have a low length to width ratio to avoid high pumping costs. At higher Reynolds number, the module length to width ratio increases and results in higher pumping cost. In order to avoid high pumping costs at high Reynolds number, the system must operate at lower specific areas (49 m^2/kg corresponding to Reynolds number of 1500), lowering the GOR while increasing steam consumption and total treatment costs.

The variation in treatment cost with increase in Reynolds number is even more pronounced for SGMD. As previously described, blower cost is a significant component of treatment cost for SGMD systems. To achieve the lowest treatment cost and optimum GOR, SGMD has a large specific area (63.4 m^2/kg; Figure 5a). This requires the system to operate at low length-to-width ratios in order to avoid high blower costs, which dramatically reduces the Reynolds number on the feed side. While the hot channel flowrate is 4-5 times that of the air channel, its Reynolds number is an order of magnitude lower than that of air channel because to the difference in viscosity and density of the two flow streams. As a result, when the minimum allowable Reynolds number on the feed side is increased, the system must either operate at the optimal specific area but with increased length to width ratios, increasing blower costs, or with a smaller specific area, lowering

the GOR and increasing steam consumption. When the Reynolds number is increased from 50 (corresponding to lowest treatment cost) to 1500, the combination of above two effects results in a 441 percent increase in treatment cost. It is worth noting that the air channel thickness in this study is comparable to the cold channel thickness in other configurations (i.e., 1.9 mm). At the same air flowrate, the lower the thickness, the greater the air side Reynolds number, pressure drop and blower cost. Increasing the air channel thickness is one way to reduce SGMD costs while decreasing the specific areas and increasing feed side Reynolds number. Although increasing the thickness of the air channel reduces the convective heat transfer coefficient, the cost savings associated with the reduced blower cost outweigh the temperature polarization in the air stream. For example, increasing the air channel thickness from 1.9 mm to 1.9 cm reduces the cost of SGMD treatment from 53.1 to 14.9 $\$/m^3_{feed}$ when operating at a minimum Reynolds number of 1500.

2.3.1 Sensitivity Analysis

MD inlet temperature- The optimization model in our work has an upper bound for MD hot side inlet temperature set to 90°C, with medium pressure steam at 140°C as the heat source. The results presented in Figures 4 and 5 indicate that all membrane configurations operate at the maximum inlet temperature of 90°C in order to achieve the lowest treatment cost. MD can operate at lower temperature if a high-quality heat source is not available. Additionally, salt solubility varies with temperature, with salts such as $CaCO_3$, $CaSO_4$, and $Mg(OH)_2$ exhibiting decreased solubility at higher temperatures [74]. As such, it may be beneficial to operate the MD system at

lower temperatures to avoid scaling in the presence of these salts in the feed water. Figure 6 depicts the variation in optimum treatment cost for different MD inlet temperatures.

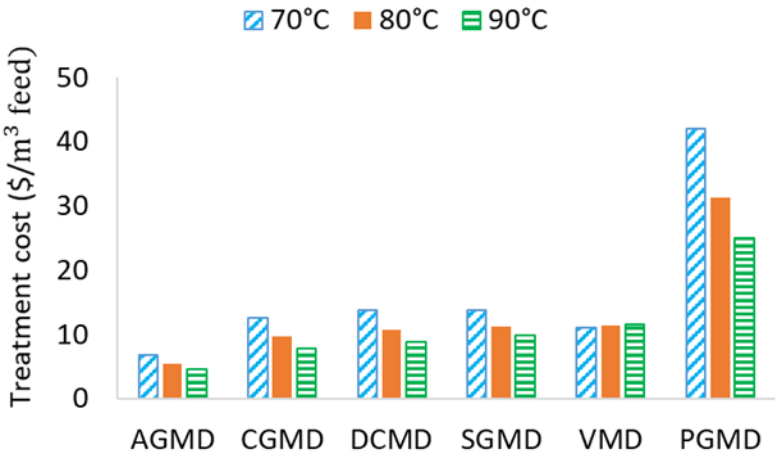

Figure 6. Variation in treatment cost as a function of MD inlet temperature

Except for VMD, lowering the MD inlet temperature increases the treatment cost for all MD configurations. This is because systems operating at higher MD inlet temperature generate higher fluxes initially along the module length, thereby increasing the average flux, thermal efficiency, and single pass recovery. Additionally, higher temperature enables the system to have higher heat recovery ratio and higher GOR.

Unlike other MD configurations, variations in MD inlet temperature has very little impact on the cost of VMD. This is consistent with the fact that the VMD configuration has minor heat recovery, and its thermal efficiency does not vary significantly with temperature. Our analysis indicates that lowering the inlet temperature from 90 to 70°C results in a decrease in the optimum vacuum pressure from 17.3 kPa to 6.9 kPa, which enables high flux and avoiding large membrane area caused by low flux at lower inlet temperatures.

Brine salinity. Figure 7 shows the effect of brine salinity on the treatment cost and GOR for various MD configurations. At high recoveries, the salinity of the mixed stream (recycle stream and makeup feed) approaches that of the reject brine. As the reject brine salinity increases, the salinity and hence the vapor pressure lowering of the mixed stream in the hot channel increases. As a result, the systems' single pass recovery, thermal efficiency and energy recovery are reduced, resulting in lower GOR. Additionally, increase in the brine salinity while maintaining a constant make-up feed salinity increases the system's recovery ratio and required recycle ratio. As a result of the combined effect of a higher recycle ratio and a lower GOR, the treatment cost of the systems increases as the reject brine salinity rises. It should be noted that increasing the brine salinity has no discernible effect on the GOR for VMD, and the treatment cost decreases solely as a result of the change in recovery ratio. Figure 7 also illustrates that PGMD configuration is most sensitive to changes in reject brine salinity. As the brine salinity decreases from 30% to 20%, PGMD configuration outperforms VMD from a treatment cost point of view.

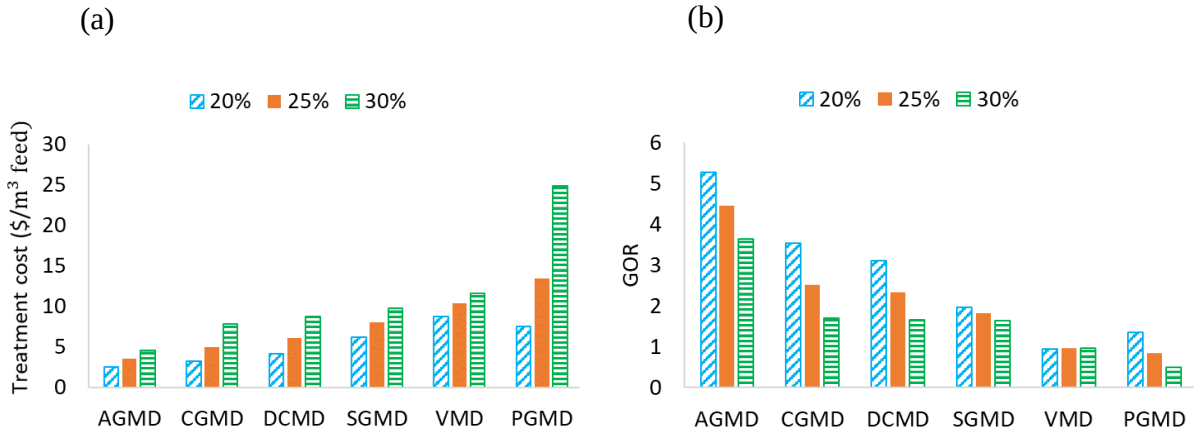

Figure 7. Optimal treatment cost and GOR as a function of reject brine salinity. The produced water salinity is fixed at 10%

Feed salinity. Figure 8 illustrates the effect of changes in produced water salinity on the optimal treatment cost of various MD configurations for a fixed reject brine salinity of 30%. As the feed salinity changes, the GOR and specific area of the systems remain unchanged. This is because the feed salinity has no impact on the operating salinity of the systems operating at high recoveries. As the system's feed salinity increases, both the recovery ratio and the required recycle ratio decrease. Thus, increasing the feed salinity reduces the system's treatment cost solely through the effect of decreasing the recycle ratio. Both Figures 7 and 8 demonstrate the critical effect of the recovery ratio in determining the magnitude of the difference between various MD configurations. As the recovery ratio increases (as a result of decreased feed salinity or increased reject brine salinity), the cost difference between various MD systems becomes more pronounced.

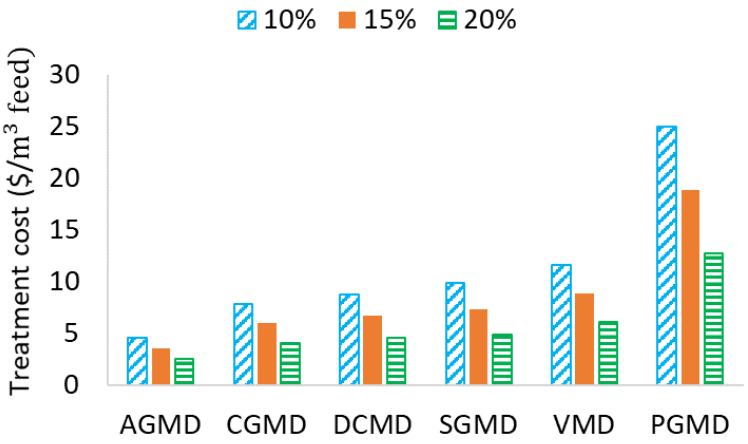

Figure 8. Effect of makeup feed salinity on optimal treatment cost

Gap width in PGMD and AGMD. In AGMD, operation at small gap sizes entails a risk of flooding in the air gap, reducing AGMD to PGMD mode of operation. As a result, larger gap sizes may be used to ensure successful performance of AGMD configuration. Figures 9a and b show that as the airgap size increases, both treatment cost and system area increase while the GOR decreases. This is because the mass flux resistance increases as the gap size increases, requiring

the system with larger membrane area to achieve the same GOR as smaller gap sizes. Simultaneously, the high cost of the membrane prohibits using a very large area. As a result of these two effects, increasing the gap size increases the membrane area but only to a limited extent, resulting in a net decrease in the GOR and an increase in total treatment cost. The gap analysis presented here is based on the assumption that there is no restriction on Re and that AGMD operates at its optimal low Re to maximize cost savings. When the effect of increasing gap and Re are combined, the impact on AGMD performance is even more detrimental. For instance, if AGMD must operate at Reynolds number of 1,500 and a large gap size of at least 3 mm, the cost of AGMD increases from \$4.57 to \$11.29/m^3feed, making it economically unattractive.

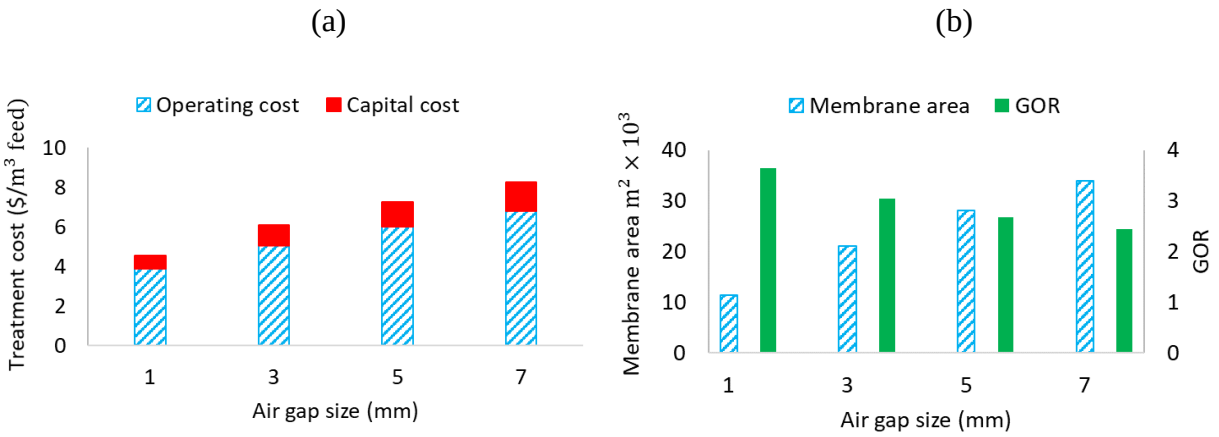

Figure 9. Effect of airgap size on a) optimal treatment cost b) membrane area and GOR of AGMD

As previously described, the permeate gap in PGMD acts as an additional heat resistance layer that reduces the system's performance. As a result, the PGMD system needs to operate with smaller gap sizes to achieve better performance. However, operation at very small gaps may be prohibitive for successful performance of the system due to pressure buildup in the permeate gap, which prevents the permeate from flowing out of the system [54]. As shown in Figure 10, smaller gap sizes result in lower treatment costs, smaller membrane area and higher GOR. This is because

a smaller gap layer improves heat transfer, increasing both heat recovery and thermal efficiency, resulting in a higher GOR. Additionally, single pass recovery increases with smaller gap sizes, lowering the recycle ratio and requiring less total membrane area.

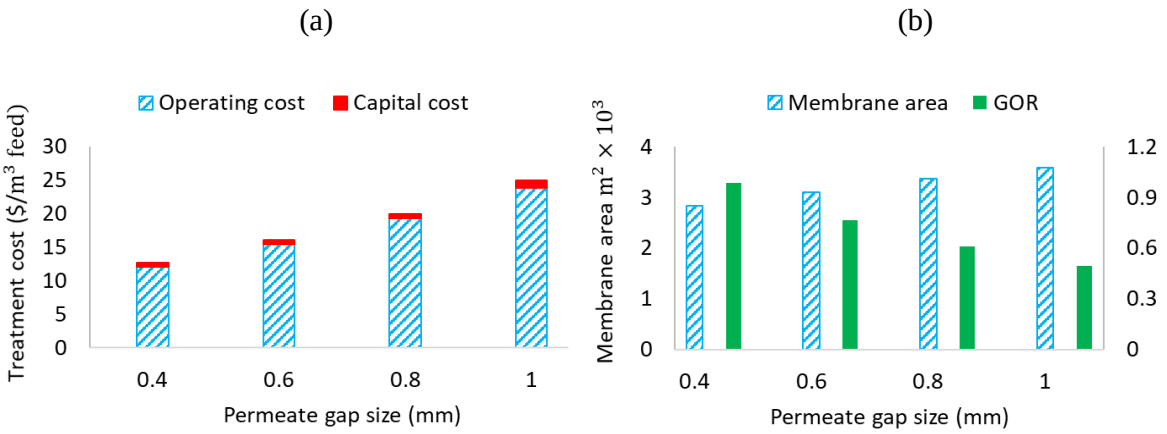

Figure 10. Effect of permeate gap size on a) treatment cost b) membrane area and GOR of PGMD

2.3.2 Membrane Thickness in MD Configurations

This analysis has shown that the GOR of PGMD, DCMD, and CGMD configurations is limited due to their relatively low thermal efficiency. Swaminathan et al. [54] highlighted the effect of increasing membrane thickness on enhancing GOR for CGMD system, assuming membranes as thick as 2 mm. Increasing the membrane thickness increases both conduction heat resistance and mass transfer resistance, resulting in higher thermal efficiency and lower flux. In order to study the effect of membrane thickness on treatment cost, we use optimization models of DCMD, PGMD, and CGMD configurations with membrane thickness as the optimization variables. We then compare the optimum thickness that yields the lowest cost for each configuration with the results obtained using commercially available membranes (0.06 mm thickness).

(a)

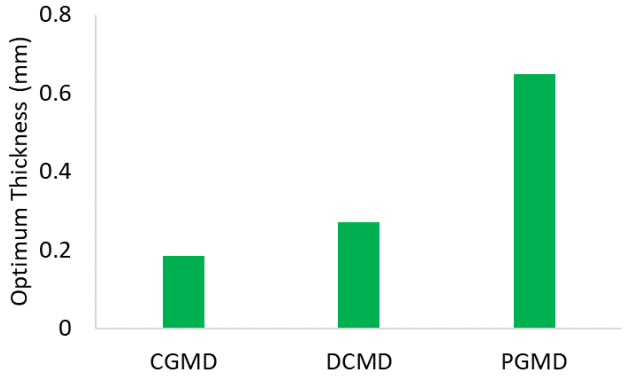

(b)

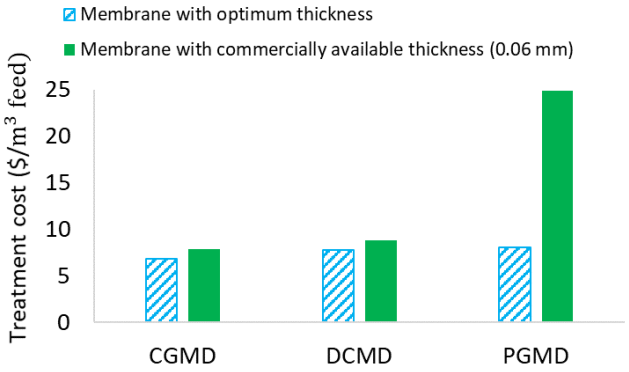

(c)

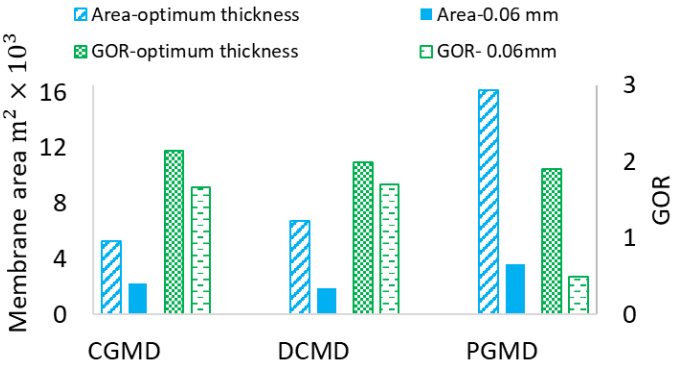

Figure 11. a) Optimum membrane thickness yielding minimum treatment cost, b) MD treatment cost at optimum membrane thickness and thickness of commercially available membranes (0.06 mm) c) Membrane area and GOR at optimum membrane thickness and thickness of commer

Figure 11 shows optimum membrane thickness and a comparison of the treatment cost, membrane area, and GOR corresponding to optimum membrane thickness and actual membrane thickness of commercially available membrane (0.06mm thickness). All three configurations have membrane optimum membrane thickness higher than 0.06 mm. These thicker membranes improve treatment cost and GOR in all configurations, but the membrane area increases because of reduced flux. To compensate for the negative effect of the permeate gap on thermal efficiency, PGMD requires a higher optimum thickness than DCMD and CGMD. PGMD also achieves the greatest cost savings and improvement in GOR as compared to DCMD and CGMD when operated using membranes with optimized thickness. This indicates that amongst all configurations, PGMD treatment cost shows the highest sensitivity to membrane thickness. When a sufficiently thick membrane is used, the GOR and cost performance of PGMD is comparable to that of CGMD and DCMD, but with a larger membrane area and lower flux.

The treatment cost of PGMD decrease to $\$8.09/m^3_{feed}$ when optimum membrane thickness is used but a large membrane area of ~16,000 m^2 would be needed for a hypothetical treatment plant. This analysis is based on the constant permeate gap size of 1 mm. The combined effect of reducing the gap size (1 mm to 0.6 mm) and using the optimal membrane thickness results in the treatment cost of $\$8.06/m^3_{feed}$ for PGMD with a total membrane area of 8,995 m^2, which is comparable to the DCMD heat exchanger area but significantly less than that membrane area need in the AGMD system. In comparison to DCMD, CGMD has a lower optimum thickness because it can achieve high energy recovery and GOR with lower membrane thickness due to direct heat recovery within the module. Additionally, unit membrane cost for CGMD is higher than DCMD due to the additional cost of the conductive material. When operating at higher thickness and correspondingly large area, this results in a significant rise in CGMD cost due to the increased cost

of the membrane, which counterbalances the benefit of increased thickness in terms of lowering the system's energy cost.

Cost-optimal design of each MD configuration requires consideration of numerous factors and theoretically cost-optimal design may not be the most attractive from a practical viewpoint. CGMD exhibits encouraging performance at reasonably high Reynolds numbers, resulting in a treatment cost of $\$7.8/m^3_{feed}$ and membrane area of 2,250 m^2 which decreases to $\$6.7/m^3_{feed}$ and membrane area of 5,260 m^2 using a membrane with optimal thickness. The optimal treatment cost for DCMD configuration is $\$8.7/m^3_{feed}$ with a relatively high Reynolds number and a small membrane area of 2,000 m^2 but a large external heat exchanger of 8,000 m^2 The cost of DCMD drops to $\$7.7/m^3_{feed}$ when a membrane of optimal thickness is used, while the membrane area increases to 6,000 m^2 and the external heat exchanger area decreases slightly to 7,500 m^2. Given the performance degradation of AGMD at high Re and large gaps, uncertainty in CGMD conductive material cost, the required membrane area (and hence system footprint), current availability of membranes with the desired thickness, and the process' practical success, DCMD appears to be the most attractive configuration from a practical viewpoint. With further advancements in material types, thickness of MD membranes, and precise cost estimates for the conductive material, other MD configurations may have the potential to outperform DCMD.

2.4 Conclusions

We developed optimization models for the single stage continuous recirculation MD process for six MD configurations (DCMD, AGMD, PGMD, CGMD, VMD, and SGMD) with the objective of minimizing total unit cost of produced water treatment at ZLD condition. Stream properties (temperature, salinity, flowrate), membrane geometry, heat exchangers area, required energy (steam and electricity) are the optimization variables. We performed two series of optimization, one with membrane thickness set constant and the other with membrane thickness as one of the optimization variables. We compared the cost, membrane area, flux, specific area, GOR, thermal efficiency, heat recovery, single pass recovery, recycle ratio, and stream flow Reynolds number of the optimal design of the MD configuration. Additionally, we performed sensitivity analyses for the inlet temperature of the hot channel, feed salinity, brine salinity, and the gap size to study their effect on MD performance. The analysis was conducted for a hypothetical treatment plant with a capacity of 10 kg/s concentrating hypersaline produced water from 10% to 30% salinity. The following are the major findings from the study.

- For 1mm gap size and membrane with thin active layer of 0.06 mm, AGMD yields the lowest treatment cost of \$4.57/m^3_{feed}, followed by CGMD, DCMD, VMD, SGMD, and PGMD with treatment cost of 7.8, 8.7, 9.8, 11.63, and \$24.11/m^3_{feed}, respectively.
- Energy cost of heating and cooling constitute the major portion of the total treatment cost for all configurations. AGMD requires lowest energy with GOR of 3.6 and PGMD requires the highest energy with GOR of 0.5. VMD, SGMD, and AGMD have the highest thermal efficiency, while AGMD, DCMD, and CGMD have the highest heat recovery.

- AGMD has the lowest flux of 2.1 LMH with the largest membrane area, while VMD and DCMD with the smallest membrane areas have the highest fluxes of 14.6 and 12.8 LMH, respectively.
- SGMD and AGMD operate at low Re of 50 and 317, respectively, to achieve the lowest cost, whereas all other configurations have Re greater than 1000. Increasing the Reynolds number of the SGMD and AGMD significantly increases their cost.
- All MD configurations have a low single pass recovery (up to 6.5 percent for AGMD) and a high recycle ratio. The highest single pass recovery and lowest recycle ratio are found in thermally efficient AGMD, SGMD, and VMD configurations.
- For all MD configurations, decreasing the MD inlet temperature increases the treatment cost (excluding VMD). The optimal vacuum pressure in VMD decreases as the inlet temperature decreases to maintain the high flux.
- When the brine salinity remains constant, increasing the feed salinity lowers the treatment cost because of the decrease in recycle ratio. The GOR of the system is independent of feed salinity at high recoveries. At high recoveries, the operating salinity of MD is highly dependent on brine salinity. Increasing brine salinity raises treatment costs due to a decrease in GOR and an increase in recycle ratio at constant feed salinity.
- In AGMD and PGMD, increasing the gap size increases membrane area while lowering GOR and treatment costs. PGMD may operate over smaller gap sizes, whereas AGMD requires larger gap sizes to avoid flooding. This reduces the difference in treatment costs between these two configurations when comparing AGMD with larger air gap size than permeate gap size in PGMD.

- The optimum thickness of the membrane in DCMD, CGMD, and PGMD is greater than the constant thickness of 0.06 mm, with PGMD having the higher optimum thickness than the other two. By operating at their optimal thickness, the GOR and area of the configurations, particularly for PGMD, increase, while flux and treatment cost decrease.

3.0 Optimization-based Economic Comparison of Multi-stage Membrane Distillation Configurations for Application in Shale Gas Produced Water Treatment

Unconventional oil and gas production raises significant concerns regarding sustainable management of high salinity wastewaters. Membrane distillation is a thermal desalination system capable of treating hypersaline brines such as produced water. Several membrane distillation configurations exist, each with their own performance and treatment cost. The low single pass recovery in MD systems when operating in single stage continuous recirculation mode necessitate a large recycle stream to achieve the desired recovery, resulting in high energy consumption and operating cost. Multistage configurations operating in continuous recirculation operation mode offer the potential advantage to reduce the energy intensity of MD systems. However, rigorous analysis is needed to evaluate the performance of various MD configurations when operating in multi-stage mode. We present an optimization-based comparison of economic and energetic performance for six MD configurations ((DCMD, AGMD, PGMD, CGMD, and VMD) operating in multi-stage continuous recirculation mode. Our findings demonstrate that multistage operation reduces the treatment cost and energy intensity of all MD configurations compared to single stage MD, with the greatest benefit for VMD and PGMD. AGMD with five stages outperform other configurations with treatment cost of 3.58 $\$/m^3_{feed}$, followed by VMD, CGMD, DCMD, and PGMD with 3.8, 4.2, 5.4, and 9.06 $\$/m^3_{feed}$ corresponding to twelve, eight, eight, and sixteen stages, respectively.

3.1 Introduction

The shale oil and gas industry in North America has experienced a significant boom as a result of developments in horizontal drilling and hydraulic fracturing. The shale gas revolution, however, is coupled with substantial environmental sustainability challenges with water management [77-80]. Hydraulic fracturing, a technique used to extract shale oil and gas, is a water-intensive process that strains groundwater resources in certain shale plays, such as Eagle Ford. [1, 81]. Furthermore, during well production, a large volume of water known as produced water is generated with a total dissolved solids (TDS) ranging between 70,000 and 350,000 mg/L [40]. These hypersaline brines, which are costly and difficult to treat, also pose contamination risk for both surface and ground water supplies [10, 82-85].

Disposal via deep well injection or recycling for reuse in hydraulic fracturing are the two most common strategies for produced water management [42, 43, 86, 87]. Direct disposal incurs a high transportation cost due to the large volume of produced water, particularly in regions that lack nearby disposal wells (e.g. Marcellus shale play) [14]. Additionally, it poses environmental risks such as induced seismicity and contamination of aquifers due to well leakage [44-46]. Recycling and reuse alleviates pressure on fresh water reservoirs for hydraulic fracturing water demands. However, this strategy imposes storage constraints for future reuse and becomes infeasible, especially when produced water volume exceeds the hydraulic fracturing water demand [1], as well as the risk of saline water leakage from storage tanks or pits [88].

Desalination technologies may be a viable long-term alternative as disposal and recycling regulations tighten and recycling is not an option. Desalination processes can provide fresh water for surface discharge, hydraulic fracturing, or other beneficial uses while reducing the volume reject brine to be managed. Desalination systems could also be used in tandem with a crystallizer

to reduce brine volume and precipitate solid salts, which necessitates desalination technologies operating at zero liquid discharge (ZLD) or near saturation brine conditions. Selecting an appropriate desalination technology for produced water treatment can be challenging, as not all desalination technologies are capable of treating hypersaline brines due to factors such as corrosion risk in conventional distillation systems and scaling and membrane failure in reverse osmosis [18-20, 89].

Membrane distillation (MD) is an emerging water treatment technology that works based on a temperature gradient-induced partial pressure difference across a hydrophobic membrane. While water vapor molecules from the hot side of the membrane pass through the membrane pores, the hydrophobic surface of the membrane prevents mass transfer of the liquid phase [23]. Mobile and modular designs, ability to treat high salinity wastewaters, high rejection factor, and ability to work with low-grade energy sources such as waste heat and geothermal energy are some of the attractive key features of MD [24, 25, 27, 72, 90]. Combined together, these features have made MD the focus of many recent modeling and experimental studies focused on evaluating its potential for treating hypersaline streams such as shale gas-produced water.

Based on the arrangement and operation of several stream channels (hot feed, permeate, and cold flow), MD configurations can be classified into five major categories including direct contact (DCMD), air gap (AGMD), permeate gap (PGMD), conductive gap (CGMD), sweeping gas (SGMD), and vacuum (VMD) [50-52]. Previous in-depth optimization-based analysis and comparison for the aforementioned MD configurations in single stage continuous recirculation mode demonstrated that all configurations have a low single pass recovery, with AGMD having the highest single pass recovery of 6.5 percent when operating at ZLD condition [91]. This necessitates recirculation and mixing of a significant portion of the high saline reject brine stream

with the makeup feed stream in order to achieve the desired high recovery. As a result, the salinity of the feed stream that passes through the MD module approaches that of the reject brine stream. Except for VMD, sensitivity analysis of reject brine salinity revealed that operating at a higher reject brine salinity (corresponding to higher recoveries) increases the energy intensity of all MD configurations. This is due to increased vapor pressure lowering at higher salinities, which has a direct impact on permeate production and heat recovery within the system. Because of the negligible heat recovery inherent in VMD configuration at single stage mode of operation, energy intensity is relatively high regardless of brine salinity.

Three methods are suggested in the published literature for reducing the energy intensity of MD systems: batch recirculation, multi-effect configurations, and multi-stage continuous recirculation [48, 92-94]. Batch operation mode sends a fixed amount of feed from the circulation tank to the membrane unit multiple times until the salinity of the feed reaches a desired level. With initial cycles operating at lower salinities, the energy intensity of separation process decreases for a given level of recovery in batch recirculation. Unsteady state batch operation, however, may not be suitable for large scale and continuous operation systems [49]. In multi-effect MD system (e.g. vacuum multi-effect MD systems), the latent heat of vapor condensation is recovered and directly used as evaporation energy for the separation process in a series of effects similar to conventional multi-effect distillation [92, 94]. In multi-stage continuous recirculation, however, the feed is preheated using the latent heat of condensation prior to the separation process [48]. Multi-stage and multi-effect systems necessitate extensive analysis for evaluating their economic and energetic performance; The focus of this specific study is on multi-stage continuous recirculation MD systems.

Several studies have been conducted on the energy intensity and recovery of multi-stage MD systems. Swaminathan et. al. [48] compared the energy intensity of conductive gap MD for various recirculation modes of operation and discovered that the batch recirculation method yields the lowest energy intensity. They demonstrated that at a high number of stages, the energy intensity of multi-stage continuous recirculation mode approaches that of batch mode, with initial stages operating at lower salinities. He and colleagues [49], as well as Gilron and colleagues [95], examined multi-stage DCMD and showed that high recoveries can be achieved with lower energy intensities when operating in a multi-stage mode. Chung et. al. [96] and Summers et. al. [97] developed a multi-stage VMD system with initial stages operating at a higher vacuum pressure that gradually decreases with each subsequent stage, allowing for greater heat recovery and a lower energy intensity within VMD systems. All of the studies mentioned above are primarily focused on the energy consumption of multistage MD systems. However, the advantages and performance of multi-stage MD operation over single stage operation mode is best studied through a rigorous optimization-based analysis that considers the trade-offs between cost and energy. Some recent studies have focused on economic analysis of multi-stage MD configurations. Dudchenko and coworkers [98] studied the minimum costs associated with gap type configurations. Their work did not consider the possibility of recirculation within stages, resulting in an increase in minimum number of stages required to achieve a certain level of water recovery. Carrero-Parreno et. al [67] conducted an analysis of the optimal cost of multistage DCMD. They, however, did not account for temperature drop along the module. Instead, they assumed a fixed MD inlet temperature as the constant driving force for separation along the module, resulting in an overestimation of permeate production. Lu and colleagues [99] developed a mathematical model for cost optimization of multistage AGMD without accounting for interstage heating. To the best of our knowledge, there

is no optimization-based process and cost analysis for multi-stage VMD systems. A comprehensive study is required to understand how multi-stage operation affects the cost, energy consumption, and cost of each specific MD configuration, as well as how different MD configurations compare against each other when operating in multi-stage mode under consistent set of conditions.

We develop optimization models for multi-stage continuous recirculation for DCMD, VMD, and all gap types of configurations, taking interstage heating and recirculation into account. The developed optimization models are used to compare and analyze the treatment costs and energy consumption of various multi-stage MD designs for treating produced water from unconventional reservoirs, as well as ZLD operations. We also provide an in-depth evaluation of key performance metrics for each MD configuration. Finally, we investigate how membrane thickness influences the number of stages required to achieve the lowest treatment cost. To our knowledge, this is the first optimization-based study to offer a comprehensive comparative evaluation of all MD configurations in a multi-stage continuous recirculation mode of operation from a cost and energy standpoint.

3.2 Methodology

Process description- The operation of the heater and hot feed channel, as well as the permeation process through the membrane pores, is the same for each of the five studied configurations. The hot feed from the heater enters the hot channel of the membrane, and water vapor permeates the hydrophobic membrane pores due to the vapor pressure difference across the membrane. Permeated vapors condense on the water surface in direct contact with the membrane

surface in DCMD, PGMD, and CGMD. However, in AGMD, the permeated vapor flows through the airgap and condenses on the cooling surface. In the case of VMD, the vapor flow is sent to an external condenser for permeate condensation. In addition to differences in condensation site, these configurations differ from each other by their preheating process and recycling stream paths, as well as their multi-stage structure, which is described in detail next.

Multi-stage DCMD- Figure 12a depicts DCMD multi-stage continuous recirculation mode of operation. Because there is no gap between the cold channel and the membrane, only pure water may be used as a coolant, necessitating the installation of an external heat exchanger to recover heat from the heated coolant. To maintain the temperature differential across the membrane, the pure water flow (coolant) exiting the heat exchanger enters a chiller. As such, each stage of the multi-stage DCMD consists of an MD module, a heater, a heat exchanger, and a chiller. A portion of the concentrated brine exiting the hot channel from each stage is recirculated and mixed with the (makeup) feed for that particular stage. The amount of water recovered in each stage can be adjusted by varying the volume of the recycle stream in that stage. The reject concentrated brine exiting the hot channel from each stage is used as a makeup feed for the subsequent stage. As a result, subsequent stages operate at increasing salinities, with the initial ones operating at lower salinities.

Multistage Gap type MD- Figure 12b illustrates the multi-stage continuous recirculation for gap type MD configurations. Because all gap type MD modules (AGMD, PGMD, CGMD) have separate permeate and cold channels, the saline feed stream can be used as the coolant in the cold channel, recovering heat directly from the membrane's hot side. In Gap type MD, as with DCMD, a portion of the reject brine is recirculated within each stage to achieve the desired level of recovery for that stage. To maintain the required temperature difference for permeation and

condensation, the concentrated brine (including both recycle and reject streams) is cooled before entering the cold channel via a chiller. As a result, each stage of the multi-stage gap MD is made up of an MD module, a heater, and a chiller. The concentrated reject brine exiting the chiller of each stage serves as the makeup feed for the next stage, and stages operate with increasing salinities from first to last.

Multistage VMD- Multi-stage continuous recirculation mode of operation for VMD configuration is illustrated in figure 12c. Condensation occurs in an external condenser in the VMD configuration, and non-condensable gases are pumped out using a vacuum pump. Except for the first stage, each stage is comprised of a VMD module, a condenser, and a flashing tank. The first stage includes a heater prior to the VMD module. We previously demonstrated that stream salinity has little effect on the energy intensity of single stage VMD with continuous recirculation of concentrated brine. Indeed, the primary reason for the high energy intensity of VMD systems is the limited heat recovery due to the lower temperature of the vapor flowing to the condenser compared to the concentrated brine exiting the module. To circumvent this limitation, Chung et al. [96] proposed a multi-stage VMD configuration with stage wise reduction in vacuum pressure. The permeated vapor from each stage flows out to a flashing and mixing tank, where it is mixed with the flashed pure water from previous stages before being sent to the condenser for pure water production and heat recovery. The total volume of concentrated brine exiting the hot channel from each stage serves as the feed for the subsequent stage. In comparison to multi-stage DCMD and AGMD, multi-stage VMD does not have a separate recirculating stream for each stage. This is because interstage recirculation in VMD precludes heat recovery, just as it does in single-stage VMD. Instead, there is a single recycle stream from the final stage of VMD that is mixed with makeup feed and passes through the train of condensers for preheating before entering the heater,

which is followed by the first VMD module. Furthermore, unlike multi-stage gap MD and multi-stage DCMD, multi-stage VMD utilizes a single heater prior to the first stage. This is supported by previous analysis for single stage continuous recirculation VMD, in which it is demonstrated that the treatment cost and energy intensity of the single stage VMD are not strongly related to the MD inlet temperature. Indeed, depending on the inlet temperature, the driving force for permeate production can be adjusted by adjusting vacuum pressure. The configuration investigated here is similar to that developed by Chung et al. [96], with the exception that the recirculating brine exiting the final stage does not flow into the chiller and the final stage condenser. This is due to the fact that the temperature of the recirculating brine is higher than the vapor exiting the last stage, preventing effective heat recovery. Instead, we use the makeup feed and a separate coolant stream loop for the final stage condenser and chiller. The results section explains in detail how this arrangement improves the energetic and cost performance of multistage VMD.

a)

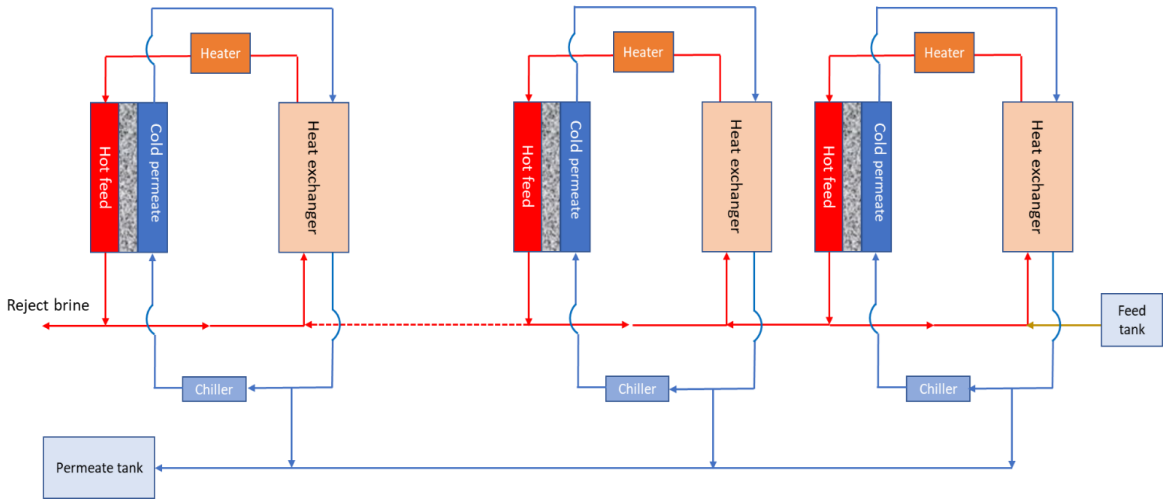

b)

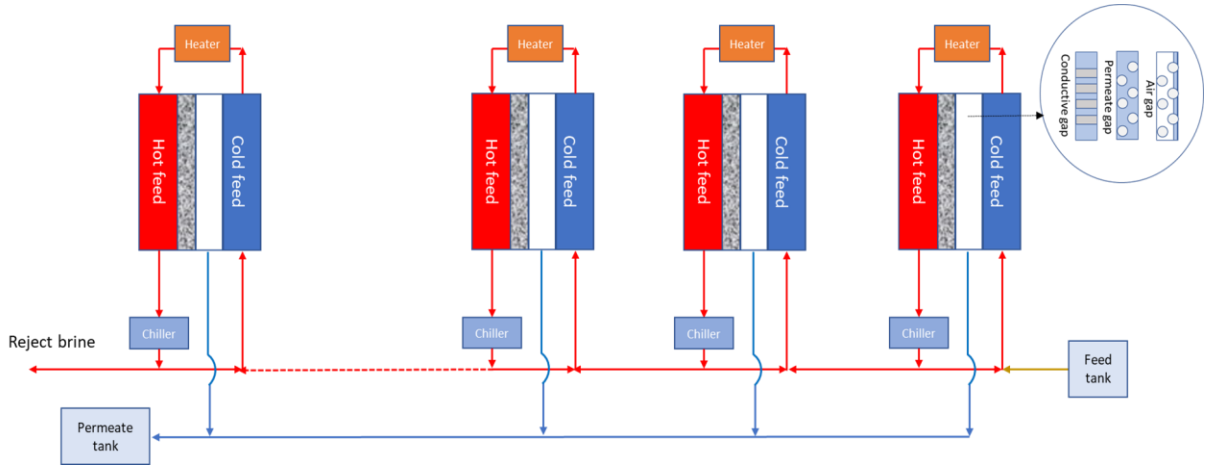

c)

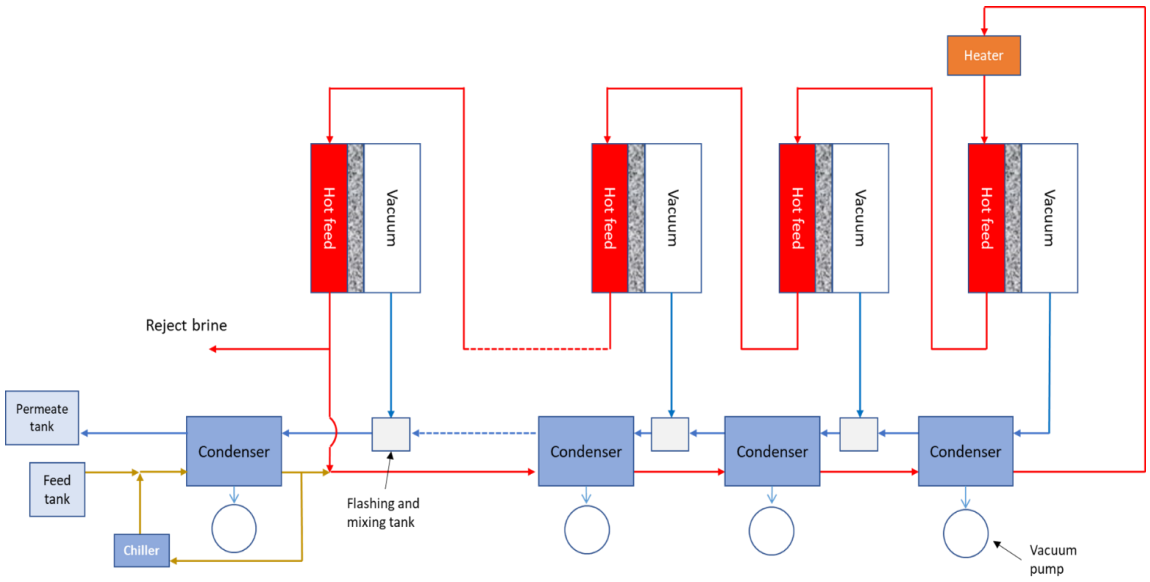

Figure 12. Membrane distillation configurations in multistage continuous recirculation operation mode:a) DCMD, b) Gap type MD, c) VMD

3.2.1 Cost Optimization Model

In this study, we developed optimization models for each of the multi-stage MD systems using governing thermodynamic and representative cost equations for various system elements such as membrane modules, heaters, heat exchangers, chillers, and pumps. We employ a modeling approach similar to that used in our previous work for single stage continuous recirculation, with modifications for multi-stage configuration. The equations used to model the processes are detailed in Appendix tables 10 to 12. In brief, the MD process was modeled using a combination of mass and energy balance equations (including heat flux, mass flux, enthalpy change, and mass flowrate change) for each particular membrane module and configuration. Convective, conductive, and evaporative heat transfer all contribute to the heat flow in the membrane module. Convective heat transfer coefficients were estimated using empirical Nusselt number correlations, and conductive heat transfer coefficients were determined using thermal conductivity and heat transfer channel thickness. The vapor flux and enthalpy of evaporation were used to determine evaporative heat flux. Vapor flux was correlated, via mass transfer coefficient, to pressure difference corresponding to saturation temperatures difference across the evaporative and condensing surface of the module. The mass transfer coefficient was calculated using membrane permeability coefficient (and mass diffusion of water vapor into air in case of AGMD). Finally, enthalpy and mass flowrate change in cold and hot channels were calculated using the mentioned heat and mass fluxes via a discretized model. We designed heat exchangers, condensers, and heaters using the energy balance and log-mean temperature difference method, and we modeled chillers by calculating the required cooling energy and accounting for the coefficient of performance.

Multi-stage configuration modeling is accomplished by properly connecting stream state variables (such as salinity, flowrate, and temperature) at the inlet and outlet of one stage to the

inlet and outlet of another stage. This connection occurs when concentrated reject brine (excluding stage recycle stream) exits the hot channel in DCMD and the chiller in AGMD and serves as a makeup feed for the subsequent stage. The stage connection in VMD is achieved through four streams: 1) concentrated reject brine exiting the MD modules and entering the subsequent stage as feed; 2 and 3) mixture of make-up feed exiting the final stage condenser and recycle stream exiting the final stage MD module that connects the inlet and outlet of the coolant side of successive stage condensers; and 4) condensed pure water flow from the hot side of each stage condenser to the subsequent stage mixing and flashing tank.

The developed non-linear programming (NLP) models were then coded in GAMS and solved using the CONOPT4 solver for a specified number of stages to determine the optimal structure and operating conditions (including the size of each stage's elements, stream flowrates, salinity, temperature, and pressure) while minimizing the system's total unit treatment cost. The influence of stage count on each system's performance is investigated by repeating the optimization process for various stage numbers as fixed parameters. For each configuration, we ran two sets of optimization models. The first model, which produced the bulk of the results, considers the membrane thickness to be a constant parameter, allowing comparison of alternative configurations with the same thickness.

$$\min \mathrm{TUC}\,(y), y = (T, M, X)^T \in \mathbb{R}$$

$$\text{s.t.} \quad \varphi(y) = 0$$

$$\psi(y) \leq 0$$

The second model, the results of which are reported in the final section of the manuscript, incorporates membrane thickness as an optimization variable in order to assess the effect of membrane thickness on the design of multi-stage configurations.

$$\min \mathrm{TUC}\,(y), y = (T, M, X, \delta_m)^T \in \mathbb{R}$$

$$\text{s.t.} \quad \varphi(y) = 0$$

$$\psi(y) \leq 0$$

3.2.2 Performance Criteria

Two performance criteria are used to evaluate the performance of the modeled multistage MD configurations: *'overall'* and *'stage'* criteria. The overall criteria assess the performance of a multistage configuration MD as a whole, whereas the 'stage' criteria examine the operation of each individual stage within the multistage configuration.

Gain output ratio (GOR) is an overall performance metric that is defined as the ratio of the total heat of permeate evaporation over all stages to the total heat of steam used to pre-heat the water (Equation 20).

$$\mathrm{GOR}\begin{cases} = \dfrac{\sum_i \sum_z M_p^{i,z} H_e^{i,z}\left(T_{hm}^{i,z}\right)}{\sum_i M_s^i H_e^i\left(T_s^i\right)} & \text{for DCMD and gap type MD} \\ = \dfrac{\sum_i \sum_z M_p^{i,z} H_e^{i,z}\left(T_{hm}^{i,z}\right)}{M_s H_e(T_s)} & \text{For VMD} \end{cases} \tag{20}$$

Overall thermal efficiency and stage thermal efficiency. The overall thermal efficiency (Equation 21) is defined as the ratio of the total enthalpy of permeated vapor to the total heat transferred across the membranes of all stages. The stage thermal efficiency is defined as the ratio

of the total enthalpy of permeated vapor to the total heat transferred across each stage (Equation 22):

$$\eta_{\mathrm{th}_{\mathrm{overall}}}\begin{cases}=\dfrac{\sum_i\sum_z M_p^{i,z}H_v^{i,z}\left(T_{hm}^{i,z}\right)}{\sum_i\sum_z M_p^{i,z}H_v^{i,z}\left(T_{hm}^{i,z}\right)+q_{cond}^{i,z}} & \text{for DCMD and gap type MD}\\ =\dfrac{\sum_i\sum_z M_p^{i,z}H_v^{i,z}\left(T_{hm}^{i,z}\right)}{\sum_i\sum_z M_p^{i,z}H_v^{i,z}\left(T_{hm}^{i,z}\right)+q_{exp}^{i,z}} & \text{For VMD}\end{cases} \tag{21}$$

$$\eta_{\mathrm{th}_{\mathrm{stage}}}\begin{cases}=\dfrac{\sum_z M_p^{i,z}H_v^{i,z}\left(T_{hm}^{i,z}\right)}{\sum_z M_p^{i,z}H_v^{i,z}\left(T_{hm}^{i,z}\right)+q_{cond}^{i,z}} & \text{for DCMD and gap type MD}\\ =\dfrac{\sum_z M_p^{i,z}H_v^{i,z}\left(T_{hm}^{i,z}\right)}{\sum_z M_p^{i,z}H_v^{i,z}\left(T_{hm}^{i,z}\right)+q_{exp}^{i,z}} & \text{For VMD}\end{cases} \tag{22}$$

Overall heat recovery and stage heat recovery. The overall heat recovery is defined as the ratio of total heat recovered across all stages of the MD system to total heat consumed for separation (which includes heat recovered and external heat of steam).

$$\mathrm{HR}_{\mathrm{overall}}\begin{cases}=\dfrac{\sum_i Q_{HR}^i}{\sum_i M_s^i H_e^i(T_s^i)+Q_{HR}^i} & \text{for DCMD and gap type MD}\\ =\dfrac{\sum_i Q_{HR}^i}{M_s H_e(T_s)+\sum_i Q_{HR}^i} & \text{For VMD}\end{cases} \tag{23}$$

The stage heat recovery for DCMD and gap type MD with individual heaters for each stage is defined as the ratio of heat recovered to total heat consumed in one stage (equation 24):

$$\mathrm{HR}^i=\frac{Q_{HR}^i}{M_s^i H_e^i(T_s^i)+Q_{HR}^i} \tag{24}$$

Overall water recovery and stage water recovery. The overall water recovery ratio (ORR) is the ratio of permeate production to the makeup feed flowrate of the plant (Equation 25). The stage

water recovery ratio (SRR) quantifies each stage's contribution to overall water recovery, and the sum of each stage's SRR yields the overall recovery ratio (Equation 26).

$$\mathrm{ORR} = \frac{\sum_i \sum_z M_p^{i,z}}{M_f^{plant}} \tag{25}$$

$$\mathrm{SRR}^i = \frac{\sum_z M_p^{i,z}}{M_f^{plant}} \tag{26}$$

Overall feed ratio, overall recycle ratio, and overall heated stream ratio- Overall feed ratio is defined as total stages' (makeup) feed flowrate that passes through the heaters to the plant feed flowrate (equation 27):

$$\mathrm{FR}_{overall} \begin{cases} = \frac{\sum_i M_f^i}{M_f^{plant}} & \text{for DCMD and gap type MD} \\ = \frac{M_f^{plant}}{M_f^{plant}} = 1 & \text{For VMD} \end{cases} \tag{27}$$

Overall recycle ratio total stages' recycle stream flowrate that passes through the heaters to the plant feed flowrate (equation 28):

$$\mathrm{RecR}_{overall} \begin{cases} = \frac{\sum_i M_{rec}^i}{M_f^{plant}} & \text{for DCMD and gap type MD} \\ = \frac{M_{rec}}{M_f^{plant}} & \text{For VMD} \end{cases} \tag{28}$$

The overall heated feed ratio is defined as the ratio of the total stream flowrate sent to the heaters across all stages to the feed flowrate of the plant (equation 29). This is essentially the sum of the overall feed and overall recycle ratios.

$$\mathrm{HSR}_{overall} \begin{cases} = \frac{\sum_i M_f^i + M_{rec}^i}{M_f^{plant}} & \text{for DCMD and gap type MD} \\ = \frac{M_f^{plant} + M_{rec}}{M_f^{plant}} & \text{For VMD} \end{cases} \tag{29}$$

The specific area is the ratio of the membrane's area to the total stream flowrate entering the module:

$$A_S^i = \frac{A_m^i}{M_{rec}^i + M_f^i} \tag{30}$$

3.3 Results and Discussion

The optimization model is used to design a hypothetical produced water treatment plant with a treatment capacity of 10 kg/s (~0.25 million gallons per day), which concentrates produced water with 10% (100,000 mg/Liter) TDS to brine with 30% TDS corresponding to saturation conditions. Tables 1 to 5 in the appendix contain the model input parameters, including plant characteristics, membrane properties, and capital and operating cost data.

Treatment Cost. Figure 13 depicts the variation in optimum produced water treatment cost as a function of number of stages for studied multistage MD configurations. Regardless of the number of stages, AGMD outperforms all other configurations, while PGMD shows the worst performance. However, the difference in treatment costs between various MD configurations is more pronounced at low stage counts and becomes more comparable across MD configurations as stage counts increase. With the exception of VMD, the order of cost performance superiority of one configuration over another in terms of treatment cost stays unchanged for all configurations. AGMD has the lowest treatment cost followed by CGMD, DCMD, VMD, and PGMD. The cost trend line for VMD crosses other configuration trend lines as the number of stages increase, and it begins to outperform DCMD at three stages, CGMD at six stages, and approaches that of AGMD at ten stages.

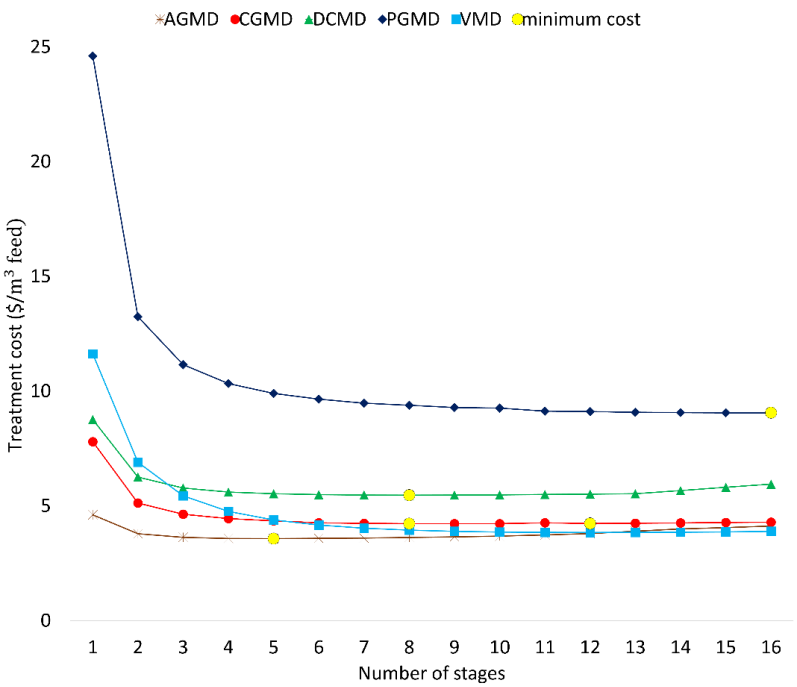

Figure 13. Treatment cost as a function of number of stages. The lowest treatment cost yielded by the optimization model for each configuration is highlighted in yellow color.

For every configuration, the greatest stagewise relative cost savings occurs at two stages. The marginal positive effect of adding stages on the optimal treatment cost starts to show diminishing returns beyond the second stage for all configurations. The cost trend lines start to plateau as number of stages increase reaching an absolute minimum treatment cost, beyond which point the treatment costs increase marginally when additional stages are added. This absolute minimum cost occurs at 5, 8, 8, 12, and 16 stages for AGMD, CGMD, DCMD, VMD, and PGMD, respectively. The optimum treatment costs for AGMD, CGMD, DCMD, VMD, and PGMD are 3.5, 3.8, 4.2, 5.4, and 9.06 $\$/m^3_{feed}$, respectively. When compared to single stage configurations, multistage PGMD and multistage VMD show the greatest improvement in treatment cost reduction.

The capital and operating cost contribution for all configurations with varying stages are shown in figure 36 in the appendix, with a detailed breakdown of the cost components listed in table 13. The majority of the cost is made up of operating cost (primarily heating and cooling costs), which decreases as the number of stages increase. With the exception of PGMD, the capital cost increases marginally for all configurations as the number of stages increase. This is because as the number of stages increases, the number of required equipment increases proportionately, but the size of the required equipment decreases. This is due to the reduction in volume of each stage's feed and recycle streams, which will be discussed in greater detail in the section devoted to the overall recycle ratio. Because of the significant reduction in recycle ratio, which compensates for the increased number of equipment, the capital cost for PGMD initially decreases, and then begins to increase marginally as the number of stages increase. At a certain number of stages, the capital cost increase exceeds the decreasing operating costs, and the configurations reach their absolute minimum treatment cost.

For all configurations, the treatment cost starts approaching the optimal cost at relatively low stage numbers and shows only marginal cost improvement before reaching a minimum. Given the added complexity of multistage systems, it may be practical not to design multistage systems at the absolute lowest treatment cost but instead operate at lower number of stages. This strategy has the advantage of exploiting the cost reduction benefit while reducing the added complexity in multistage MD systems associated with higher number of stages. However, for the purpose of comparison, all subsequent analysis for each configuration is presented at their optimum number of stages which yield the absolute minimum cost.

GOR, thermal efficiency, heat recovery. As described previously, the operating costs of heating and chilling energy account for the largest share of treatment costs and are the primary

area for improvement in multistage MD design. Figure 14 depicts the energy intensity of various MD configurations in terms of GOR at various stages. Although PGMD appears to have the least absolute improvement in GOR, it has the highest relative improvement (between the first and final stage) after VMD; the relative increase in GOR is 90, 85, 65, 55, and 30 percent for VMD, PGMD, CGMD, DCMD, and AGMD, respectively, when their operation at the lowest treatment cost is compared with single stage operation mode. While VMD outperforms DCMD treatment cost at three stages (Figure 12), it outperforms DCMD GOR at five stages (Figure 14). This is because at three stages, VMD has lower treatment cost than DCMD due to the higher capital cost of DCMD heat exchanger and membrane.

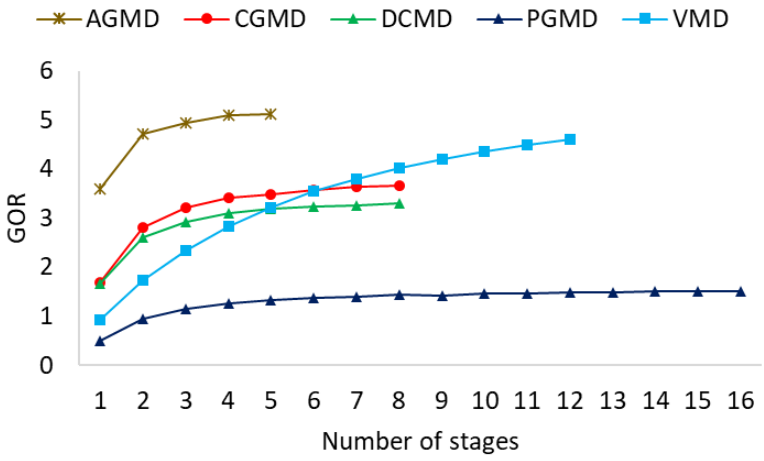

Figure 14. Variation in gain output ratio (GOR) with increasing number of stages

As with treatment cost, the greatest relative improvement in GOR occurs during the initial stages and diminishes as the number of stages increases. Unlike treatment cost, however, GOR continues to increase, even after reaching the point of lowest treatment cost. GOR is determined by heat recovery and thermal efficiency of the MD module. In the case of DCMD and gap type MD, as the number of stages increases, the operating salinity of the initial stages decrease,

improving the thermal efficiency and heat recovery of the initial stages (figure 37 appendix show stage thermal efficiency and heat recovery for MD configurations). The feed salinity of the plant determines the minimum possible salinity at the inlet of the hot channel in the first stage of multistage DCMD and gap type MD. Therefore, as long as the addition of stages results in a reduction in the operating salinity of the initial stages in multistage DCMD and gap type MD there is potential for improvement in thermal efficiency, heat recovery, and GOR.

In the case of VMD, as the number of stages increase, the feed stream (a mixture of recycle and plant feed) passing through the condensers can reach a higher temperature. The maximum possible temperature of feed stream passing through the condenser in VMD is determined by the hot channel's inlet temperature of the first stage. Therefore, as long as the addition of stages results an increase in the feed stream temperature in multistage VMD, there is potential for improvement in thermal efficiency, heat recovery, and GOR.

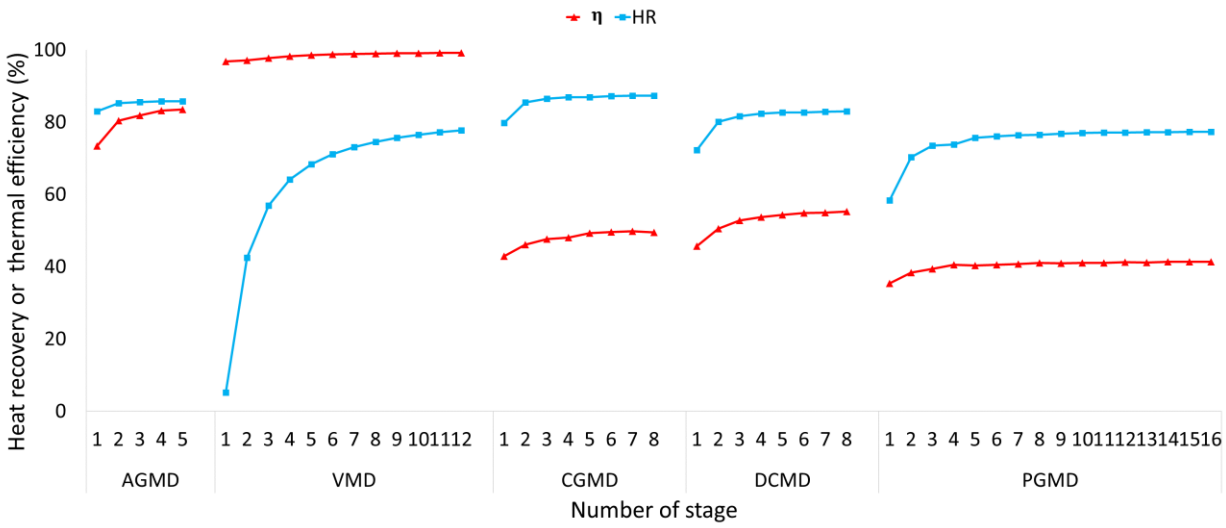

Figure 15. Overall thermal efficiency and overall heat recovery as a function of number of stages

Figure 15 shows the change in overall heat recovery and thermal efficiency as the number of stages increase. As the number of stages increase, AGMD benefits more from increased thermal efficiency, PGMD and VMD benefits more from increased heat recovery, and DCMD and CGMD benefit from both increase in thermal efficiency and heat recovery. CGMD achieves the highest overall heat recovery, followed by AGMD, DCMD, VMD, and PGMD when operating at their cost optimal number of stages. Additionally, VMD has the highest overall thermal efficiency, followed by AGMD, DCMD, CGMD, and PGMD.

Although increasing the number of stages improves heat recovery significantly for certain configurations, we observe that configurations with the highest thermal efficiency (including AGMD and VMD) have the lowest treatment cost and highest GOR when operating at their cost-optimal number of stages. This is because, thermal efficiency is more intrinsic property of a configuration type than heat recovery and is the primary reason for performance differences between various configurations.

Overall feed, recycle, and heated stream ratios. Figure 16 illustrates the overall feed ratio, overall recycle ratio, and overall heated stream ratio for various stage counts. In DCMD and gap type MD, the overall recycle ratio decreases as the number of stages increases for two reasons: 1) the contribution of each stage to water recovery decreases, and 2) more importantly, the lower boiling point elevation in initial stages with lower salinity increases single pass recovery of these stages, requiring a smaller recycle stream resulting in reduction of overall recycle ratio. On the other hand, as the number of stages increases, the overall feed ratio increases proportionately, as each stage adds a feed stream. As a result, the reduction in the overall recycle ratio is offset by an increase in the overall feed ratio, resulting in a nearly constant value for the overall heated stream ratio as the number of stages increases beyond a certain point. This implies that after a certain

number of stages the total amount of feed sent through the heaters remain constant. This leads to an important conclusion that completely eliminating the recycle streams does not result in the lowest cost. Instead, it forces the system to demand a large minimum number of stages in order to reach a certain level of recovery. This increases the system's capital cost for a large number of equipment while also increasing the system's complexity.

The overall feed ratio remains constant in the case of VMD because the system consists of a single heater through which only the plant feed and recycle stream pass. The overall recycle ratio of VMD, on the other hand, decreases as the number of stages increases. The optimum recycle ratio in a single stage VMD is determined by the trade-off between heating and chilling costs. That is, a lower recycle ratio reduces heating demand while increasing chilling demand. This is due to the fact that a lower recycle ratio necessitates a higher single pass recovery. For single stage VMD, higher single pass recovery necessitates lower vacuum pressure, which increases chilling demand. The overall recycle ratio of multistage VMD is determined by the cumulative single pass recovery of the stages. Furthermore, only the permeate from the final stage necessitates the use of chiller energy for condensation. As a result, when compared to single stage VMD, less vapor is sent to the chiller for the same amount of total water recovery. This allows multistage VMD to operate at a lower final vacuum pressure and a higher cumulative single pass recovery without increasing chiller energy demand. The vapor volume of the final stage heading to the chiller decreases as the number of stages increases. As a result, final vacuum pressure can be reduced further for higher single pass recovery and lower overall recycle ratio. However, recycle stream flowrate does not change beyond a certain number of stages. This is because the final vacuum pressure and temperature is limited by chiller bottom temperature and increasing the number of stages beyond a certain number does not increase the overall system cumulative single pass recovery. After a

certain number of stages, the overall heated stream ratio will maintain a constant value as a result of a constant overall feed ratio and a relatively constant overall recycle ratio.

a)

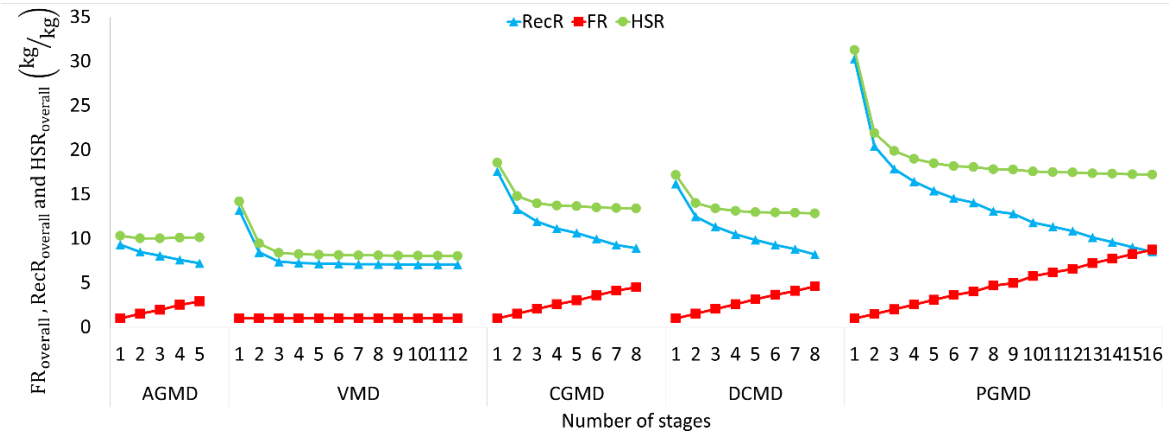

Figure 16. Overall feed, overall recycle and overall heated stream ratios as a function of number of stages

Stagewise water recovery. Figure 17a illustrates the stagewise water recovery at the optimal stage count for the MD configurations studied at a certain total recovery of 67% (corresponding to concentrating feed with 10% salinity to brine with 30% salinity). Except for VMD, the majority of water recovery occurs during the initial stages and reduces dramatically in subsequent stages in other configurations. In VMD, however, with the exception of the final stage, all other stages contribute equally to water recovery, whereas the water recovery from the final stage is almost three times that of the previous stages. This is better explained by the inlet salinity of each stage, as illustrated in the figure 17b. Because of the low single pass recovery of each stage, the inlet and outlet salinities of a stage are very close, and the inlet salinity can approximate the operating salinity throughout the length of that stage. The inlet salinity of successive stages in VMD increases much more slowly compared to that of DCMD and gap type MD. This is primarily because VMD has a different heating and recirculation structure than other configurations.

Interstage heating and recirculation in DCMD and gap type MD systems enables adjustment of each stage's optimal recovery and, thus, operating salinity. Initial stages operating at lower salinities produce more water with less energy consumption due to increased heat recovery and thermal efficiency, resulting in an overall increase in GOR.

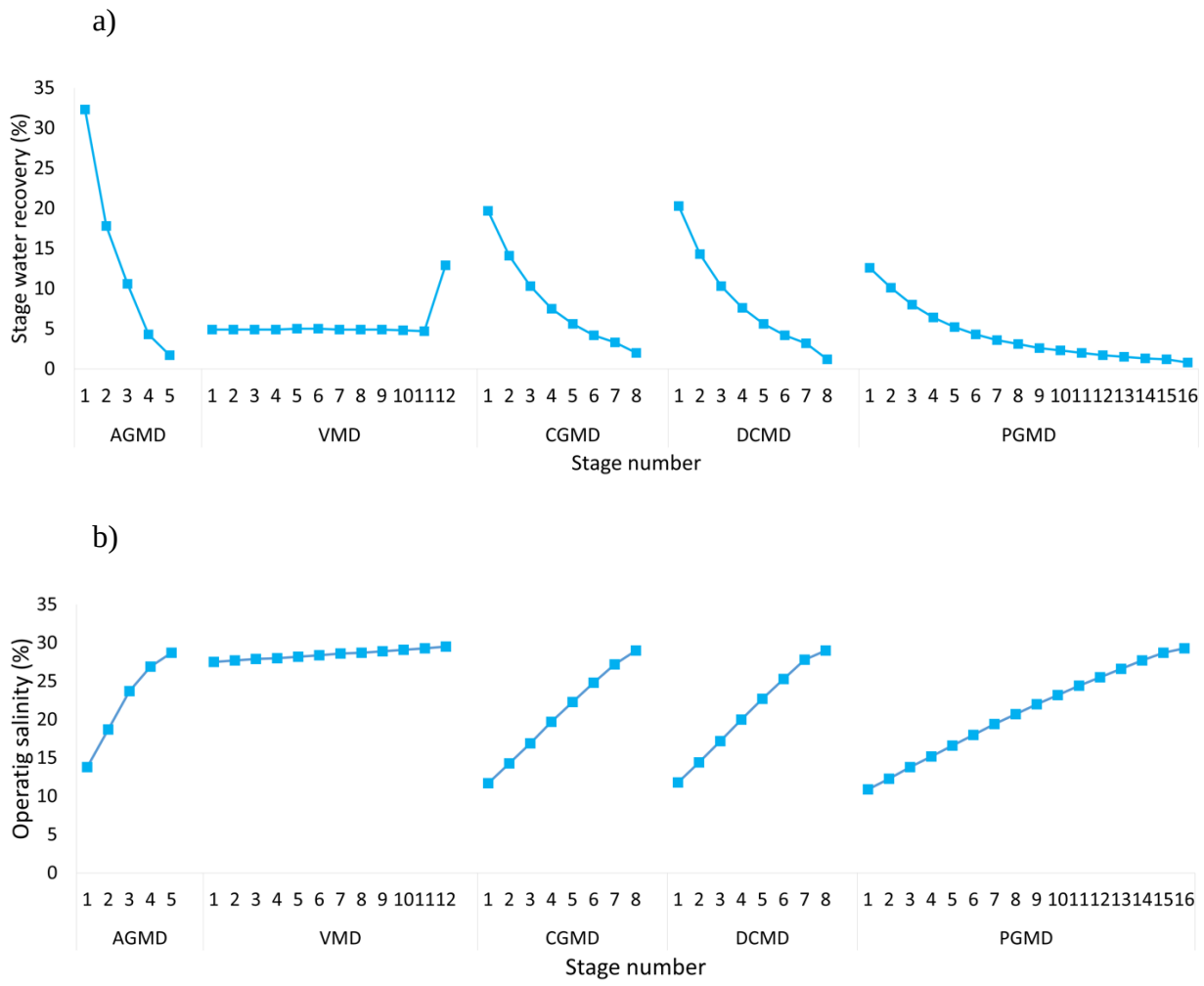

Figure 17. Stagewise water recovery and operating salinity for various MD configurations. The trends in figure 17 a) and b) are presented for the cost optimal solution for all configurations

In the absence of recirculation, the amount of water recovered in each stage of multistage VMD is dependent on cooling capacity of the stage external condensers. Except for the final stage condenser, the flowrate of the coolant stream in all other stage condensers equals the sum of the

recycle stream and the plant feed, resulting in equal water recovery for all stages except the final one. For the final stage, the coolant stream is recirculated in a separate loop and its flow rate is freely adjustable within the model. As a result, the final stage can achieve higher water recovery by having a greater flowrate of coolant than the other stages. Water recovery in other stages can be increased by increasing the recycle stream flowrate. However, this increases the stream flowrate to the heater, and therefore energy consumption. By separating the final stage loop and increasing the final stage water recovery, the recycle stream flowrate to the heater can be reduced. Our findings indicate that for a multistage VMD with 12 stages, the unit treatment cost without a separate cooling loop is 10% higher than the treatment cost with a separate cooling loop for the final stage.

The stagewise water recovery and feed salinity analysis presented here explains the plateauing trend in treatment costs and GOR with increasing number of stages; As the number of stages increases, the operating salinity intervals between stages decrease, which 1) reduces the difference in vapor pressure lowering and energy intensity between consecutive stages. 2) reduces the contribution of all stages to water recovery, including the initial stages with lower salinity, (as illustrated in the figure 38 in the appendix) resulting in a diminishing beneficial effect as the number of stages increases. Similarly, as the number of stages in VMD increases, the amount of water recovered in each stage decreases, lowering the temperature rise in the stream flowing to the heater. As a result, as the number of stages increases, the benefit of stage addition diminishes.

Stagewise membrane area. Figure 18a shows the stagewise membrane area to total membrane area ratio. For DCMD and gap type MD, membrane area is greater in the initial stages and decreases in subsequent stages, whereas for VMD, membrane area increases from the first to

the last stage, with the most significant increase occurring at the final stage. The membrane area of each stage is the product of the stage's specific area and the stage's stream flowrate. We observed that the initial stages of DCMD and gap type MD have a higher water recovery and correspondingly higher amount of interstage stream recirculation. Additionally, as illustrated in figure 39, the specific area is highest for initial stages and decreases stagewise for DCMD, PGMD, and CGMD. As the specific area increases the temperature difference at the module exit increases. The cost-optimal specific area for DCMD, PGMD, and CGMD is primarily limited by the vapor pressure lowering, which limits the temperature difference at the module's exit. As a result, reduction in salinity of initial stages increases the specific area, which results in an increase in both heat recovery and thermal efficiency. Thus, the initial stage area is the largest due to the combined effect of larger specific area, the greater amount of water recovered, and the resulting increased recirculation of streams.

a)

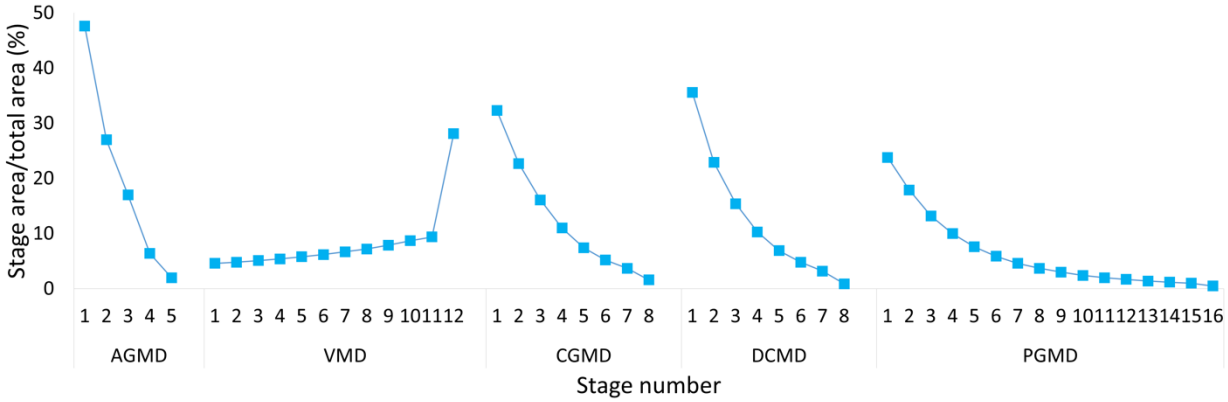

b)

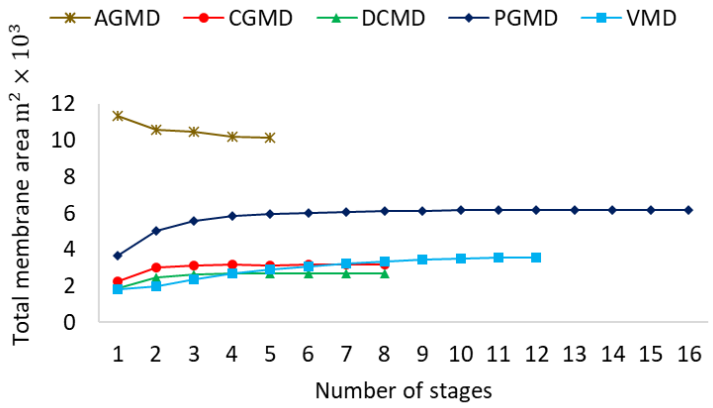

Figure 18. a) Ratio of stage area to the total membrane area for various MD configurations at their optimum number of stages. b) Variation in total membrane area with increasing number of stages

In the case of AGMD, the cost-optimal specific area is determined by both vapor pressure lowering and membrane cost, owing to the large membrane area required for this configuration to operate optimally. Reduced vapor pressure lowering in the first stage with lower salinity enables AGMD to achieve both greater heat recovery and higher thermal efficiency while requiring less area. As a result, considering high volume of water recovery (and corresponding high amount of

feed recirculation), the cost optimum specific area reduces in initial stage of AGMD to bring cost saving by area reduction. The net effect of higher water recirculation and lower specific area lead to higher area in initial stage of AGMD.

In VMD the stage area is lowest for initial stage and increases stagewise. This is because there is not interstage heating in VMD system and each stage operate at lower average temperature across the membrane in comparison to preceding stages. On the other hand, we observed that VMD has an equal amount of water recovery through the initial stages, with the final stage producing the highest recovery. Given the exponential relationship between saturation vapor temperature and pressure, stages with a lower vapor pressure across the membrane require a larger area to maintain the same amount of recovery or a higher recovery than previous stages. Combination of higher water recovery and lower pressure across the membrane result in a more significant increase in stage area in the final stage.

Total membrane area. The variation in total membrane area as a function of the number of stages is depicted in Figure 18b. In comparison, AGMD has the largest membrane area required when operating at its optimal number of stages, followed by PGDM, VMD, CGMD, and DCMD. Except for AGMD, the total membrane area increases as the number of stages increases in all other configurations. This is well justified by the fact that as the number of stages increases, the specific area at the initial stage with the highest share of water recovery increases. The same argument can be used to justify a decrease in the total membrane area for AGMD. As the number of stages increases, the decrease in the specific area of the initial stage that has the greatest portion of the recovery results in a decrease in the total membrane area. However, as the number of stages increases and reaches a plateau, the change in treatment area for DCMD and gap type MD diminishes.

In the case of VMD, the maximum and minimum temperatures throughout the stages are determined by the temperature at the first stage hot channel inlet (or heater outlet) and the chiller bottom temperature. With an increase in the number of stages, this range is subdivided into smaller intervals within stages. This results in greater number of stages with a lower level of saturation vapor pressure across the membrane, which increases the total membrane area as the number of stages increases.

Effect of membrane thickness. The analysis presented so far assumed commercially available PTFE membranes with active layer thickness of 60 micrometer and support thickness of 80 micrometer. It is assumed that only the active layer contributes to mass transfer, as demonstrated in [100], and that the support layer has a negative impact on heat transfer [101]. This type of membrane is relatively thin which results in both higher heat conduction and higher fluxes. It has been shown previously that both GOR and treatment cost of DCMD, PGMD and CGMD improve utilizing membranes with higher thickness. Membrane thickness affects the performance of MD system through altering both conduction thermal resistance and mass flux. Higher thickness decreases the conduction heat flux, thereby increasing the thermal efficiency and GOR of the system. On the other hand, higher thickness decreases the mass flux and requires higher membrane area. We conducted separate optimization considering thickness as a decision variable to obtain optimum thickness value and its effect on the design of multistage DCMD, PGMD and CGMD. VMD and AGMD are not analyzed further because these two configurations have high thermal efficiency due to air gap and vacuum channel and tend to have membranes with smallest thickness possible to increase the flux and avoid large membrane area.

Figure 19a depicts the optimum membrane thickness at various number of stages. It should be noted that in a multistage MD configuration, we assume that the membrane thickness is not

stage specific and membranes with the same thickness will be used for all stages. As the number of stages increase, the optimum membrane thickness decreases for all three configurations. This is a direct result of lower operating salinities in initial stages of multistage MD systems yielding a higher overall efficiency at higher number of stages. Therefore, as the number of stages increase, lower thickness membranes yield the minimum cost by increasing flux and decreasing the required membrane area. In contrast to the previous section result, when optimizing thickness as a variable, the total membrane area decreases as the number of stages increase (Figure 19b). This is because as the number of stages increases, the optimum thickness decreases and the flux through each stage increases, reducing the total membrane area.

Figure 19c compares the optimal treatment cost of multistage DCMD, PGMD, and CGMD configurations with commercial membrane and membrane with optimum thickness. For all configurations, the difference in thickness between optimal thickness membrane and commercially available membrane decreases as the number of stages increase, requiring a thinner thickness closer to that of the commercial membrane used in this study. Another significant finding is that for CGMD and DCMD, increasing the number of stages has a much greater effect on treatment cost reduction than using the optimal thicker membrane, and that when using more than two stages for the case study considered here, using thicker membranes has little effect on cost. However, for PGMD, there is significant reduction in treatment cost with optimally thicker membranes. For instance, by operating with a relatively thick membrane in two or three stages, the unit treatment cost of multistage PGMD approaches that of multistage DCMD and CGMD.

a)

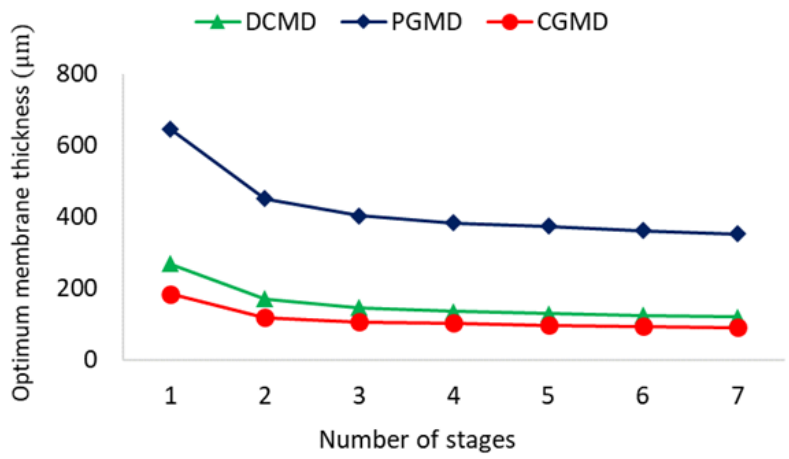
DCMD
PGMD
CGMD
Optimum membrane thickness (µm)
800
600
400
200
0
1
2
3
4
5
6
7
Number of stages

b)

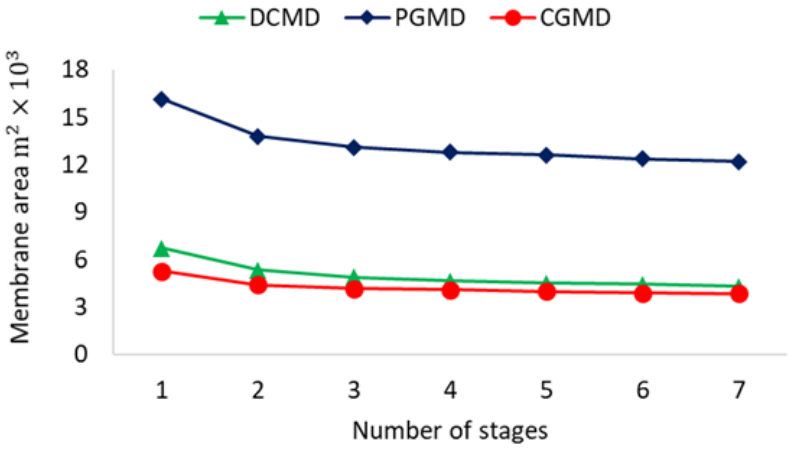
DCMD
PGMD
CGMD
Membrane area m² × 10³
18
15
12
9
6
3
0
1
2
3
4
5
6
7
Number of stages

c)

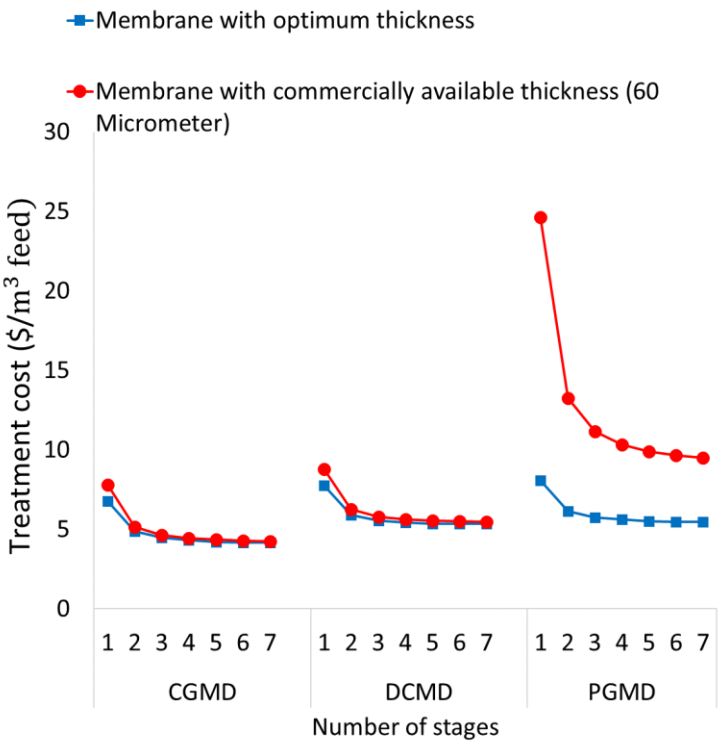

Figure 19. a) Cost-optimal membrane thickness, b) Total membrane area corresponding to cost-optimal membrane thickness, and c) Treatment cost for membranes with commercially available thickness and membranes with cost-optimal thickness as a function of stage count.

Feed salinity-sensitivity analysis. Figure 20 illustrates the GOR, total membrane area, and treatment cost for the studied MD configurations at two different feed salinity levels of 3.5% and 10% and a constant reject brine salinity of 30%. With the exception of multistage VMD, the GOR of all multistage MD configurations increases as the feed salinity increases (figure 20a). This is in contrast to the trend observed for single stage MD, in which salinity reduction has no effect on GOR but increases treatment cost. This is because in multistage systems, lowering the feed salinity enables the majority of the recovery process to occur at initial stages with lower salinity and higher thermal efficiency and heat recovery. On the other hand, as feed salinity increases, the membrane area increases proportionately as the specific area and volume of

recirculating streams increase concurrently. As a result of the counterbalancing effect of increased area and GOR on treatment costs, the treatment costs for PGMD, DCMD, and CGMD all decrease, with the greatest reduction for PGMD, while the treatment costs for AGMD increase (figure 20c). In VMD, the GOR is unaffected by feed salinity, and the treatment cost rises as the area increases. This is because, as with single stage MD systems, the operating salinity of multistage VMD is determined by the reject brine salinity.

a)

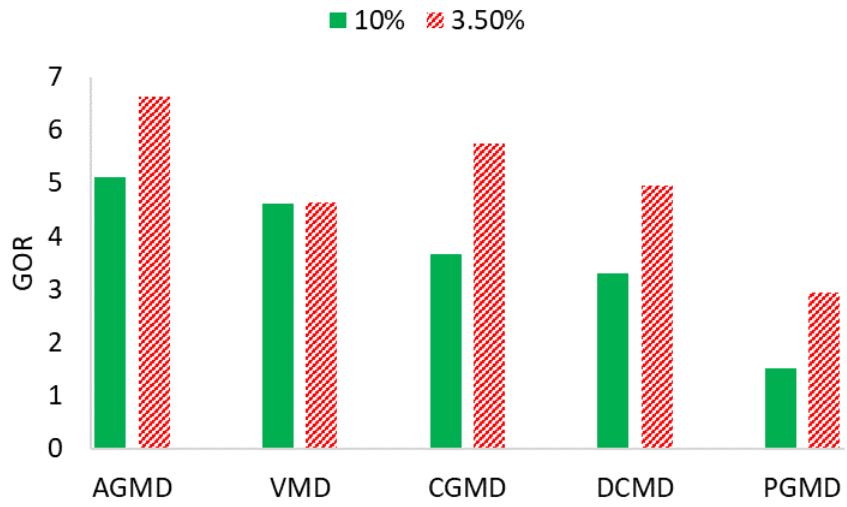
10%
3.50%
GOR
7
6
5
4
3
2
1
0
AGMD
VMD
CGMD
DCMD
PGMD

b)

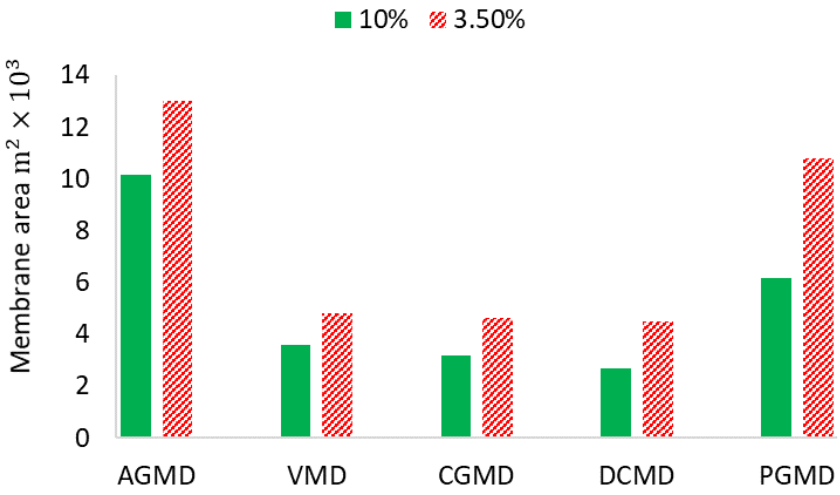
10%
3.50%
Membrane area m^2 × 10^3
14
12
10
8
6
4
2
0
AGMD
VMD
CGMD
DCMD
PGMD

c)

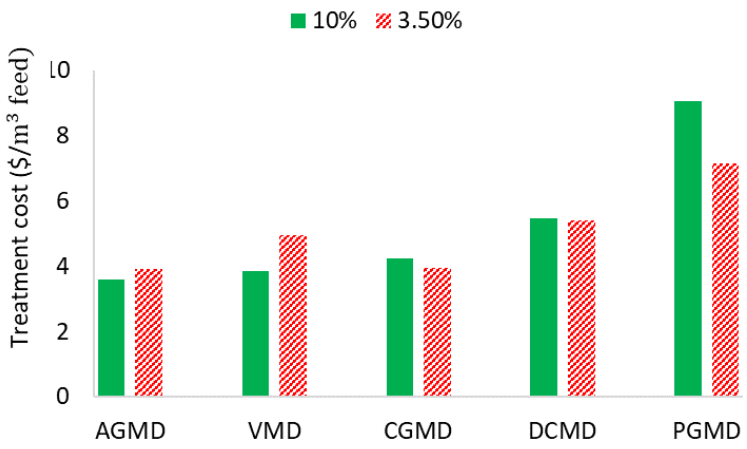

Figure 20. GOR, total membrane area, and treatment cost at two level of feed salinity of 3.5% and 10% for studied MD configurations at their cost optimal number of stages

Operation with free source of cooling. A free source of cooling may be possible in cases such as integration into other processes or having access to a large supply of feed water (e.g. seawater). On this basis, we analyzed the studied MD systems in the presence of a free cooling source, but at a temperature greater than the chiller bottom temperature in the initial analysis (assumed to be 30℃ versus chiller bottom temperature of 10℃). The GOR of all configurations decreases as the temperature differential across the MD module decreases when using a free cooling source (figure 21a). Except for VMD, the total area of all configurations decreases as the smaller temperature difference limits the membrane area (figure 21b). In VMD, with free cooling source at higher temperature, the vacuum pressure drops, lowering the flux and increasing the membrane area. Although the GOR of all MD configurations decreases with free cooling source, the reduction in treatment cost is significant across all configurations.

a)

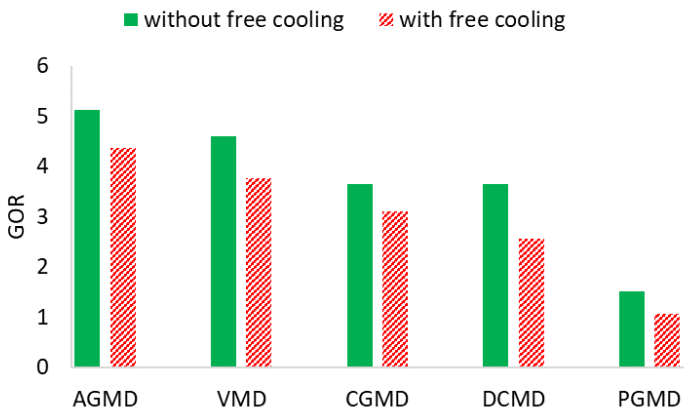

b)

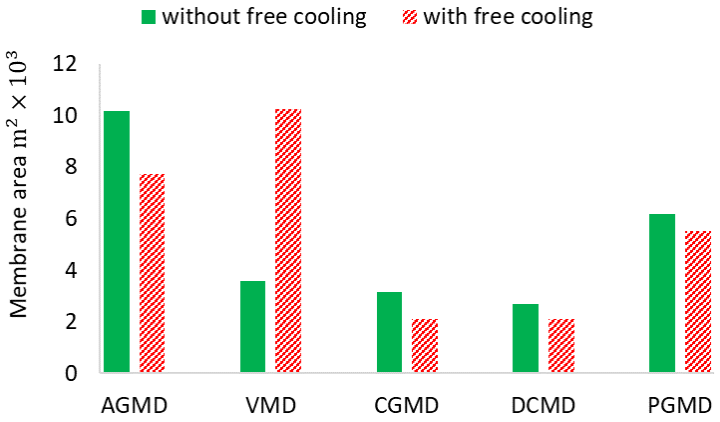

c)

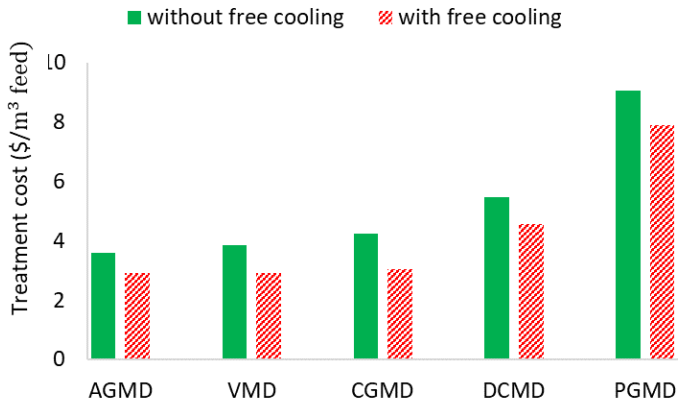

Figure 21. GOR, total membrane area, and treatment cost with and without free cooling source

3.4 Conclusions

This work developed process-based optimization models for five MD configurations operating in multistage operation mode: DCMD, AGMD, PGMD, CGMD, and VMD. The optimization process was carried out with the goal of minimizing the unit treatment cost for treatment of produced water. We specifically investigated and compared the variation in treatment cost, GOR, thermal efficiency, heat recovery, recycle ratio, and membrane area with variation in number of stages. Additionally, we investigated the effect of membrane thickness on the optimal cost for DCMD, CGMD, and PGMD. The analysis was conducted for a hypothetical treatment plant with a capacity of 10 kg/s concentrating hypersaline produced water from 10% to 30% salinity. The major findings are summarized as follows.

- Treatment cost and GOR of all MD configurations improve with increasing number of stages, with VMD and PGMD showing the greatest improvement, with 90 percent and 85 percent improvement in GOR, respectively.

- AGMD with the fewest stages outperforms all other configurations with respect to treatment cost, while PGMD with the most stages yield the highest treatment cost.

- AGMD benefits the most from increased thermal efficiency as a result of reduced area when operating in multistage mode. On the other hand, VMD and PGMD benefit the most from improved heat recovery.

- For DCMD and gap type MD, the water recovery ratio and percentage of stage membrane area are highest in the early stages and decrease in subsequent stages.

- For VMD, the water recovery ratio is the same for all stages except the last, which has the highest water recovery ratio. The stage area in VMD increases from the first to the last stage as the level of saturated vapor pressure across the stage decreases.

- For all configurations, the overall heated stream ratio decreases at first and then shows asymptotic behavior as the number of stages increase.

-Except for AGMD, total membrane area increases as the number of stages increase due to an increase in specific area in DCMD, PGMD, and CGMD, and a higher number of stages with a lower pressure level in VMD. For AGMD, total membrane area decreases to optimize system cost.

-Thickness analysis shows that a higher number of stages with a higher overall thermal efficiency necessitate a thinner membrane for increased flux and a smaller membrane area, and vice versa. For multistage CGMD and DCMD, using optimally thicker membrane has negligible impact on treatment cost, whereas for multistage PGMD, utilizing thicker membranes significantly improves the treatment cost.

The sensitivity analysis of feed salinity revealed that unlike the single stage continuous recirculation MD, the GOR increases across all configurations (excluding multistage VMD) while area increases. The trade-off between increased area and GOR results in a reduction in treatment costs for multistage DCMD, CGMD, and PGMD, but a slight increase in treatment costs for multistage AGMD. As with single stage configurations, the treatment cost of multistage VMD increases with feed salinity. Multistage MD configurations were also analyzed in the presence of a free source of chilling energy but at a higher temperature. The result revealed that the cost of treatment for all MD systems is significantly reduced. Additionally, it was discovered that when chilling costs are eliminated and the chilling source temperature is increased, the total membrane area for multistage DCMD, CGMD, PGMD, and AGMD decreases, whereas the membrane area for VMD increases as the vacuum pressure increases.

4.0 An Optimization-Based Study of Osmotically Assisted Reverse Osmosis Systems for Application in Zero Liquid Discharge Systems

Significant amounts of wastewater generated by water-intensive industrial activities such as shale oil and gas production have sparked grave environmental concern in recent years. One way to address this issue is to desalinate wastewater at a high recovery rate, which reduces reject waste and provides fresh water for beneficial use. Osmotically assisted reverse osmosis (OARO) is a potential desalination method for achieving high recoveries and handling hypersaline brines. The performance, energy consumption, and cost of this system are highly dependent on its configuration. In this study, we present the brine-reflux OARO system and compare it with the commonly discussed configurations, such as cascading osmotically mediated reverse osmosis (COMRO), consecutive loop OARO, and split feed counterflow RO, through a cost-optimization-based framework. We analyze and compare the treatment costs, membrane area, specific energy consumption, and design parameters associated with each of the aforementioned configurations for zero liquid discharge (ZLD) water recovery. Our results indicate that the BR-OARO system with treatment cost of 5.1 US $/m^3 of feed outperforms other configurations in terms of least number of stages, treatment cost, membrane area, and energy consumption.

4.1 Introduction

The growth of water-intensive industries and the wastewater they generate have all contributed to the rise of environmental concerns over the last decades. Processes such as shale oil

and gas production, flue gas desulfurization, and brackish water desalination generate large amounts of brine, which can have a detrimental impact on the environment if not properly managed [9, 77, 80, 102-106]. Given the scarcity of fresh water, the tightening of environmental regulations, and the high cost of brine disposal, recycling hypersaline brine and minimizing waste may be a viable option. This alleviates stress on freshwater resources and mitigates adverse environmental impacts. As such, Zero Liquid Discharge (ZLD), a method that reduces waste to solids while increasing water recovery, is gaining traction in academia as well as industry [15, 16]. The ZLD process entails concentrating water to its saturation salinity limit and then passing it through a crystallizer. Thermal distillation is a common desalination method used to treat hypersaline brine or to increase recovery up to the point of saturation. However, in general, evaporative-based technologies are inefficient in terms of energy consumption due to the phase change involved, which consumes far more energy than the minimum work of separation [107-109].

Having higher energy efficiency in comparison to thermally driven desalination processes, reverse osmosis (RO) is the most widespread technology accounting for 69% of the desalination capacity worldwide [110, 111]**.** RO is a pressure driven separation process utilizing hydraulic pressure to force the solvent (water) to move through a semipermeable membrane from higher solute concentration to lower concentration. The required permeate recovery, or desired concentrate salinity will determine the energy required for separation process. The minimum applied hydraulic pressure in RO process should be at least as high as the terminal osmotic pressure difference (at most concentrated state of the feed solution) so that permeation occurs across the entire available membrane area [112]. This implies that higher recovery ratios, or higher feed salinities increase the required applied hydraulic pressure, impacting the economic feasibility of

the process by increasing both capital and operating costs. In addition, the applied hydraulic pressure is limited by the maximum pressure that RO membranes could withstand.

Multi-stage RO (MSRO) systems have been suggested to decrease the required energy of separation through stage-wise increase in the terminal pressure difference [113]. The energy savings in this configuration arise from operating the system at higher feed flowrates with lower terminal pressure difference corresponding to lower brine salinities at initial stages, and reduced feed flowrate with higher terminal pressure difference at latter stages [112, 114, 115]. Although MSRO configuration could result in energy savings, the problem of maximum allowable pressure for RO membranes still remains an issue for high permeate recoveries and high feed salinities such as those encountered in shale gas wastewater applications [35].

Osmotically assisted reverse osmosis (OARO) systems are emerging RO configurations that enable the pressure driven membranes to treat hypersaline solutions [30, 31]. OARO overcomes the problem of excessive hydraulic pressures by introducing a saline solution stream on the low-pressure side of the membrane leading to reduction in transmembrane osmotic pressure difference [30, 32-34]. Permeate donating saline feed is concentrated on the high-pressure side of the membrane, while permeate receiving saline stream is diluted on the low-pressure side of the membrane. This process is also referred to as countercurrent flow reverse osmosis (CFRO) given the fact that the concentrating and diluting saline solution flow (move) in the opposite direction. In this countercurrent flow mode, the concentration of both feed and saline solution increase in the feed flow direction along the module which minimizes the local osmotic pressure difference and increases the system's second law efficiency by creating a balanced driving force throughout the module [37, 116]. OARO system mainly produce concentrate of high salinity and cannot produce fresh pure water on its own. Therefore, OARO is usually coupled with a RO process for freshwater

production [117]. In fact, the diluting solution serves as a medium for delivering the permeate from the OARO's high saline feed to the RO system for separation.

Various OARO configurations have been proposed in the available literature. The key difference among various OARO systems is the source of saline diluting solution stream on the low-pressure side of OARO unit, which could be: 1) working solution, 2) concentrate, and 3) feed stream. Depending on the plant makeup feed salinity and choice of the configurations, plant makeup feed may enter the system as: 1) diluting stream of the OARO unit, 2) feed stream of the RO unit, and 3) concentrating feed of the OARO unit. Depending upon the desired product recovery, size and energy consumption of the system, each of the mentioned OARO systems may be configured in multi-stage operation mode. Furthermore, RO unit itself could be designed in multi-stage configuration for energy efficiency.

The most frequently discussed OARO configurations in the published literature are consecutive loop osmotically assisted RO (CL-OARO) [36, 116], split feed counterflow RO (SF-CFRO) [37], and cascading osmotically mediated RO (COMRO) [35], the details of which will be discussed in the following sections. To achieve high recoveries, CL-OARO and SF-CFRO require multiple stages, which adds to the design complexity of these systems. On the other hand, regardless of number of stages, recovery is extremely limited for the COMRO configuration which is developed based on the same premise as MSRO (i.e. energy savings through stage-wise increases in terminal pressure difference).

In this study, we present the rarely discussed brine reflux osmotically assisted RO (BR-OARO) configuration, which, in contrast to CL-OARO and SF-CFRO, is capable of achieving high recoveries without the use of multiple stages. Additionally, similar to COMRO, BR-OARO can be configured with cascaded stages for energy savings. We develop mathematical models of

the BR-OARO, COMRO, SF-CFRO, and CL-OARO configurations at the module scale and compare their maximum achievable recovery, energy consumption, cost, and membrane requirement using an optimization-based framework. Furthermore, we investigate the underlying cause of the limitation of CL-OARO and SF-CFRO recoveries in a limited number of stages. In addition, we investigate whether cascading stages in series (as in COMRO and BR-OARO) save energy in OARO systems in the same way that MSRO systems do. Finally, we conclude the manuscript with a sensitivity analysis of the feed salinity and burst pressure of the membrane.

a)

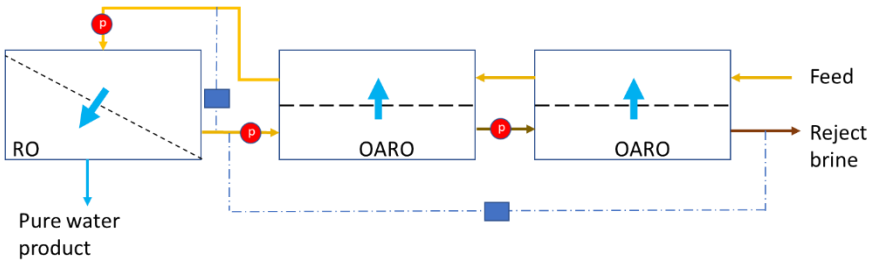
RO
OARO
OARO
Feed
Reject
brine
Pure water
product

b)

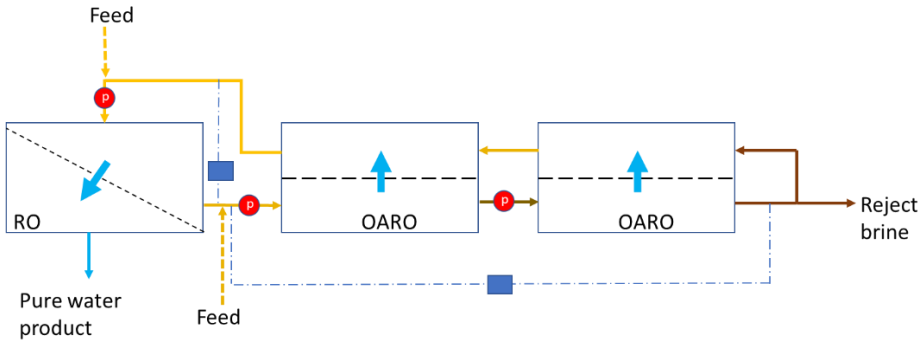
Feed
RO
OARO
OARO
Reject
brine
Pure water
product
Feed

c)

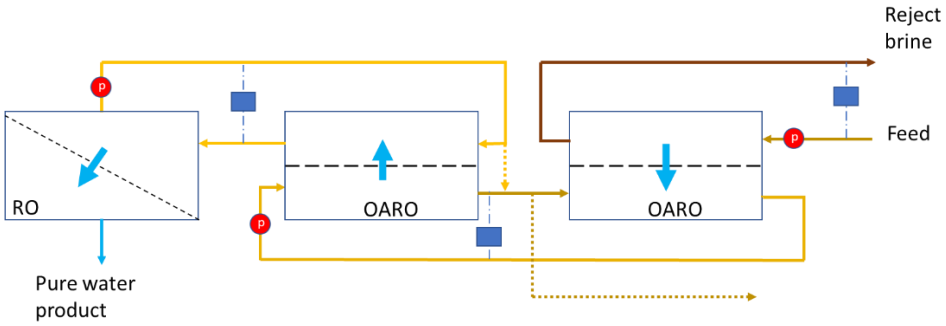
Reject
brine
Feed
RO
OARO
OARO
Pure water
product

d)

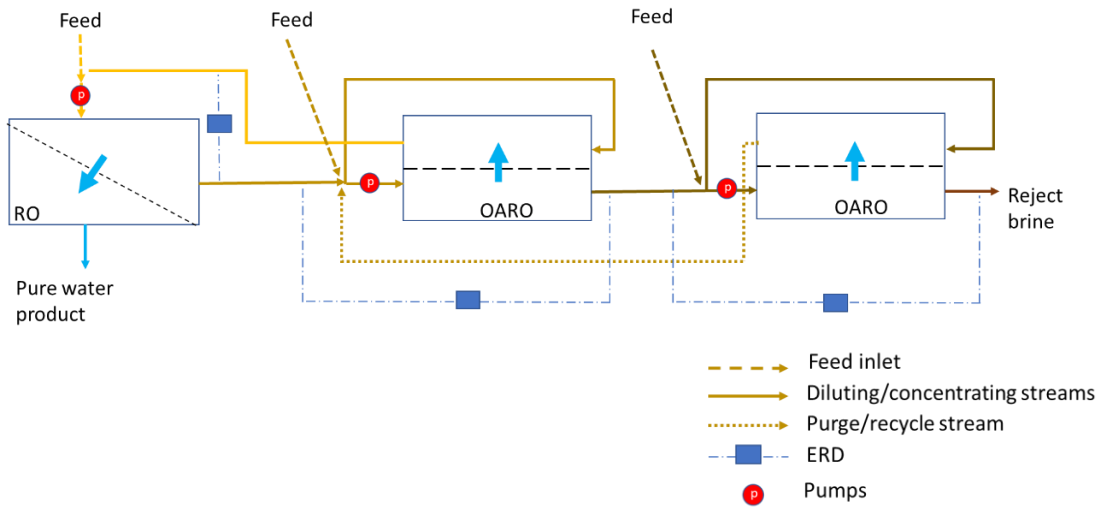

Figure 22. CFRO configurations: a) COMRO b) BR-OARO, c) CL-OARO, d) SF-OARO

4.2 Methodology

4.2.1 Process Description

COMRO- The COMRO configuration is illustrated in Figure 22a. It consists of an initial RO stage followed by multiple stages of CFRO modules connected in series. The plant feed enters the system through the inlet of the last CFRO stage's diluting stream channel. Except for the first CFRO stage, the diluting stream exiting each CFRO stage enters the preceding stage's diluting stream channel. However, the diluting stream that exits the first CFRO stage enters the RO stage as a concentrating stream. The reject stream from the RO stage is directed into the first CFRO stage as a concentrating stream. Similarly, the concentrating stream exiting each CFRO stage enters the following CFRO stage for further concentration, and the plant reject stream exits the

system at the final CFRO stage. This configuration makes use of two energy recovery devices (ERDs). One is used to recuperate the energy contained in the RO reject stream and pressurize the RO inlet stream. The level of depressurization and pressure of the stream entering the first CFRO concentrating channel will be determined through optimization. The second ERD device is assigned to recover energy from the system's reject brine and to pressurize the stream entering the first CFRO stage. The model is based on the assumption that the reject brine is completely depressurized.

As discussed in [37], one issue with the COMRO configuration is the imbalance of the system flowrates on the concentrating and diluting sides. The flowrate of the dilute stream is highest at the diluting outlet of the first CFRO stage (entrance of the RO stage) in COMRO, whereas the flowrate of the inlet of the concentrating stream of the first CFRO stage (corresponding to RO outlet) is significantly lower due to dewatering in the RO stage. Because of the flowrate imbalance, changes in salinity on the concentrating side are greater than those on the diluting side, resulting in an osmotic pressure difference imbalance throughout the system.

Brine Reflux (BR)- OARO- The BR-OARO configuration is depicted in Figure 22b. As with COMRO, it consists of an initial RO stage followed by a train of CFRO stages, with each stage's reject concentrate serving as the concentrating stream for the subsequent stage. A portion of the concentrate reject brine exiting the final CFRO stage is recycled into the final stage's diluting channel as a diluting stream. The diluting stream with the lowest salinity exits the first CFRO and flows to the RO stage to produce permeate. Feed can enter the process at multiple locations in this configuration, including the inlet or outlet of the RO or any CFRO stages. The ERD devices operate similarly to those described in the COMRO configuration.

Although the BR-OARO configuration appears to be similar to the COMRO configuration, we will demonstrate that the imbalance problem associated with COMRO does not exist for BR-OARO due to the presence of the recirculating stream and the choice of optimum feed entrance location (elaborated further in the stage flowrate and salinity section).

Consecutive loop (CL)- OARO- The CL-OARO configuration depicted in Figure 22c employs a sweep solution as a diluting agent that may or may not contain the same constituents as the plant feed. Additionally, it is capable of using draw solution as a sweep solution, similar to the forward osmosis process. The plant feed enters the final CFRO stage's concentrating stream channel, and the reject brine exits the system through the same final stage. The diluting stream exiting each CFRO stage serves as the concentrating stream for the preceding stage. As a result, the first CFRO stage's diluting stream serves as the concentrating stream of the first RO stage, where fresh water is produced. Due to the membranes' imperfect salt rejection, a portion of the dilute stream at the inlet of the diluting channel of each stage is recycled to the inlet of the diluting side of the subsequent stage. This maintains steady state operation and prevent salt buildup in one loop. The recycle stream from the final stage is purged. Due to the fact that the concentrating stream exiting each stage serves as the diluting stream for the following stage, it is completely depressurized, and its energy is recovered by the concentrating stream entering the same stage.

Split-Feed (FS) CFRO- Figure 22d depicts the SF-CFRO configuration. Each stage's concentrating and diluting solution is sourced by a mixture of reject brine from the previous stage and diluted solution exiting the subsequent stage. This mixture is split by a ratio (referred to as split feed ratio in this study) between the sides of each stage. The dilute solution that exits the first CFRO stage flows into the initial RO stage for freshwater recovery, while the RO reject outlet flows to the CFRO stages for further concentration. The final CFRO stage's concentrate stream

exits the system as reject brine. As with the BR-CFRO system, feed can enter the SF-CFRO system at a variety of locations, including the RO or CFRO stages' inlet and outlet. Each stage has one ERD device assigned to recover energy from the exiting concentrate and pressurize the stage's entering concentrate.

Choice of membrane- The operation of salinity gradient membrane-based separation processes is affected by concentration polarization (CP). CP occurs when the solute concentration increases and decreases near the membrane surfaces at the boundary and support layers of the concentrating and diluting channels, respectively. This reduces the driving force of separation through increasing the osmotic pressure gradient across the membrane. For RO membranes with pure water on the permeate side, CP occurs only on the feed concentrating side. However, CP occurs on both sides of bilateral modules in CFRO processes with saline solution on the concentrating and diluting sides. Specifically, the presence of a support layer on the dilute side intensifies CP, impeding the separation process further. The CP is affected by the support layer structural parameter that is directly correlated to the thickness and tortuosity and is inversely correlated to the porosity of the support layer. Reduced structural parameters improve permeate and diluting solution mixing, resulting in less concentration polarization. However, membranes with a lower structural parameter (for example, forward osmosis (FO) and pressure retarded osmosis (PRO) membranes) have a lower strength and burst pressure, typically less than 24 bar [118-121], which limits the applied hydraulic pressure for the separation process. Meanwhile, Straub et al. [122] conducted a study in which the burst pressure of the PRO membrane was boosted to around 50 bar using feed spacers. Therefore, we will use the same membrane characteristic and burst pressure as in [122] as an optimistic yet feasible choice for CFRO membranes given current advances in membrane technology. The maximum burst pressure for the

initial RO stage is assumed to be 85 bar, which is typical for seawater desalination reverse osmosis (SWRO) membranes. The characteristics of both RO and CFRO membranes are listed in Table 16 in the appendix.

Modeling CFRO process- Individual CFRO stages operate identically in all CFRO configurations; the primary differences arise from the source of diluting and concentrating solution and the manner in which CFRO stages are connected to one another. Each CFRO stage is composed of a series/or parallel arrangement of CFRO modules, the combination of which determines the stage's total width, length, and area.

we developed unique mathematical models for each of the BR, CL, and SF configurations. To model the large-scale modules, we used a discretization method in which each stage of the RO and CFRO modules is divided lengthwise and mass and energy balances are calculated for each slice. The common equations used to model the process are discussed here, and the detailed equations and correlations for each configuration are listed in tables 19 to 23 in the appendix.

The membranes used in this study are not ideal in terms of salt rejection, and there is salt flux through the membrane in addition to water flux. As a result, the total mass flux passed through each membrane slice is equal to the sum of salt and water fluxes (equation 31).

$$j_{total}^{i,z} = j_w^{i,z}\rho_w^{i,z} + j_s^{i,z} \tag{31}$$

The water permeability coefficient and the pressure difference across the membrane determine the water flux. The pressure on each side of the membrane is the sum of the osmotic pressure near the membrane surface and the applied hydraulic pressure (Equation 32).

$$J_w^{i,z} = a_w\left(P_c^{i,z} - P_d^{i,z} - OP_{c_m}^{i,z} - OP_{d_m}^{i,z}\right) \tag{32}$$

The osmotic pressure is proportional to the salinity and temperature of the stream via the osmotic coefficient (equation 33).

$$OP_{c_m}^{i,z} = \frac{iRT}{M_w} C\varphi \tag{33}$$

Salt flux through the membrane is a function of salinity gradient across the membrane and is calculated using the membrane salt permeability coefficient (equation 34).

$$J_s^{i,z} = a_s\left(C_{c_m}^{i,z} - C_{d_m}^{i,z}\right) \tag{34}$$

The change in flowrate across each membrane slice is the product of the area and total mass flux received or donated for diluting and concentrating solution, respectively (equations 35 and 36).

$$M_{C_{out}}^{i,z} = M_{C_{in}}^{i,z} - \left(J_w^{i,z} \times \rho_w + J_s^{i,z}\right)L^{i,z}W^{i} \tag{35}$$

$$M_{d_{in}}^{i,z} = M_{d_{out}}^{i,z} - \left(J_w^{i,z} \times \rho_w + J_s^{i,z}\right)L^{i,z}W^{i} \tag{36}$$

The pressure drop per unit of membrane length is equal to the change in hydraulic pressure across each slice of the membrane for both diluting and concentrating (equation 37):

$$P_{C/d_{in}}^{i,z} - P_{C/d_{out}}^{i,z} = PD_{c/d}^{i,z}L^{i,z} \tag{37}$$

The remaining modeling consists of developing equations that connect slices of one RO or CFRO module, developing equations that connect the stage specific to each type of OARO

configuration, modeling the high-pressure pump, recirculation/booster pump, and energy recovery devices based on their location within the system.

Optimization model- We develop a non-linear optimization model for each of the studied OARO configurations using the mathematical models developed for each configuration and representative cost equations for capital (membrane and pumps) and operating costs (electricity, membrane replacement, pretreatment, labor, and maintenance). Within the optimization model, the stream's pressure, salinity, and flowrate are independent variables, while the dimensions of each stage, the size of the pumps, and the ERD devices are dependent variables. The developed non linear programming models are implemented in GAMS software and solved with the CONOPT4 solver. We run the optimization model of each configuration for two set of optimization objective. One objective is to determine the maximum amount of water that each configuration can recover under specified conditions, and the second objective is to determine the minimum cost associated with achieving a certain level of water recovery by each configuration. The stage count is specified as a known parameter in the optimization model, and the effect of changing the stage count on the obtained result is investigated by running the optimization model multiple times with the stage count changed.

4.3 Result and Discussion

We ran an optimization model for a hypothetical plant treating 10 kg/s produced water with 10% salinity and 74% pure water recovery, which corresponds to reject brine at saturation conditions, in order to make the system compatible with crystallizers for ZLD operation. Tables

16 to 18 in the appendix provide the model input parameters, including plant characteristics, membrane properties, and capital and operating cost data.

Maximum recovery- Figure 23 depicts the maximum achievable recovery versus the number of stages for two pressure levels of 20 and 50 bar for a 10% feed salinity. The stage count excludes the initial RO stage and only includes CFRO stages. For a 10% feed salinity, 74% water recovery corresponds to the reject brine's saturation salinity or ZLD condition (as shown by a yellow line in Figure 23). The BR configuration outperforms the COMRO, CL and SF configurations by achieving ZLD conditions at a pressure as low as 20 bar and with only one CFRO stage. The maximum water recovery of the CL and SF configurations increases as the number of stages increases, and both configurations require a larger number of stages to achieve ZLD recovery at lower pressure levels. Water recovery in the COMRO configuration is independent of the number of stages and only varies with applied hydraulic pressure, and at applied hydraulic pressures of 20 and 50 bar, COMRO recovers significantly less water than ZLD.

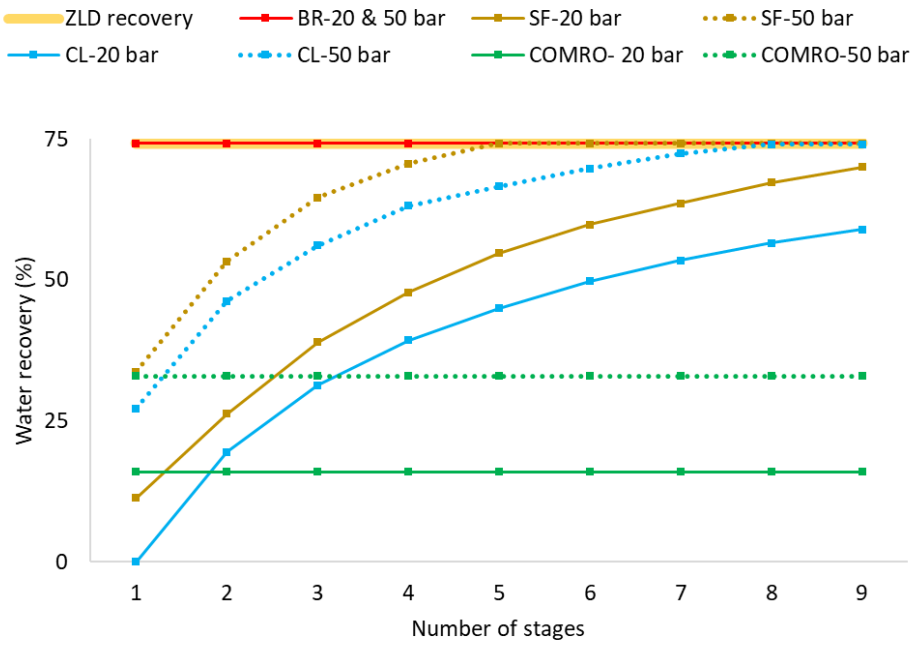

Figure 23. Maximum possible recovery vs. number of stages for CFRO membrane at two maximum pressure levels of 20 and 50 bar for feed containing 10% salinity. The maximum pressure in the RO stage is assumed to be 85 bar.

The applied pressure and terminal concentration difference (corresponding to terminal osmotic pressure difference) at the CFRO module's exit determine water recovery or final reject brine salinity in any CFRO configuration. The terminal concentration difference is determined by the diluting stream inlet salinity that enters the system at the point where reject brine exits the system. For a given recovery, the lower the applied pressure, the higher the diluting concentration required at the module exit. Since higher levels of recovery necessitate a dilute solution with high salinity at the CFRO module's exit, it is commonly assumed that CFRO should be configured in multiple stages (such as CL and SF configurations) to reduce the diluting solution concentration to a level treatable by the RO stage. However, we've just shown that the brine reflux configuration can achieve ZLD recovery with only one CFRO stage. This means that in a single stage CFRO module, the concentration of diluting stream (or recycle stream in the case of BR) with the same salinity as the reject brine at saturation concentration is reduced to a salinity treatable by RO.

The primary reason that SF and CL configurations require multiple CFRO stages to achieve a high level of recovery is that a single stage SF and CL configuration imposes a salinity limitation on the stream at the inlet of the diluting channel. As shown in figure 23, single stage CL and SF configurations can only achieve 27% and 33% recovery at 50 bar applied pressure. In a single stage CL configuration, the diluting side's inlet salinity is constrained by the RO outlet salinity, thereby constricting the terminal osmotic pressure difference, recovery, and concentrate stream outlet salinity. Additionally, in multiple stage CL, the increase in recovery with each additional stage is limited. This is because, in CL configuration, each stage's diluting solution inlet salinity is equal to the concentrate stream outlet salinity of the preceding stage, which is limited by the

preceding stage's diluting solution inlet salinity. As a result, the restriction imposed by the first RO stage's outlet salinity (not the inlet salinity) propagates throughout the subsequent CFRO stages, requiring the system to operate at a high number of stages to achieve the desired level of recovery. If we had an unlimited supply of saline dilute solution, we could have configured CFRO in open end form rather than closed loop and achieved high recoveries in just one stage by using the high salinity solution that exit the RO stage without returning back to the CFRO module.

Likewise, recovery in a single stage SF configuration is constrained by the salinity of the RO reject (and feed salinity if feed is introduced after the RO stage). This is because the diluting and concentrating streams have the same inlet salinity as the previous stage's reject stream. To maximize recovery, multiple split feed stages should be connected together, each with a recovery limitation imposed by the stage feed salinity. The same rationale justifies COMRO's limited recovery, which cannot be increased by adding CFRO stages, because the inlet salinity of the final COMRO stage's diluting stream is always limited by the feed salinity.

Rather than dealing with the complexities and limitations of the CL and SF configurations, we can simply recirculate the brine as in the BR configuration to achieve high recovery in just one stage or multiple stages in series. In the following sections, the performance of the BR, CL, and SF configurations will be discussed in greater depth.

COMRO's water recovery is extremely limited at the study's maximum burst pressure of 50 bar. As a result, this configuration is excluded from the remainder of the manuscript's analysis, as it is incapable of achieving the ZLD condition.

a)

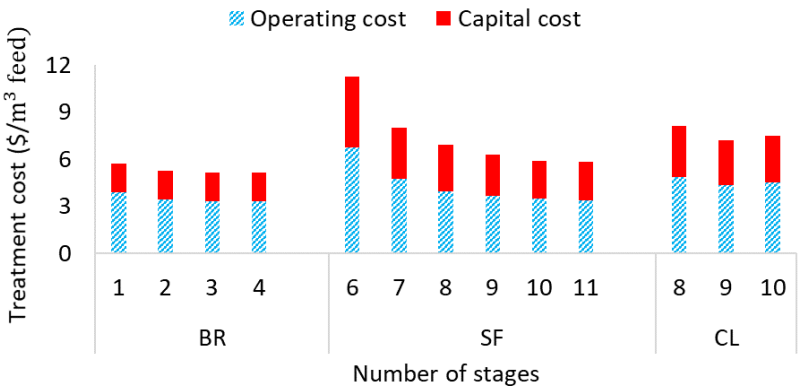
Operating cost
Capital cost
Treatment cost ($/m3 feed)
12
9
6
3
0
1 2 3 4
6 7 8 9 10 11
8 9 10
BR
SF
CL
Number of stages

b)

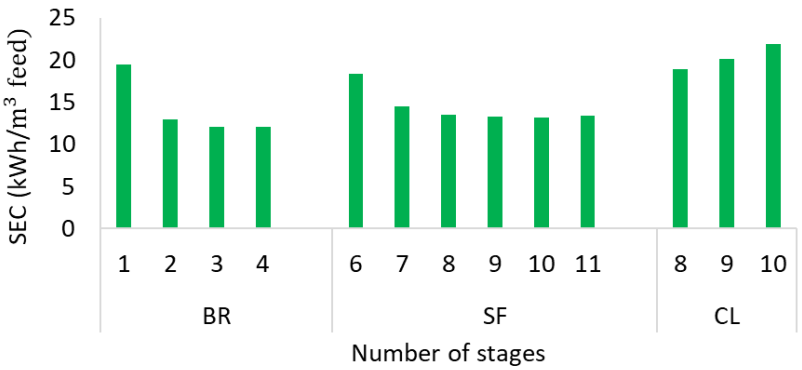
SEC (kWh/m3 feed)
25
20
15
10
5
0
1 2 3 4
6 7 8 9 10 11
8 9 10
BR
SF
CL
Number of stages

c)

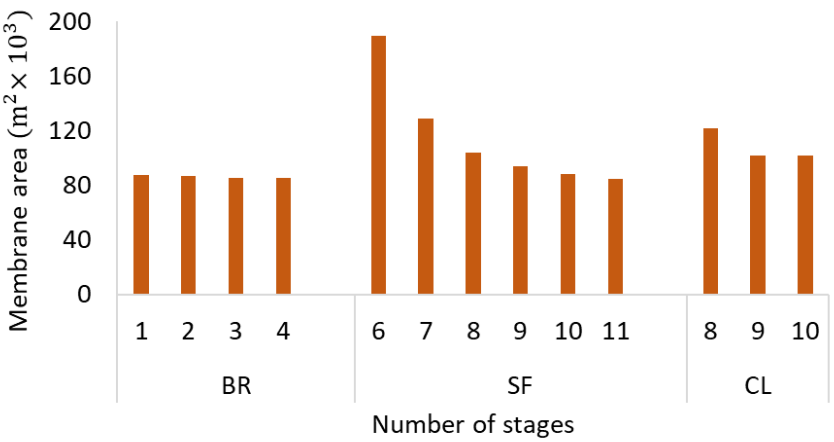

Figure 24. a) Treatment cost, b) Specific energy consumption, c) Total membrane area versus number of stages for BR, SF, and CL configurations (the stage counts exclude the initial RO stage)

Treatment cost. We investigated the effect of feed inlet location on treatment cost in single stage BR and SF configurations since these two configurations allow for multiple feed inlets (figure 40 in the appendix). In order to determine the optimal feed inlet location based on salinity, we ran the analysis for two salinity levels: 3.5% and 10% (this salinity level is also close to the maximum salinity that RO reject can achieve at 85 bar burst pressure). We compared two potential feed entrance locations: one at the RO inlet and another at the RO outlet. Our findings show that for both BR and SF, the lowest cost is obtained when feed enters the system at the RO outlet for 10% salinity feed, and the lowest cost is obtained when feed enters the system at the RO inlet for 3.5% salinity feed. This is due to the fact that if high salinity feed enters the system at the RO inlet, it either raises the inlet salinity or increases the volume of recirculated diluting solution from the subsequent CFRO stage to keep the RO inlet salinity low. Both of the aforementioned system changes increase the system's energy consumption. Similarly, introducing low salinity feed at the RO outlet dilutes the concentrated stream, increasing the energy and membrane area required for reconcentration. On this basis, we continue our analysis in the subsequent sections of the

manuscript for 10% feed salinity entering SF and BR systems at the RO outlet prior to the first CFRO stage.

The variation in treatment costs as a function of the number of stages is depicted in Figure 24a. The analysis of SF and CL configurations begins at 6 and 8 stages, respectively, as this is the minimum number of stages required to achieve the maximum recovery corresponding to saturation salinity under ZLD conditions. For the BR configuration, increasing the number of stages up to three results in a cost savings of approximately 10%, after which the cost savings become very marginal. For the SF configuration, increasing the number of stages initially results in a significant cost reduction of around 47% and then reaches a plateau after ten stages, similar to the BR trend. The cost of treatment for CL is minimum at nine stages, one stage more than the minimum number of stages required for ZLD, and increasing the number of stages further increases the cost of treatment. As a result, the optimal number of stages for BR, SF, and CL configurations are 3, 10, and 9 stages, with treatment costs of 5.1, 5.9, and 7.22 $\$/m^3_{feed}$, respectively. This demonstrates that BR outperforms two other configurations in terms of cost and stage count.

The cost breakdown analysis in Table 14 demonstrates that membrane capital and replacement costs, as well as electricity costs, account for the majority of the treatment cost and are the primary reason for the difference in treatment cost with varying stages and between different configurations. The following sections will demonstrate the underlying reason for energy and cost savings associated with multiple CFRO stages.

Total specific energy consumption. Figures 24b illustrate the change in specific energy consumption (SEC) as the number of stages increases. All configurations have roughly similar SEC at their smallest number of stages (1, 6, and 8 for BR, SF, and CL, respectively), which decreases for BR and SF configurations as the number of stages increases. In the CL configuration,

however, SEC rises as the number of stages increases. According to our findings, the reduction in SEC of BR and SF with increasing number of stages is directly influenced by the Reynolds number (Re) lower bound (minimum allowable Reynolds number) within the model. While higher Re values promote mixing and decrease CP, resulting in increased flux and decreased membrane area, they also increase the pressure drop along the module.

Our analysis demonstrates that, despite the CP effects, the cost-optimal design for CFRO modules tends to reduce Re to the lowest allowable value (Re of 100 in case of the presented results above). CFRO membranes, regardless of their Re value, operate over large areas with low fluxes. As a result, the small reduction in membrane area cost at higher Re is heavily outweighed by the increased electricity cost due to the large pressure drop across large membrane areas. In CFRO stages, the flowrate of both diluting and concentrating streams reduces along the module in the same direction with concentrating stream flow. Therefore, in a single CFRO stage, where the width is the same throughout the module, terminal point of the stage will have the lowest flowrate with lowest Re. Therefore, as we constraint the lower bound on Re, the cost optimum design will assign this lowest Re value to the terminal point within a stage which determine the maximum possible width of that stage. Therefore, in case of single stage CFRO, initial part of the module with high flowrate will have high Re and high pressure drop due to the limited width determined by terminal flowrate and minimum Re which result in high SEC. This limitation could be addressed in two ways: 1) with relaxing the lower bound on Re. This way the width throughout one stage could be increased and the pressure drop in initial part of the module with high flowrate decreases. 2) Design system in multiple stages, where staging provides the opportunity to change the width along the concentrating flow direction. This way, terminal flowrate of each stage will determine the width of that stage according to the minimum allowable Re. With constant Re lower bound, initial stages

with higher flowrate can have higher width and lower Re and pressure drop resulting in energy saving. Our analysis for BR-OARO configuration show that as the Re number increases, higher number of stages are required to prevent the pressure drop.

Previous explanations clarify why SEC of SF and BR configurations reduces with increasing stages while this is not the case for CL configuration. For CL, stages are not connected in series and the flowrate change occurs along each stage independently. Therefore, each stage of CL act like single stage BR and adding additional looping stage not only does not reduce the SEC, but it increases the SEC due to an additional pressurization and circulation required. Therefore, the SEC of CL with 9 number of stage is equal to the SEC of single stage BR. Therefore, if we want to see the improvement in SEC as in BR and SF, each independent stage of CL should be subdivided to multiple stages in series which adds to the complexity of the design. To conclude, BR, SF, CF have 12.1, 13.1, and 20 kWh/m^3_{feed} at their cost optimum number of stages which shows that BR again is superior with regard to energy consumption. For the case of SF, SEC is also affected by variation in membrane area and split feed ratio with number of stages which will be explained in the following sections.

Total membrane area. Figure 24c depicts the total membrane area as a function of number of stages. For BR, the area changes very marginally as the number of stages increases; thus, the improvement in BR treatment cost with increasing number of stages is primarily attributed to the reduction in SEC while capital cost remains constant. For CL and SF configurations, increasing the number of stages from the minimum to the optimal number reduces the total membrane area by 50% and 15%, respectively. This is because CL and SF rely on stage-wise increase in recovery to achieve the desired level of reject brine salinity and freshwater production. As a result, given a fixed amount of total water recovery, the permeate production and concentrating stream's outlet

salinity of individual stages increase as the number of stages decreases. Given the limited inlet salinity of the diluting solution in each stage of CL and SF, increased permeate production (or reject brine salinity) results in a larger terminal osmotic pressure difference for each individual stage. This reduces the average flux and increases the area required for each stage and the total membrane area. Similarly, increasing the number of stages enables each stage to operate with a lower terminal osmotic pressure difference, a higher average flux, and a smaller area requirement. In the CL configuration, increasing the number of stages results in a lower relative reduction in area when compared to the SF configuration. Only one additional stage is required beyond the minimum number of stages in the CL configuration to reduce the total membrane area and treatment cost. Further increasing the number of stages not only has no effect on the total membrane area, but also increases the cost of treatment. This is because each additional stage of CL configuration adds an independent stream loop with a flowrate that is roughly equivalent to the plant feed (figure 25a. This will be elaborated further in the next section). As a result, the added area of the new stage compensates for the reduction in area of each stage, and the treatment cost rises as more power is required to pressurize and circulate the flow in the added stage.

In the case of a BR configuration, no such restriction on dilute inlet salinity exists, and the system does not rely on stage-wise salinity increase to achieve the desired recovery. As a result, area is reduced only slightly as a result of the slight increase in water flux caused by the reduced pressure drop described in the previous section. To summarize, the total membrane area of the BR, SF, and CL is 85.4, 86.3, and 101.9 thousand square meters, respectively, demonstrating the superiority of the BR configuration over the other two configurations when taking into account the simplicity of the design in BR.

Stage flowrate and salinity. The figures 25a and 25b illustrate the stage flowrate and salinity of the investigated CFRO configurations at their cost optimum stage count. The difference between the inlet and outlet of each stage's concentrating or diluting stream (corresponding to the vertical distance between the solid and dashed lines in figures 25a and 25b) represents the permeate production and salinity rise during that stage. For BR, the majority of permeate production and concentration rise occurs during the initial stage, when salinity is lowest and flowrates are greatest, and permeate production decreases during subsequent stages. Similarly, the initial stage of SF produces the greatest amount of permeate (though not as much as the initial stage of BR due to the SF stages' limited recovery potential), which gradually decreases stage by stage.CL requires that all stages produce approximately equal amounts of permeate in order to maintain the system's steady state operation and mass balance.

It is worth noting that the BR-OARO configuration achieves an appropriate balance of diluting and concentrating flowrates due to the presence of the recycle stream and the location of the feed entrance. For high salinity feed, the plant feed is added to the first CFRO stage's concentrating inlet after the RO dewatering process, based on the optimum location determined in previous sections. This compensates for permeate loss in the RO stage, and the flowrate difference (between the diluting outlet and the concentrating inlet of the first CFRO stage) decreases to the volume of reject brine, which is significantly less than the volume of permeate in high recovery cases. Furthermore, if the feed salinity is low, the optimum feed entrance location is through direct entry to the RO stage inlet. As a result, the majority of permeate production (volume loss) is generated by the plant feed rather than the dilute outlet of the first CFRO stage, and the difference between the concentrating inlet and the diluting outlet of the first CFRO stage is reduced. As a result, we see a relatively well-balanced system in the BR-OARO configuration, as shown in figure

25a. Additionally, we observe that the optimal recycle stream flowrate (dilute inlet of the final CFRO stage in the BR configuration) is approximately equal to the plant feed flowrate.

For SF configuration, we observe that the difference between the diluting and concentrating side flowrates is greatest at the initial stages and diminishes at the final stages. This is because, as shown in figure 40c (in the appendix), the SF's optimum split feed ratio varies sage-wise, being higher at the beginning and lower at the end. Reduced feed split ratios result in a greater proportion of feed flowing to the diluting side as opposed to the concentrating side. In final stages with higher salinity and lower flux, a lower split feed ratio results in less salinity reduction on the dilute side. This increases the separation driving force and alleviates the low flux of the final stages. However, in the initial stages, the split feed ratio is decreased to maximize the salinity reduction of the dilute stream that enters the RO stage.

The flowrates of the diluting stream inlet and concentrating stream outlet (and vice versa) of each stage are so close in the CL configuration that they almost overlap. It is worth noting that the maximum flowrate of both the diluting and concentrating streams is approximately the same as the plant feed flowrate throughout the length of CL's stages.

a)

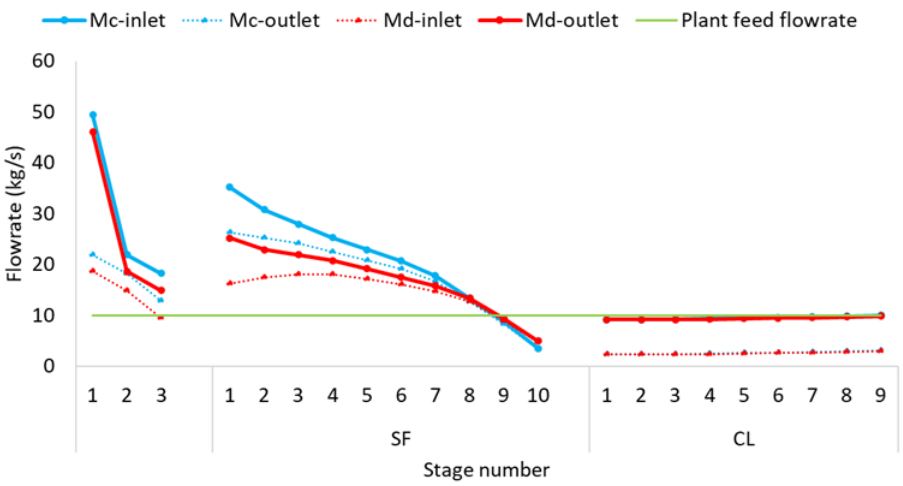
Mc-inlet
Mc-outlet
Md-inlet
Md-outlet
Plant feed flowrate
Flowrate (kg/s)
60
50
40
30
20
10
0
1 2 3
1 2 3 4 5 6 7 8 9 10
1 2 3 4 5 6 7 8 9
SF
CL
Stage number

b)

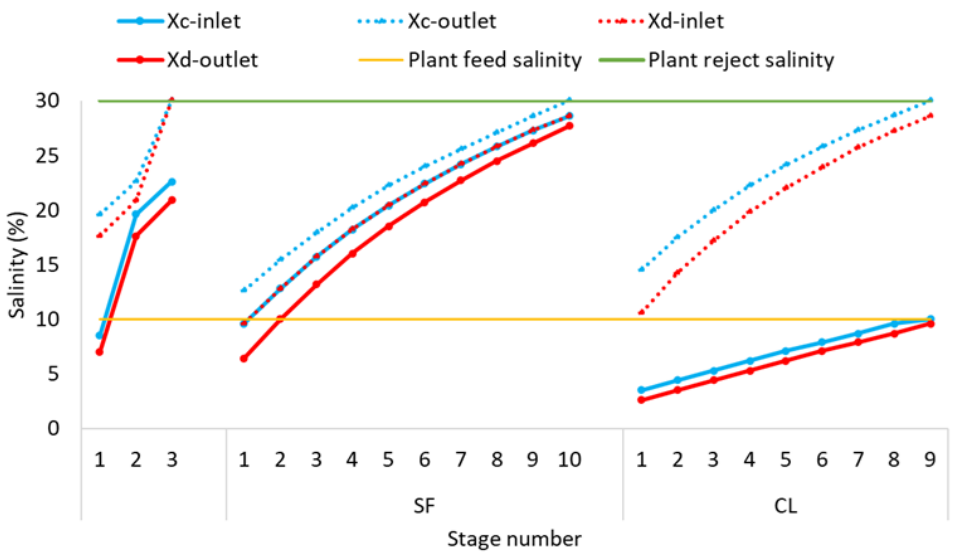
Xc-inlet
Xc-outlet
Xd-inlet
Xd-outlet
Plant feed salinity
Plant reject salinity
Salinity (%)
30
25
20
15
10
5
0
1 2 3
1 2 3 4 5 6 7 8 9 10
SF
1 2 3 4 5 6 7 8 9
CL
Stage number

c)

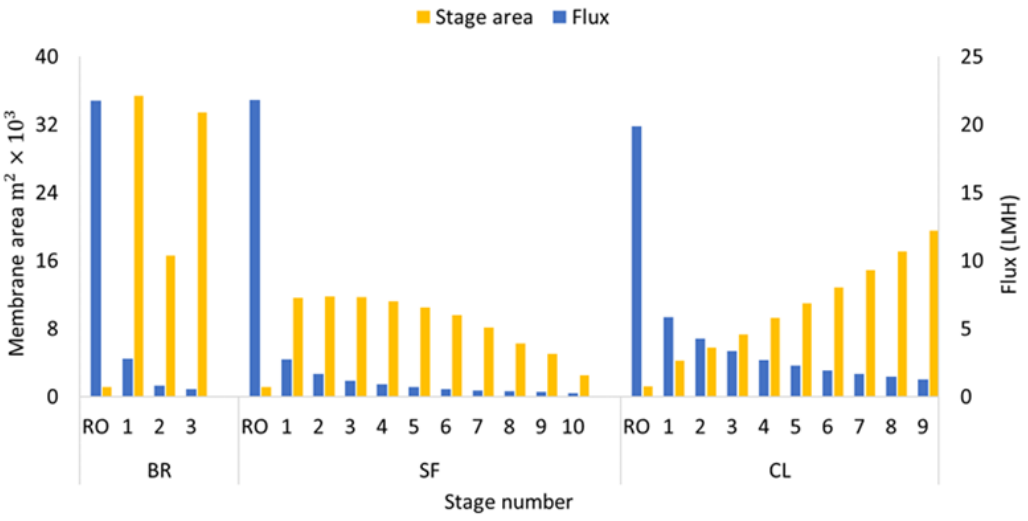
Stage area
Flux
Membrane area m² × 10³
40
32
24
16
8
0
Flux (LMH)
25
20
15
10
5
0
RO 1 2 3
RO 1 2 3 4 5 6 7 8 9 10
RO 1 2 3 4 5 6 7 8 9
BR
SF
CL
Stage number

d)

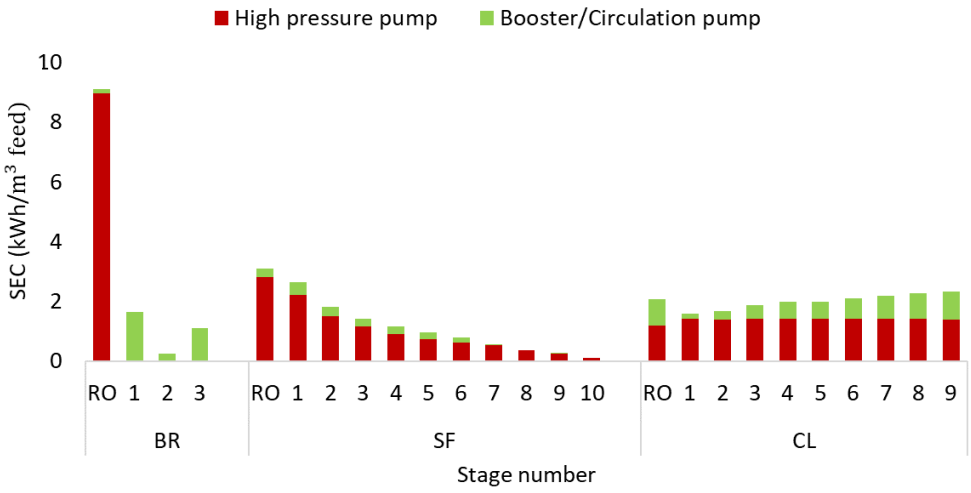

Figure 25. a) Stage flowrate and b) stage salinity, c) stage area, and d) stage specific energy consumption for BR, SF, and CL configurations at their cost optimum number of stages

Stage area and flux. Figure 25c shows the area and flux of each stage for all studied CFRO configurations operating at their minimum cost number of stages. Flux decreases stage-wise for all three configurations, with significantly higher flux occurring at the initial RO stage. This is due to the fact that, as illustrated in Figure 25b, the salinity of both dilute and concentrating solutions increases stagewise in all configurations. According to our findings, higher salinity levels have higher concentration polarization, resulting in lower flux in the final stages. The initial RO stage not only benefits from the lower salinity of the feed, but it also operates at a higher hydraulic pressure, resulting in a higher flux and smaller area than the subsequent CFRO stages. In comparison to SF and BR's CFRO stages, CFRO stages in CL configurations operate at a higher flux. This is because the CFRO stages of the SF and BR configurations operate at higher salinities

than the CL configuration in which the last CFRO stage's concentrating inlet and diluting outlet salinity are bound by the plant feed salinity (figure 25b).

CL stage area increases stage by stage as permeate production remains constant while flux decreases. In the SF configuration, permeate production decreases stage-wise, resulting in stage-wise area reduction despite the decrease in flux. However, for BR, the initial and final CFRO stages have the largest area. This is because BR stages are connected in series, similar to a long stage, and are separated whenever the width of the stage needs to be changed in accordance with the pressure drop and Reynolds number, as described in the preceding section. As a result, there is no regular pattern for the stage area of the BR configuration.

***Stage specific energy consumption*.** Our findings indicate that, with the exception of the RO stage in the CL configuration, all stages operate at their maximum allowable pressure in all configurations (figure 40b in the appendix). This demonstrates that configuring multiple stages of CFRO modules in series (for example, COMRO and BR-OARO) does not save energy in the same way that a multi-stage RO (MSRO) system does (i.e., stagewise increase in applied pressure). This is because the large CFRO membranes have a significant impact on CFRO optimum design; Lower pressure reduces flux and increases the membrane area of these systems, resulting in an increase in pressure drop and membrane cost. As a result, the energy savings in multiple stages of CFRO module is series only occur with regard to changing the width and adjusting the Re of the system, as previously explained.

The applied pressure in CL's RO stage is low at the module's inlet (around 50 bar) and gradually increases to the maximum allowable level of 85 bar at the RO stage's concentrate outlet. This saves energy by operating at a lower pressure and higher flowrate at the beginning of the RO stage and a higher pressure and lower flowrate toward the RO stage’s outlet. However, for BR and

SF configurations, the high osmotic pressure of the RO feed inlet at high salinity prohibits the RO stage from operating at a low initial hydraulic pressure. Thus, the RO stage of the SF and BR modules operates at a maximum hydraulic applied pressure of 85 bar throughout the module's length.

Figure 25d depicts the stage specific electricity consumption (SEC) of the investigated configurations, as well as the portions of SEC attributed to the operation of the high-pressure pump and booster/recirculation pumps. For BR configuration, the majority of SEC occurs in the initial RO stage and is primarily made up of high-pressure pump SEC. This is because the feed to each BR's CFRO stage is already pressurized effluent from the preceding stage, requiring only booster and recirculation pumps to maintain the optimal flow and separation process. Our optimization results indicate that the stream from the RO outlet is only partially depressurized in the ERD device (to pressurize RO inlet stream). As a result, the RO outlet stream exits the ERD while maintaining an elevated pressure. Additionally, this stream recovers energy from the system's reject brine prior to entering the first CFRO stage via another ERD device. As a result, the concentrating stream enters the train of CFRO stages without the need for an additional high-pressure pump. First and last stages of the BR configuration have the highest stage SEC of recirculation/booster pumps, which is a function of the stage area and flow rate.

For SF, the SEC of both the high-pressure pump and the recirculation/booster pump gradually decreases stage-by-stage proportional to the flow, and area of each stage. Although the concentrating effluent from each stage of the SF configuration flows to the next, unlike the BR configuration, each stage of the SF configuration requires a high-pressure pump to pressurize the streams. This is due to the fact that the majority of the feed stream to each SF stage comes from the subsequent stage's low-pressure diluting stream outlet, which requires pressurization. Further,

the effluent from the previous stage is split between the diluting and concentrating channels, with only a portion of it going to the concentrating side. Our findings show that for optimal performance of SF configuration, each stage's effluent must be completely depressurized before proceeding to the next stage, and its reject energy is recovered for the concentrating stream at the same stage's inlet.

For the CL configuration, all stages SEC of the high-pressure pump are roughly the same because they operate at the same flowrate and the effluent of each stage is completely depressurized because it should serve as the dilute of the next stage. As a result, pressurization is required at each stage, and ERD devices recover energy from the reject stream for the same stage's inlet concentrating stream. The energy required for recirculation in CL increases stage by stage as the stage area and pressure drop increase.

4.3.1 Sensitivity Analysis

Feed salinity. Figure 26a shows the treatment cost of the studied CFRO configuration for two levels of feed salinity, 3.5% and 10%. The treatment costs of both SF and BR are reduced by 55% when the feed salinity is reduced from 10% to 3.5%, while the treatment costs of CL are only reduced by 16%. This is primarily because, in the case of SF and BR, lowering the feed salinity results in the majority of the separation occurring in the initial RO stage. As a result, the volume of the RO effluent, which is the amount of stream that requires further concentration in the subsequent CFRO stages, decreases, as does the amount of CFRO permeate recirculation to the RO stage. However, in the case of CL, plant feed enters the final CFRO stage via a separate loop, and permeate production is constant throughout the stages. As a result, salinity reduction has no effect on the flowrate of the CFRO stages. The only reason for the slight reduction in CFRO

treatment costs associated with reduced salinity is that the average salinity of all stages is reduced, which increases flux and reduces area requirements. This is consistent with the result obtained in analytical study by [35], which demonstrated that the energy consumption of the CL configuration is not dependent on the feed salinity but rather on the brine salinity. As a result, the operational difference between SF and BR with CL is even more pronounced at lower salinities.

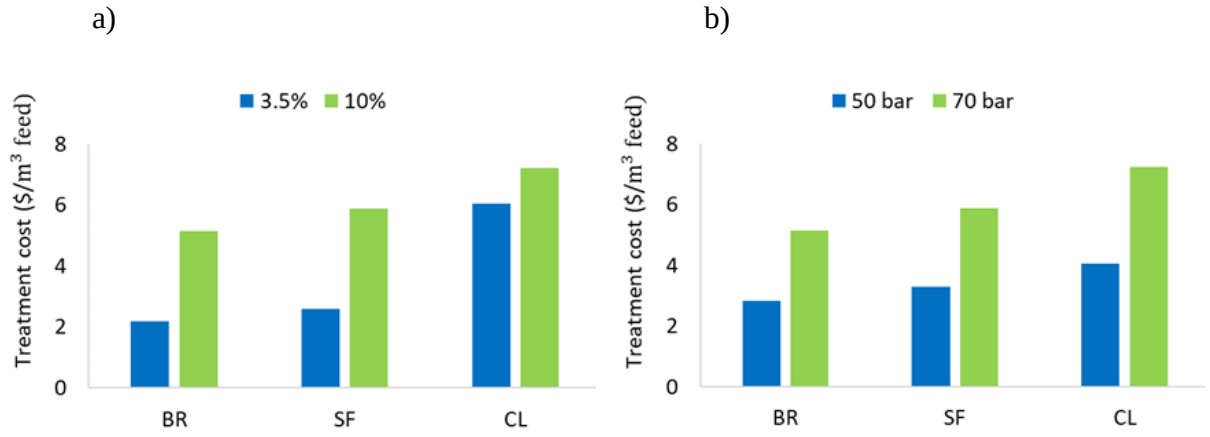

Figure 26. Cost of treatment for BR, SF, and CL configurations for: a) two stage salinity levels of 3.5% and 10%, and b) two burst pressure levels of 50 and 70 bar for CFRO membranes.

Pressure- The effect of increasing the burst pressure of CFRO membranes on treatment cost is shown in Figure 26b. Increased pressure has roughly the same effect on all configurations in terms of relative cost savings. Increasing the burst pressure from 50 to 70 bar results in a 44% reduction in the cost of treatment for all configurations. This is because increased pressure results in a greater driving force for separation, which increases flux and decreases the membrane area, resulting in a decrease in pressure drop and a reduction in capital and energy costs.

4.4 Conclusion

We presented the BR-OARO configuration and developed optimization models for the BR-OARO, as well as frequently discussed CL-OARO, SF-CFRO, and COMRO configurations. We optimized each system to maximize recovery and to minimize treatment costs and compared their capital, operating, and energy consumption costs, as well as membrane area. We performed analysis on a hypothetical plant treating hypersaline produced water with salinities ranging from 10% to 30% and the following are the manuscript's main findings:

- Regardless of the number of stages used, COMRO cannot achieve the high recoveries required for the ZLD condition at the burst pressures of 50 bar used in this study. CL and SF configurations necessitate a large number of stages in order to achieve high recoveries. However, the single stage BR configuration can achieve ZLD recovery with a maximum applied pressure as low as 20 bar.
- Recovery limitation in SF and CL configurations with a low stage count is primarily due to their limited dilute stream inlet salinity (not the salinity treatable by RO stage). Dilute salinity can be reduced to a level treatable by RO stage in one single stage, such as one in the BR configuration.
- In terms of cost, membrane area, specific energy consumption, and stage count, BR outperforms all other configurations. We observe that the performance of the SF configuration approaches that of the BR configuration when the number of stages is increased, but at the cost of increased design complexity.
- Increasing the number of stages saves energy and thus lowers the cost of BR configuration, but only by a modest 10%. Increasing the number of stages in SF, on the other hand, results in a 50% reduction in treatment cost, owing to the reduction in membrane area. The cost

of the CL configuration is reduced by adding only one stage in addition to the minimum number of stages required to achieve the desired recovery, owing to the savings in membrane area, as with the SF configuration.

- Configuring CFRO stages in series results in energy savings in BR and SF. This enables the width to be adjusted in accordance with the lower Re bound.
- Because of the large pressure drop at CFRO stages with large areas, all configurations operate at low Re numbers. Furthermore, increasing Re necessitates more staging in order to adjust the width and alleviate pressure drop.
- With the exception of the RO stage in the CL configuration, all stages in all configurations operate at their maximum allowable hydraulic pressure. As a result, configuring CFRO modules in series does not save energy in the same way that MSRO systems do.
- The initial RO stage has the highest SEC of the BR configuration, with high pressure pump SEC being the main constituent, and the remaining stages only require a booster/recirculation pump. In the case of SF, the SEC of the high-pressure pump and the booster/recirculation pump is distributed proportionally to the area and flowrate of the stages and increases stage-wise. The SEC of the CL high pressure pump is the same at all stages, while the SEC of the recirculation/booster pump increases stage by stage.
- Reducing plant feed salinity significantly lowers the treatment cost of BR and SF configurations while only slightly lowering the cost of CL configurations. Our findings show that a 65% reduction in feed salinity (10% to 3.5%) lowers SF and BR treatment costs by 56% while only lowering CL costs by 16%.
- Increased membrane burst pressure reduces the cost of BR, CL, and SF configurations, and the effect of increased pressure is consistent across all of these configurations. Our findings

indicate that a 40% (50 to 70 bar) increase in CFRO membrane burst pressure results in a 44% reduction in treatment cost of all configurations.

5.0 Optimization Based Comparison of Single Effect versus Multi Effect Mechanical Vapor Recompression for Shale Oil and Gas Produced Water Treatment

With the growth of unconventional oil and gas extraction, the need for environmental management and desalination of hydraulic fracturing produced water is increasing. Mechanical vapor recompression (MVR) is one of the evaporative technologies that fits this purpose due to its ability to operate at high TDS (Total Dissolved Solids), high recovery ratio, high energy recovery, and modular design. MVR consumes a significant amount of electricity and has a relatively high capital cost due to the equipment (including compressor, evaporator, preheaters) required to work with highly saline water. Thus, optimization of the MVR's operating conditions and equipment size is required to develop a financially viable system and to conduct technical assessments on its application in produced water treatment. Additionally, MVR has a variety of configurations including single effect and forward feed, backward feed and parallel feed multi effects. Increasing the number of effects decreases the vapor flow to the compressor, which reduces energy consumption. On the other hand, increasing number of effects increases the required temperature differential across the compressor, which increases energy consumption. The net effect of increasing the number of effects on MVR performance has yet to be investigated. The goal of this research is to compare the energy consumption and treatment costs of single effect and multi effect MVR systems within an optimization framework. Furthermore, we evalutate the effect of brine recirculation on MVR performance. In terms of produced water treatment costs, we conclude that

single effect MVR outperforms all other multi-effect configurations. Additionally, we find that incorporating a brine recycle stream raises both operating and capital costs.

5.1 Introduction

Mechanical vapor recompression (MVR) is an evaporative desalination technology able to treat hypersaline produced water owing to its low operating temperature preventing scaling and corrosion [123, 124]. MVR is one of the commercially available evaporative technologies with modular design that does not require external heating and cooling sources, since the system works based on the latent heat energy recovery. MVR system may be operated in single effect (SE-MVR) or multi-effect (MEE-MVR) operation modes [125, 126].

In conventional multi-effect evaporation (MEE) systems utilizing steam as external energy source, increasing the temperature difference between the heating steam and the end condenser will yield higher energy recovery and higher GOR. This is achieved by enabling the system to work with higher number of effects with higher temperature difference across the evaporator and condenser. However, for the case of MVR, the latent heat recovery process is mainly induced by vapor compression and the compressor is the main energy consumer in the system. This implies the fact that the potential benefit of increasing number of effects in MEE-MVR systems might be different from conventional MEE systems. While there is significant work regarding conventional MEE systems [127-134], there are a limited number of studies analyzing the MEE-MVR [135-140]; Most of these studies lack analyzing the system with varying and optimum compressor head assuming temperature difference at the inlet and outlet of the compressor as a constant. Further, unlike rising film evaporator tubes horizontal tube falling film evaporators do not require high

temperature difference as driving force and could work with temperature differences as low as 1-2 ℃. To have a fair comparison between single effect and multi-effect MVR systems, lower temperature difference ranges and also optimum temperature differences for each specific number of effects should be considered.

Evaporator and compressor are the main elements affecting the cost of MVR systems. To reduce the cost of evaporators, the temperature difference across the evaporator tubes should be increased which reduces the required evaporator area for heat transfer [141]. This in turn increases the work required by compressor. To decrease the compressor cost, either the compressor head or the vapor mass flowrate to the compressor should be decreased. The former is achieved by increasing the evaporator area and the latter could be realized by increasing the number of effects, both of which increase the evaporator cost [142]. This implies that there is a tradeoff between operating and capital cost of the system and indicates the necessity for finding this optimum.

5.2 Methodology

MVR configuration and process description- In this section, the overall process scheme will be first depicted for a single effect MVR and then various configuration of multi-effect MVR will be explained.

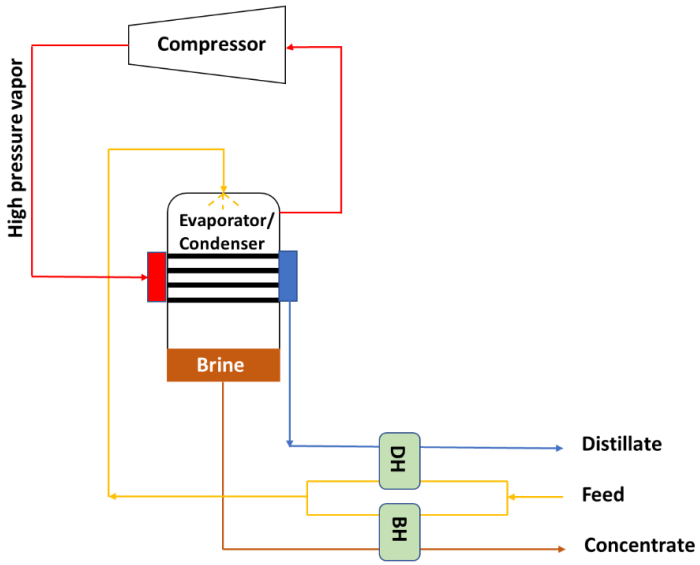

Figure 27. Single effect MVR

Single effect MVR- The MVR system, shown in figure 27 consists of two plate preheaters, a horizontal tube falling film evaporator/condenser, compressor, pumps, and mixers. Saline feed entering the system recovers the sensible heat, via two preheaters, from hot brine and hot distillate streams leaving the system. The preheated feed is then sprayed over the evaporator horizontal tubes surfaces forming even thin film layers. Falling film is then partially evaporated at relatively low pressure and temperature, induced by compressor vacuum system, and the remaining concentrated blowdown leaves from bottom of the evaporator. The generated vapor is introduced to compressor and its pressure and temperature is increased to provide the driving force (temperature difference) of the heat transfer between the saline film layers and water vapor. Superheated vapor exiting the compressor enters the evaporator tubes and condenses by losing its heat to the saline film layers over the horizontal tubes.

Multiple effect MVR- In this mode of operation, MVR system is designed with multiple evaporator/ effects in series; Compressed vapor condenses inside the first effect evaporator tubes producing distillate, while vapor is generated over the tubes at a lower temperature which is then

introduced to the second effect. Vapor generated from each effect enters the subsequent effect tubes as heating source and this process continues. As a result, MVR effects operate at successively lower pressure and temperature from first effect to the last one. The generated vapor from the last effect enters the compressor inlet. The heating vapor in the first effect undergoes desuperheating process via sensible heat transfer prior to condensation, while for the rest of the effects vapor is saturated and condenses as it enters the evaporator tubes. There are various multiple effect MVR systems based on the feed flow arrangement as follows:

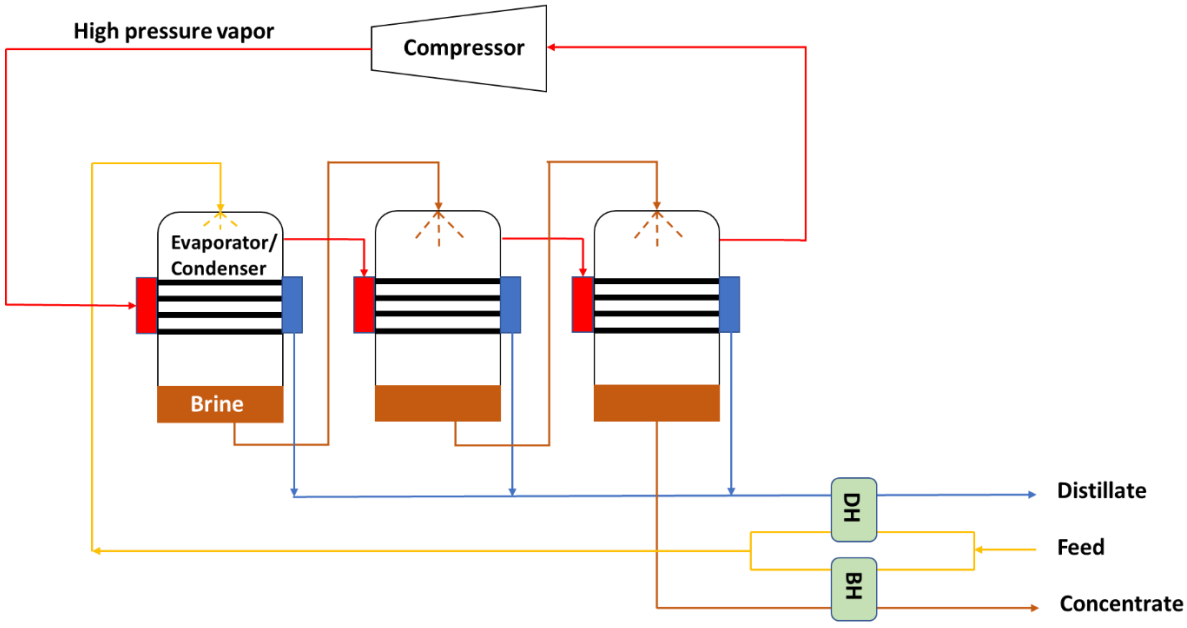

Figure 28. Forward feed multi effect MVR

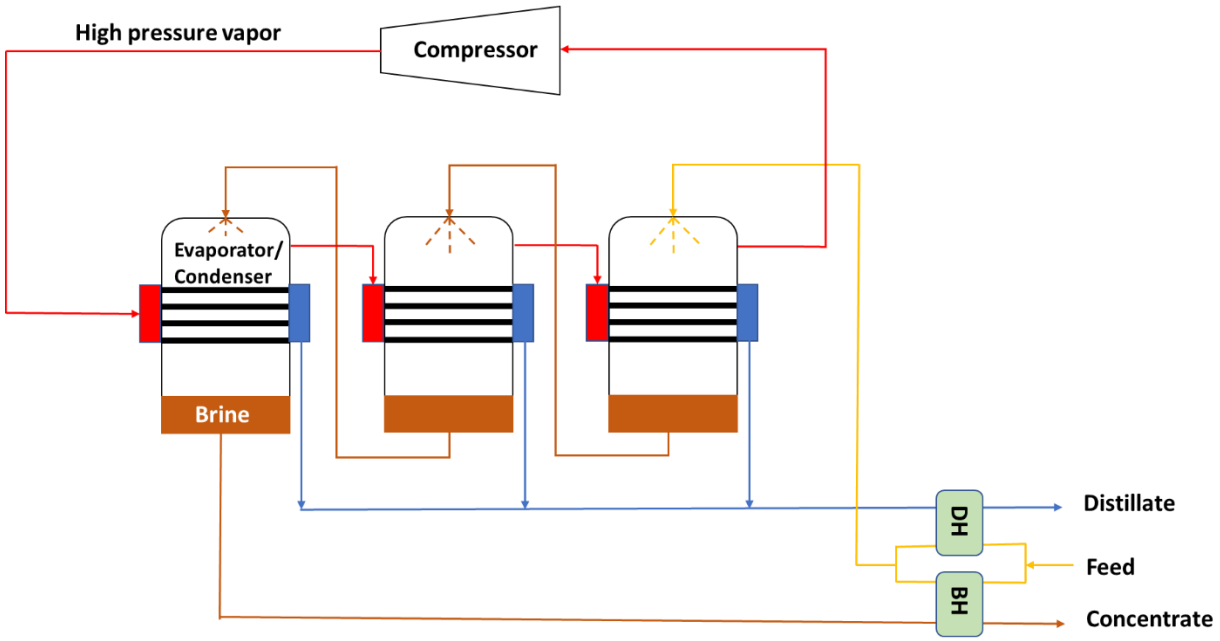

Figure 29. Backward feed multi effect MVR

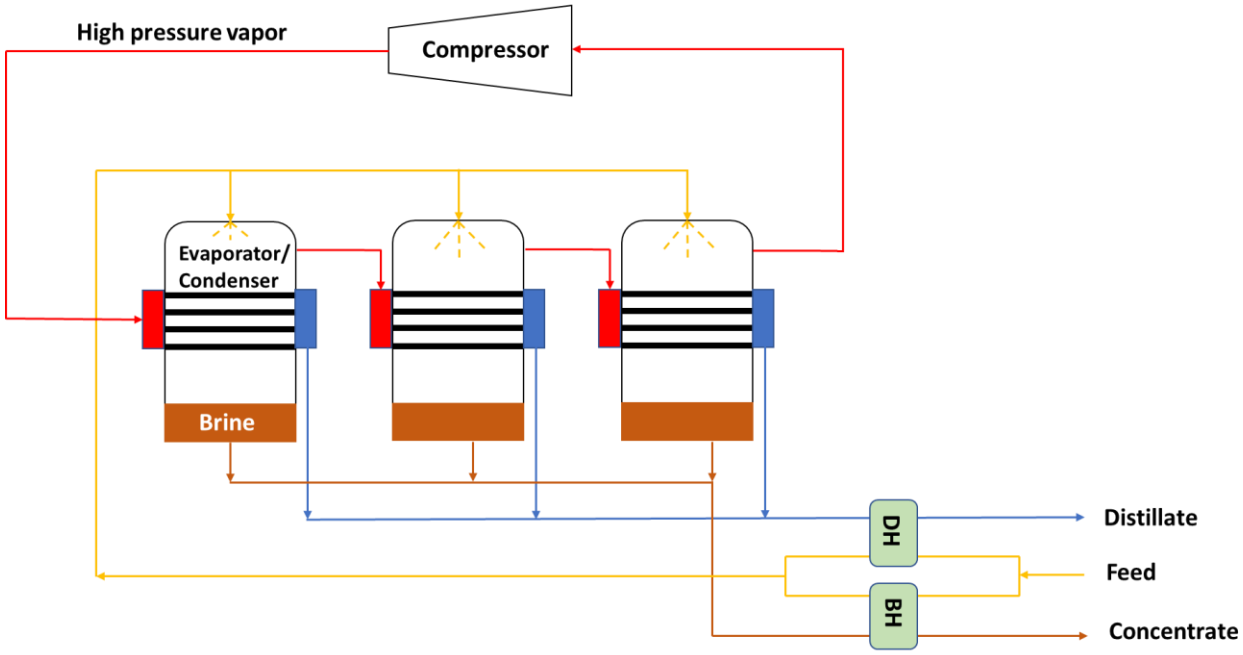

Figure 30. Parallel feed multi effect MVR

Forward feed (FF) multi effect MVR- In this configuration (figure 28), feed moves in the same direction with the heating vapor through the system; Preheated feed is sprayed over the first effect tubes and the concentrated brine is directed to the next effect. Concentrate brine from each effect act as the feed for the subsequent effect. The temperature of the feed in the first effect is initially increased via sensible heating prior to evaporation, while for the subsequent effects the entering brine is first partially flashed due to decreased pressure and temperature, and then the remaining saturated brine evaporates via latent heat recovery.

Backward feed (BF) multi effect MVR- In this configuration (figure 29), feed moves in the opposite direction with the heating vapor through the system; Preheated feed is sprayed over the last effect tubes and the concentrated brine is directed to the previous effect and this process continues. The temperature of the feed in all effects is initially increased via sensible heating prior to evaporation due to increasing temperature and pressure in the feed flow direction.

Parallel feed (PF) multi effect MVR- In this configuration (figure 30), preheated feed is distributed equally in all the evaporators. The temperature of the feed in all effects is initially increased via sensible heating prior to evaporation and the concentrated brine from each effect is directed to the subsequent effect blowdown space causing brine partial flashing due to decreased temperature and pressure.

5.2.1 Modeling MVR Process

Thermodynamic Model- MVR desalination process is modeled using a combination of mass and energy balance equations for preheaters, evaporators, and compressor. Preheaters are modeled considering stream temperature changes through sensible heating across the preheater plates. Evaporator are modeled depending on the operation mode and feed flow arrangement,

through vapor desuperheating and condensation, film layer sensible heating, latent heat flux across the evaporator tubes, and flashed vapors due to pressure drop. The compressor work is calculated assuming adiabatic compression. The equations used to model these processes are summarized in table 24 in the appendix.

Economic Model- To calculate the cost of the system, representative correlation for capital costs (including preheaters, evaporators, compressor, and pumps), and for operating costs (including electrical energy required to operate compressor and pumps) were gathered from available textbooks and literature [143-145].

Objective function and constraints – Similar to MD system, the objective function is defined to minimize the unit cost of produced water treatment with main constraint being the concentrate salinity at ZLD requirement, and other logical constraints regarding temperature changes within the system.

Optimization - The model described above is optimized through a non-linear programming model coded in GAMS utilizing local solver CONOPT. To our knowledge, there is no optimization based comparative study that compares energy usage, and capital cost of single effect and multi-effect MVR with various feed flow arrangements treating compressor head itself as an optimization variable for application in zero liquid discharge for produced water management.

5.3 Results and Discussions

The developed optimization models are applied to a hypothetical plant with a capacity of 10 kg/s that concentrates produced water with a salinity of 10% to reject brine with a salinity of 30%.

Treatment cost and temperature difference across compressor- Figure 31 shows the treatment cost of single effect MVR and MEE-MVR for FF, BF, and PF configurations with varying number of effects each of which at their own optimum temperature differences (figure 32) across the compressor inlet and outlet; Interestingly, single effect MVR has the lowest unit treatment cost when compared with MEE-MVR configurations. This is because by increasing the number of effects, the compression ratio (corresponding to temperature difference across the compressor) is increased accordingly to prevent the high cost of evaporators with very large areas. Also, compression ratio is increased to provide higher degree of superheating to compensate for lower amount of heating vapor mass flowrate to the multi-effect system. This results in an increase in compressor energy consumption, as illustrated in figure 44b in the appendix. All three MEE-MVR configurations have very close economic performance with PF having the lowest cost, followed by BF and FF configurations. Feed flowrate distribution among PF effects cause this system to require both smaller evaporator areas, and smaller compression ratio to heat and evaporate the saline feed. The vapor production increases in successive effects for FF configuration, while it decreases for BF configuration. On the other hand, the concentration and thus boiling point elevation of the feed is higher in BF first effect in comparison to FF first effect. The combination of the mentioned factors causes BF to have lower total cost along with higher compression ratio in comparison to FF configuration. Figures 44a-c in the appendix provide

detailed information on compressor work, operating and capital costs, and evaporator area for various MVR configurations with varying numbers of effects.

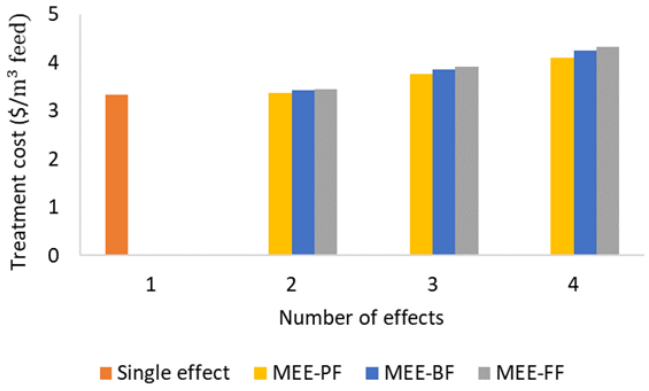

Figure 31. Treatment cost versus number of effects for MEE-MVR with various feed flow arrangement

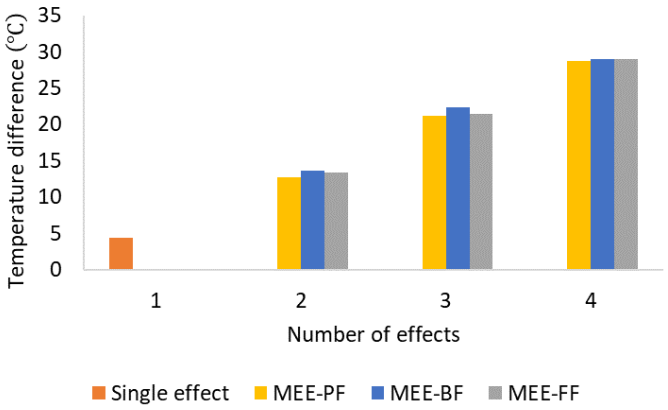

Figure 32. Temperature difference across the compressor versus number of effects for SE-MVR and MEE-MVR

To further investigate the importance of optimizing the temperature difference along with other variables, we optimized the models for a second round for single effect MVR and PF-MEE-MVR up to four effects assuming constant temperature differences shown in figure 33. By increasing the temperature difference across the compressor, the optimum number of effects- yielding lowest treatment cost- increases. It could be observed that as a certain number of effects is not matched with its optimum temperature difference, the treatment cost is highly increased.

This is because for higher number of effects, the lower the temperature difference, the higher evaporator area is required, although there would be some cost saving for the compressor and energy consumption. For lower number of effects and higher temperature difference, the evaporator capital cost decreases while the compressor cost and associated energy consumption is higher. To summarize, for small capacity and mobile applications such as shale gas plays, a single effect evaporator is the best choice with the lowest treatment cost, provided the compressor head is chosen appropriately.

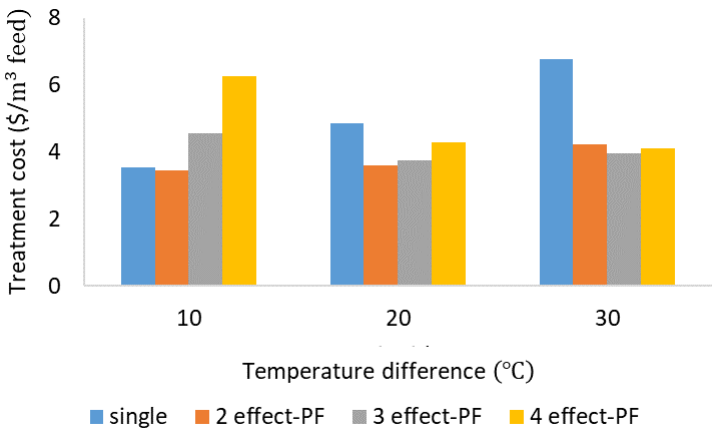

Figure 33. treatment cost versus temperature difference across the compressor for SE-MVR and PF-MEE-MVR up to four effects

Single effect MVR- Brine recycle- MVR has a high single pass recovery rate, with the ability to recover 67 percent water (corresponding to treating feed with 10% salinity to brine at 30% saturation salinity) without the need for brine recirculation. However, in order to avoid scaling and fouling, single pass recovery is usually kept between 10% and 50% in practice, and for most contaminated feed, this number drops below 10%. As a result, brine recirculation is required to achieve high recoveries. To investigate the impact of brine recirculation on the system's

energy and cost, we repeated the optimization procedure for single effect MVR with various single pass recoveries.

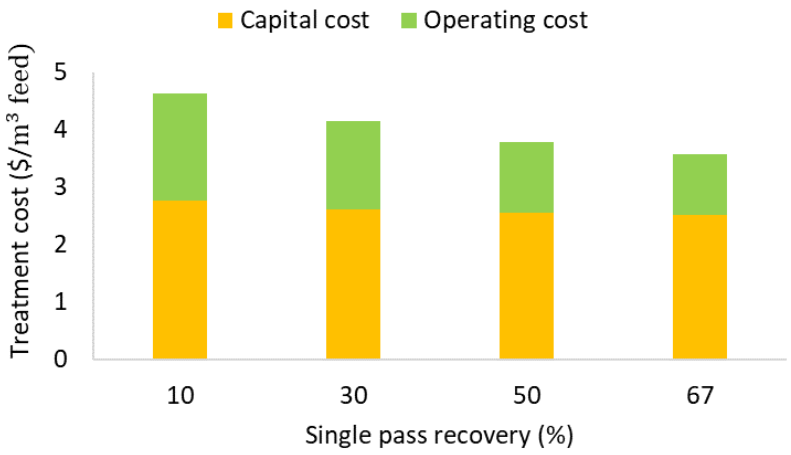

Figure 34. Single effect MVR treatment cost versus single pass recovery

Figure 34 depicts the treatment cost of single effect MVR at various single pass recovery values. The capital and operating costs decrease as the system's single pass recovery increases. This is primarily because recirculating brine has the same salinity as reject brine and thus increases the overall salinity in the evaporator area when combined with plant makeup feed. As a result, the vapor pressure at the compressor's inlet drops, and the compressor's work and size increase to maintain the driving force of separation across the evaporator tubes. When the compressor does not fully compensate for the temperature drop at the inlet, this will also slightly increase the evaporator area as the flow into the evaporator increases and the temperature across the evaporator tube decreases.

Feed salinity- Figure 35 depicts the variation in MVR treatment cost with and without recycle stream at two level of feed salinity. The MVR with brine recirculation corresponds to a single pass recovery of 30%. This number was chosen as an average number of single pass

recovery because there is no practical data available at this time. While lowering the feed salinity lowers the boiling point elevation in the evaporator area, it raises the operating cost in both cases of MVR with and without brine recycle. The primary reason for the increase in treatment costs is that increasing feed salinity while maintaining brine salinity constant at saturation salinity of 30% increases recovery and vapor production. As a result, the beneficial effect of reduced boiling point elevation is offset by an increase in vapor flow to the compressor, which increases energy consumption.

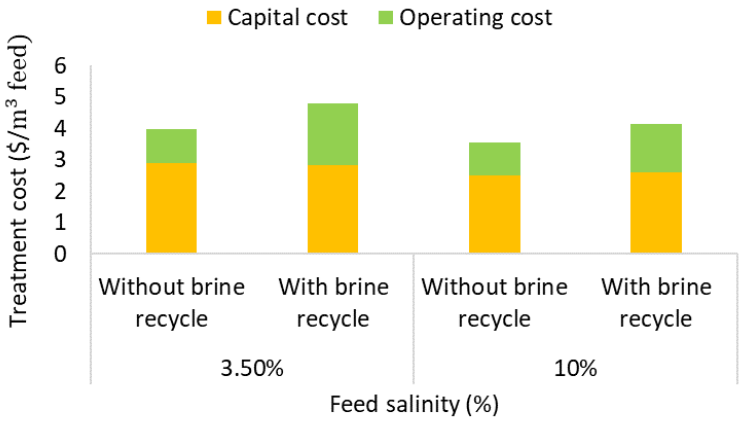

Figure 35. Treatment costs for MVR with and without brine recirculation for feed salinities of 3.5% and 10%. The brine recirculation configuration corresponds to a single pass recovery of 30%.

5.4 Conclusions

In this work, an optimization-based comparison of single effect versus multiple effect (including forward feed, backward feed, and parallel feed) mechanical vapor recompression is presented. The performance of the aforementioned configurations was examined twice, once with the saturation temperature difference across compressor as a free variable and once with it as a fixed parameter. It was concluded that when each configuration is allowed to operate at its optimal saturation temperature differential across the compressor, single effect MVR outperforms all other configurations. This is because as the number of effects increases, the temperature differential across the compressor increases proportionately to prevent the evaporators' surface area from increasing. However, when the saturation temperature differential across the compressor is fixed, the optimal configuration is determined by the magnitude of the temperature difference. It was discovered that when operating at a smaller saturation temperature difference across compressor, a lower number of effects yields the lowest treatment cost, and when operating at a larger saturation temperature difference across compressor, a higher number of effects yields the lowest treatment cost. Increasing the number of effects reduces vapor flow to the compressor, counteracting the negative effect of an increase in temperature difference across compressor. It was also discovered that the parallel feed configuration produces the lowest treatment cost among multi-effect configurations. The effect of brine recirculation on single effect MVR was also studied, and it was discovered that brine recirculation significantly increases MVR cost and energy consumption by increasing boiling point elevation, compressor work, and evaporator area. Sensitivity analysis of feed salinity revealed that an increase in feed salinity raises MVR treatment costs due to an increase in vapor flow to the compressor inlet.

6.0 Concluding Comparison Across Different Technologies, Summary, and Future Work

This chapter begins by summarizing the main findings of the previous chapters. Then, using the findings from the preceding chapters on MD, OARO, and MVR, it provides a comparison of treatment cost, equivalent work of separation, and equipment size across technologies. Finally, recommendations for future work are discussed.

6.1 Summary and Main Findings

The overall goal of this thesis was to assess the technoeconomic feasibility and performance of novel as well as well-established desalination technologies for hypersaline produced water treatment. Desalination technologies such as membrane distillation, mechanical vapor recompression, and osmotically assisted reverse osmosis were specifically investigated, as they are all capable of working with hypersaline brines, have a modular design, and have a high recovery rate. Various configurations of each technology were thoroughly analyzed using module-scale mathematical modeling of thermodynamic processes and technoeconomic nonlinear programming optimization. The following questions were addressed through an analysis of each technology: 1) how various configurations of each technology compare in terms of treatment cost, energy consumption, and equipment size when operating at their optimal design, 2) what factors contribute to the performance differences between various technologies and configurations, 3) how each technology's performance can be improved through configuration modification, and 4) how

the performance of various technologies compares to one another in terms of equivalent work of separation and treatment cost under various scenarios and conditions.

To ensure a consistent analysis and comparison of various technologies, all developed models were applied to a hypothetical water treatment plant with a capacity of 10 kg/s that concentrates produced water with a salinity of 10% to brine with a saturation salinity of 30% (corresponding to zero liquid discharge requirement). Sensitivity analysis was then conducted to determine the impact of input parameters on system performance.

Chapter 2 developed optimization-based analysis to evaluate the technical and economic performance of DCMD, AGMD, PGMD, CGMD, VMD, and SGMD configurations in single stage continuous recirculation mode for produced water treatment. Treatment costs and energy consumption were found to be significantly lower in AGMD than in other configurations, followed by CGMD, DCMD, VMD, SGMD and PGMD. Heating and cooling energy costs account for majority of the total treatment cost for all configurations. The energy consumption in MD configurations is directly linked to their thermal efficiency and heat recovery. It was demonstrated that incorporating an air gap or a vacuum channel into a membrane module, as in SGMD, VMD, and AGMD, yields the highest thermal efficiency, whereas incorporating a liquid gap, as in PGMD, has a detrimental impact on the system's thermal efficiency. The highest heat recovery was found in AGMD, CGMD, and DCMD, whereas the heat recovery of VMD is negligible due to the configuration's inherent heat recovery limitation. This research showed that when operating at a cost optimal design, AGMD produces the lowest flux with the largest membrane area, while VMD and DCMD produce the highest flux with the smallest membrane areas. Furthermore, it was revealed that SGMD and AGMD operate at low Reynolds numbers (Re less than 320) in their cost-

optimal design, whereas all other configurations have Re greater than 1,000. Increasing the Reynolds number in AGMD and SGMD results in a significant increase in their treatment cost.

All MD configurations were found to have a low single pass recovery (up to 6.5 percent for AGMD) and a high recycle ratio, which increases steam consumption through increase in vapor pressure lowering. The highest single pass recovery and lowest recycle ratio were observed in thermally efficient AGMD, SGMD, and VMD configurations. The sensitivity analysis of the MD hot channel inlet temperature revealed that, with the exception of VMD, lowering the MD inlet temperature increases the treatment cost in all configurations. Furthermore, it was demonstrated that for constant reject brine salinity, increasing feed salinity reduces treatment costs because of the decrease in recycle ratio; however, GOR of the system is independent of feed salinity at high recoveries. The operating salinity of MD is highly dependent on brine salinity at high recoveries and increasing reject brine salinity raises treatment costs due to a decrease in GOR and an increase in recycle ratio at constant feed salinity. Further investigation of the effect of gap size on AGMD and PGMD performance revealed that increasing the gap size decrease GOR while increasing membrane area and treatment costs. Given that PGMD can operate with smaller gap sizes, whereas AGMD requires larger gap sizes to avoid flooding, the difference in treatment costs between these two configurations is reduced when comparing AGMD with a larger gap size than PGMD. The analysis of the membrane thickness of DCMD, CGMD, and PGMD demonstrated that operating at their optimal thickness increases the GOR and area of the configurations, particularly PGMD, while decreasing the flux and treatment cost. Operation at extremely thick membranes may be prohibitively expensive due to the increased area requirement.

Chapter 3 present an optimization-based comparison of economic and energetic performance for gap type MD, DCMD, and VMD configurations operating in multi-stage

continuous recirculation mode. It was observed that the treatment cost and GOR of all MD configurations improve as the number of stages increase, with VMD and PGMD showing the greatest improvement. The AGMD configuration with the fewest stages was found to have the lowest treatment cost compared to all other configurations, whereas PGMD configuration with the highest number of stages has the highest treatment cost. It was demonstrated that AGMD benefits the most from increased thermal efficiency due to the reduced area when operating in multistage mode. VMD and PGMD, on the other hand, benefit the most from improved heat recovery in multistage operation mode.

Stagewise analysis of membrane area revealed that for DCMD and gap type MD, the water recovery ratio and stage membrane area are greatest in the early stages and decrease significantly in subsequent stages. However, for VMD, the water recovery ratio is constant throughout the stages, except for the final stage, which has the highest water recovery ratio. The stage area in VMD increases as the saturated vapor pressure across the stage decreases. This work demonstrated that except for AGMD, total membrane area increases as the number of stages increase, owing to an increase in specific area in DCMD, PGMD, and CGMD, as well as a higher number of stages with lower saturation pressure levels across the modules in VMD. However, for AGMD, increasing the number of stages reduces the total membrane area, lowering system costs. The heated stream ratio criterion was established to examine the trade-off between the total flowrate of the recycle streams in stages and the total flowrate of the makeup feed across stages when the number of stages was increased. It was discovered that the overall heated stream ratio decreases at first and then exhibits asymptotic behavior as the number of stages increase for all configurations.

Thickness analysis revealed that as the number of stages increase, a thinner membrane results in the lowest treatment cost with a smaller membrane area and higher flux. Additionally,

this work demonstrated that using optimally thicker membranes (than commercially available thin membrane) has a negligible effect on multistage CGMD and DCMD treatment costs, but significantly improves multistage PGMD treatment costs. The sensitivity analysis of feed salinity revealed that unlike the single stage continuous recirculation MD, the GOR increases across all configurations (excluding multistage VMD) while area increases. The trade-off between increased area and GOR results in a reduction in treatment costs for multistage DCMD, CGMD, and PGMD, but a slight increase in treatment costs for multistage AGMD. As with single stage configurations, the treatment cost of multistage VMD increases with feed salinity. Multistage MD configurations were also analyzed in the presence of a free source of chilling energy but at a higher temperature. The result revealed that the cost of treatment for all MD systems is significantly reduced. Additionally, it was discovered that when chilling costs are eliminated and the chilling source temperature is increased, the total membrane area for multistage DCMD, CGMD, PGMD, and AGMD decreases, whereas the membrane area for VMD increases as the vacuum pressure increases.

Chapter 4 proposes the BR-OARO configuration and evaluates it in comparison to the frequently discussed CL-OARO, SF-CFRO, and COMRO configurations through optimization-based analysis. Each configuration was evaluated in terms of maximum achievable recovery and lowest treatment costs. It was demonstrated that the limited recovery of single stage SF-CFRO and CL-OARO is due to their low diluting stream inlet salinity, and that a large number of stages is required to enable stagewise increase in diluting stream inlet salinity and recovery. COMRO was found to be incapable of achieving the high recoveries required for the ZLD condition regardless of the number of stages used. However, it was found that the single stage BR-OARO configuration is capable of yielding high recoveries with a maximum applied pressure as low as 20 bar. This

work further demonstrated that the BR-OARO configuration outperforms all other configurations in terms of cost, membrane area, specific energy consumption, and stage count. When the number of stages is increased, the performance of the SF-CFRO configuration approaches that of the BR configuration, but at the cost of increased design complexity. It was shown that increasing the number of stages slightly reduces energy consumption and thus the cost of the BR-OARO configuration. However, increasing the number of stages in SF-CFRO results in a significant reduction in treatment cost due to the reduced membrane area. The cost of the CL configuration is reduced by adding only one stage in addition to the minimum number of stages required to achieve the desired recovery, owing to the membrane area savings. This research established that connecting CFRO modules in series does not save energy in the same way that multistage RO systems do, as all CFRO stages operate at their maximum allowable hydraulic pressure in all configurations. Instead, connecting CFRO stages in series saves energy in BR-OARO and SF-CFRO by allowing the stage width to be adjusted to the lower Reynold's number bound. Additionally, it was demonstrated that the initial RO stage has the highest SEC of the BR-OARO configuration, with the high pressure pump consuming the most energy, while the remaining stages require only a booster/recirculation pump. In the case of SF-CFRO, the SEC of the high-pressure pump and booster/recirculation pump is proportional to the stage area and flowrate and increases stagewise. The SEC of the CL-OARO high pressure pump remains constant across all stages, whereas the recirculation/booster pump's SEC increases with each stage. The modeling results also showed that lowering the salinity of the plant feed significantly reduces the treatment cost of BR-OARO and SF-CFRO configurations, but only slightly reduces the cost of CL-OARO configurations. Finally, it was demonstrated that increasing the burst pressure of the membrane

reduces the cost of BR-OARO, CL-OARO, and SF-CFRO configurations, and that this effect is consistent across all configurations.

In Chapter 5, an optimization-based comparison of single effect versus multiple effect (including forward feed, backward feed, and parallel feed) mechanical vapor recompression is presented. The performance of all MVR configurations was examined twice, once with the saturation temperature difference across compressor as a free variable and once with it as a fixed parameter. It was concluded that when each configuration is allowed to operate at its optimal saturation temperature differential across the compressor, single effect MVR outperforms all other configurations. However, when the saturation temperature differential across the compressor is fixed, the optimal configuration is determined by the magnitude of the temperature difference. It was discovered that when operating at a smaller saturation temperature difference across compressor, a lower number of effects yield the lowest treatment cost, and when operating at a larger saturation temperature difference across compressor, a higher number of effects yield the lowest treatment cost. It was also discovered that the parallel feed configuration produces the lowest treatment cost among multi-effect configurations. The effect of brine recirculation on single effect MVR was also studied, and it was discovered that brine recirculation significantly increases MVR cost and energy consumption by increasing boiling point elevation, compressor work, and evaporator area. Sensitivity analysis of feed salinity revealed that an increase in feed salinity raises MVR treatment costs due to an increase in vapor flow to the compressor inlet.

6.2 Comparison Across Various Desalination Technologies

Multistage AGMD (labeled as MS-AGMD) and multistage VMD (labeled as MS-VMD) are selected as the two best MD technologies with the highest GOR and lowest treatment cost, and multistage DCMD (labeled as MS-DCMD) was chosen as the MD technology with the best performance guarantee. Additionally, these selected MD technologies are evaluated both with and without a free cooling source, as MVR and OARO do not require chilling. In the case of an abundant supply of feed water (e.g., seawater), or through integration with other industrial processes, a free cooling source may be available. The BR-OARO configuration is chosen as the best OARO configuration due to its low treatment cost, energy consumption, membrane area, and design simplicity in comparison to other OARO configurations. The BR-OARO is evaluated at two burst pressure levels: 50 bar as an optimistic but practical option (labeled as BR-OARO-50), and 70 bar (labeled as BR-OARO-70) as a membrane available with future membrane technology advancements. Because brine is commonly recirculated for operational purposes and adds to the treatment cost, single effect MVR (labeled as SE-MVR) with and without brine recirculation is chosen as the best ideal and best practical configurations of MVR, respectively. In the absence of industrial data, the SE-MVR with brine recirculation investigated in this section corresponds to the SE-MVR with an assumed average single pass recovery of 30%.

Figure 36a depicts the treatment cost of select desalination technologies with feed salinity of 10% and reject brine salinity of 30%. Assuming that OARO membranes with high burst pressure are available, BR-OARO-70 and multistage AGMD and VMD with a free available cooling source, result in the lowest treatment cost of $\$2.9/m^3_{feed}$. When a free cooling source for MD and a high-pressure membrane for OARO are unavailable, the next best options are multistage AGMD and SE-MVR without brine recirculation, at a cost of $\$3.57/m^3_{feed}$ per treatment. However, as

previously stated, SE-MVR may operate with brine recycle stream, and adding any portion of the recycle stream to SE-MVR degrades its performance in comparison to AGMD. On the other hand, it was demonstrated that AGMD requires a small air gap and a low Re number to function optimally, which comes with the risk of flooding and fouling. As a result, multistage VMD is the next best option, with a treatment cost of $\$3.8/m^3_{feed}$. VMD will perform optimally if full condensation occurs in the condenser; otherwise, the flow to the vacuum pump increases, increasing its energy consumption. SE-MVR with brine recirculation is the next best option, followed by multistage DCMD with free chilling, BR-OARO-50, and multistage DCMD with treatment cost of 4.1, 4.5, 5.1, and $\$5.4/m^3_{feed}$, respectively. Given the difficulties associated with operating BR-OARO crossflow membranes at low pressures of 50 bar, SE-MVR followed by DCMD would be more appealing options.

Figure 36b depicts the treatment cost of selected desalination technologies with feed salinity of 3.5% and reject brine salinity of 30%. When comparing technologies at lower feed salinity, BR-OARO-70 and even BR-OARO-50 have significantly lower costs than other technologies with 1.2 and $\$2/m^3_{feed}$ treatment cost, respectively. Chapter 4 demonstrated that the treatment cost of OARO systems decreases significantly with decrease in feed salinity. However, as demonstrated in Chapters 3 and 5, the treatment cost increases as feed salinity decreases for multistage AGMD, multistage VMD, and MVR, whereas the cost reduction is negligible for DCMD.

a)

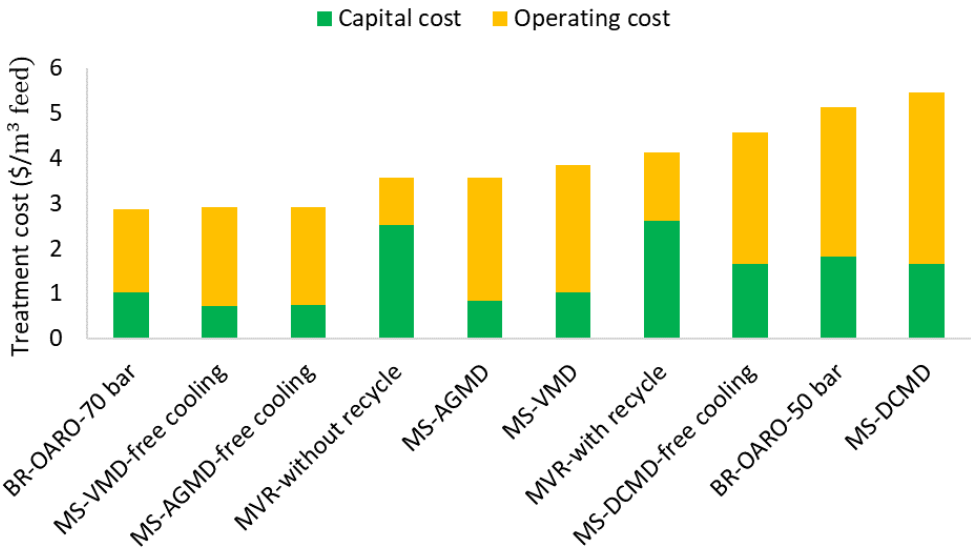

b)

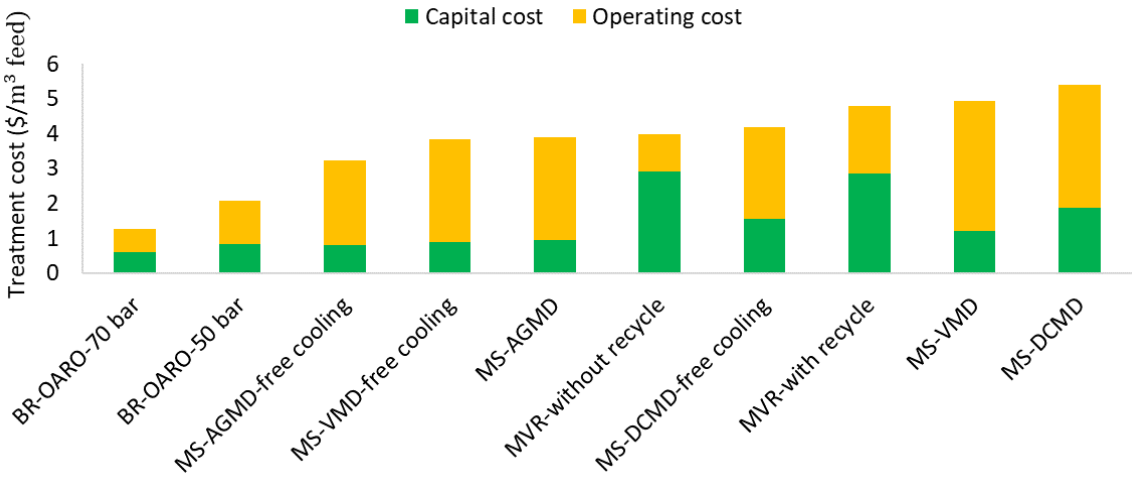

Figure 36. Unit cost of produced water treatment for a) feed with 10% salinity, and b) feed with 3.5% salinity, and reject brine with 30% salinity

In summary, given available technologies and ideal operating conditions, multistage AGMD followed by multistage VMD would result in the lowest treatment cost at high feed salinities. Additionally, MVR with brine recirculation followed by DCMD are the next best options due to the certainty of their predicted optimal performance. Specifically, multistage VMD and AGMD have the lowest capital cost in comparison to all other systems, which means that 1) they require a low initial investment and 2) if a free source of thermal energy is available, these options would yield significantly lower cost, followed by multistage DCMD. When operating at low feed salinities, pressure driven OARO systems are the best option, even at low burst pressure of 50 bar, as a great portion of the separation process happens in the initial RO stage. This implies the possibility of investigating RO coupled with MD rather than RO coupled with OARO. This is because the primary reason for OARO cost savings with reduced feed salinity is an increase in RO stage recovery, and the performance of multistage MD systems is superior to the BR-OARO-50 system at high salinity.

a)

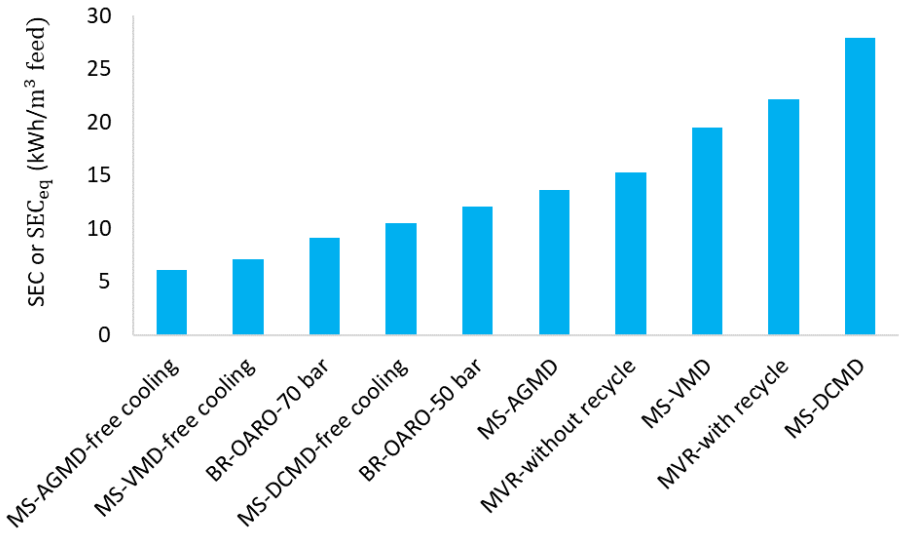

b)

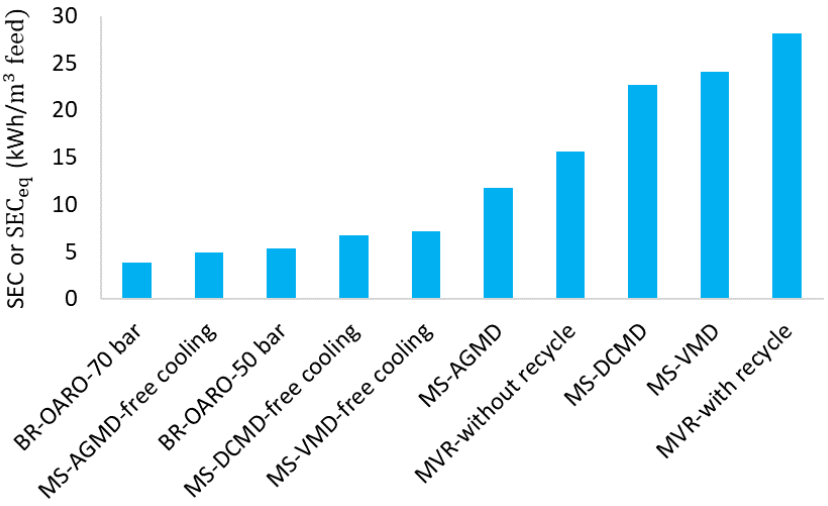

Figure 37. Work of separation for the OARO and MVR systems, as well as the equivalent work of separation for MD systems at their cost optimum design: a) feed salinity of 10%, and b) feed salinity of 3.5%.

6.3 Energy Consumption (Equivalent Work of Separation)

The equivalent work of separation for MD technologies with thermal energy sources was calculated to enable energy consumption comparisons with electricity-driven MVR and OARO systems; The steam used in thermal desalination processes such as MD is assumed to be extracted from a steam turbine, and the steam potential for electricity generation is calculated as equivalent work of separation. The method of calculation is detailed in appendix table 10. As illustrated in Figure 37a, when a free chilling source is available, multistage AGMD outperforms all other technologies with an SEC of 6.1 kWh/m^3_{feed}, followed by multistage VMD and BR-OARO-70 with SECs of 7.1 and 9 kWh/m^3_{feed}, respectively. The primary reason that a pressure driven membrane falls short of AGMD in terms of energy consumption, even at a high pressure of 70 bar, is the large pressure drop within BR-OARO systems with large areas. In an ideal case with no pressure drop within the OARO system, the separation work of the BR-OARO-70 will be reduced to 7 kWh/m^3_{feed}. To further reduce the energy consumption of the BR-OARO, the burst pressure of the membrane should be increased. When no free chilling is available, the BR-OARO-70 and BR-OARO-50 have the lowest work of separation. This indicates that when it comes to transitioning to low carbon zero liquid discharge and separation systems, pressure-driven separation processes are excellent potential investments. Considering the complexity of operating crossflow OARO systems with extremely low fluxes, the next best options are AGMD, followed by MVR without brine recirculation, VMD, MVR with brine recirculation, and DCMD. When operating at a low-salinity feed of 3.5% (figure 37b), BR-OARO-70, AGMD with free chilling, and BR-OARO-50 outperform all other technologies with 3.8, 4.9, and 5.3 kWh/m^3_{feed}, respectively.

a)

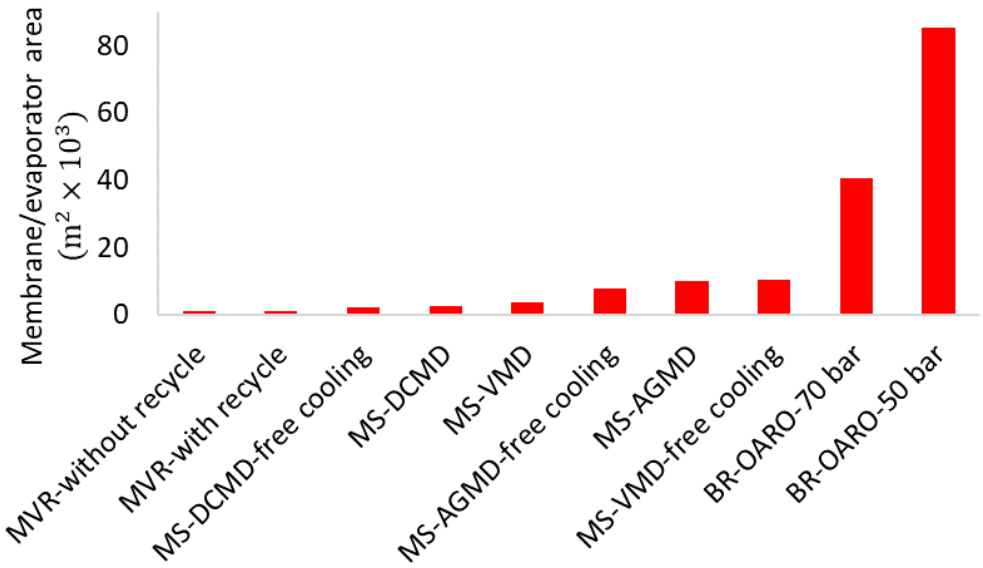

b)

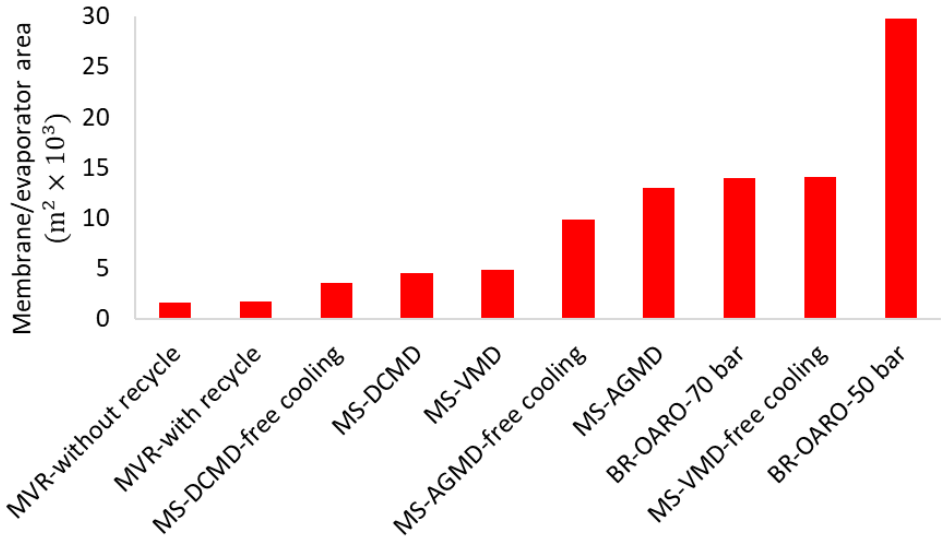

Figure 38. Cost-optimal equipment size (membrane for OARO and MD, and evaporator for MVR): a) feed salinity of 10%, and b) feed salinity of 3.5%

6.4 Equipment Size

Figure 38 a and b illustrate the total membrane area of the OARO and MD membranes, as well as the evaporator area of the MVR, at two different feed salinity levels of 10% and 3.5%, respectively. BR-OARO-50 and BR-OARO-70 have a significantly larger membrane area than MD systems at high feed salinity. However, by operating at a lower feed salinity of 3.5%, the required membrane area of BR-OARO systems improves significantly, approaching that of MS-AGMD in case of BR-OARO-70. The smallest equipment size belongs to the MVR evaporator area, followed by the MS-DCMD and MS-VMD. The dimensions of the equipment are provided for general comparison purposes only; however, the actual footprint of each technology may vary depending on the compactness of the equipment's design.

6.5 Future Work

It was demonstrated that the superiority of various desalination technologies varies according to the feed salinity. As a result, future research should focus on the potential of hybrid desalination technologies, such as OARO combined with MD, at a range of feed salinities. Furthermore, different technologies require a specific quality of energy source to function. For example, MD can be easily integrated with low temperature heat sources. As a result, it is advantageous to evaluate technologies on their ability to integrate a variety of energy sources, such as geothermal, solar, or waste heat from industrial processes such as flared gas. Produced water contains volatile organic compounds and various dissolved solids in addition to sodium chloride. Different technologies have different capabilities for removing all of these components. For

example, pressure-driven separation technologies, reject volatile compounds at a higher rate than thermal desalination technologies. As a result, it is suggested that these technologies be investigated for their performance when organic compounds are present in produced water and hence the need for pretreatment.

Appendix A . MD Plants Input Parameters and Cost Data

Table 2. Plant characteristics and annual cost estimation

Produced water temperature (°C)	20
Produced water salinity (%)	10
Reject brine salinity (%)	30
Plant capacity (kg/s)	10
Steam temperature	140
Maximum stream temperature (°C)	90
Minimum stream temperature (°C)	10
Maximum stream salinity (%)	30
Plant life (year)	20
Interest rate (5)	5

Table 3. Membrane properties- MD

Membrane type	PTFE with PP support	Ref
Membrane permeability coefficient* $\left(\frac{\text{kg}}{\text{s.m.Pa}}\right)$	0.936×10^{-10}	[69]
Membrane thermal conductivity $\left(\frac{\text{kW}}{\text{m.K}}\right)$	0.000242	[69]
Overall thickness of the membrane	148 μm	[69]
Active layer thickness (μm)	60	[69]
Membrane porosity (%)	60	[69]
Support thermal conductivity $\left(\frac{\text{kW}}{\text{m.K}}\right)$	0.00023	[69]
Air thermal conductivity $\left(\frac{\text{kW}}{\text{m.K}}\right)$	0.000024	
Conductive gap thermal conductivity $\left(\frac{\text{kW}}{\text{m.K}}\right)$	0.01	[51]
Permeate gap thermal conductivity $\left(\frac{\text{kW}}{\text{m.K}}\right)$	0.00006	[51]
Gap size (mm)	1	
Air gap spacer thermal conductivity $\left(\frac{\text{kW}}{\text{m.K}}\right)$	0.0002	[54]
Condensing surface thickness (mm)	1.5	
Cooling wall thermal conductivity $\left(\frac{\text{kW}}{\text{m.K}}\right)$	0.06	
Spacer porosity	77%	[69]
Spacer thickness	1.9 mm	[69]
Filament diameter	1.2 mm	[69]
Overall heat transfer coefficient (liquid-liquid heat exchangers)	$1.3\ \frac{\text{kW}}{\text{m}^2.\text{K}}$	Assumed
Overall heat transfer coefficient (liquid-condensing vapor heat exchangers)	$2\ \frac{\text{kW}}{\text{m}^2.\text{K}}$	Assumed

*calculated using the production of the active layer thickness and membrane permeability ($B_0 = B \times \delta_m$) obtained from ref [69].

Table 4.Capital cost data- MD

Capital Cost	Base price	Base capacity	Scale up coefficient	Ref.
Membrane (AGMD, PGMD, CGMD)	90 ($\frac{\$}{m^2}$)			[65]
Membrane (DCMD)	56 ($\frac{\$}{m^2}$)			[65]
Membrane Module (AGMD, PGMD, CGMD)	2340 ($\frac{\$}{module}$)	3 modules	0.8	[65]
Membrane module (DCMD)	1080 ($\frac{\$}{module}$)	3 modules	0.8	[65]
CGMD conductive material*	390 ($\frac{\$}{m^2}$)			assumed
Feed water storage Tanks	0.5 ($\frac{\$}{gal}$)			[66]
Permeate water storage Tanks	0.4 ($\frac{\$}{gal}$)			[66]
Heating and cooling installation each	5	10 ($\frac{m^3}{h}$)	0.6	[65]
Heat exchanger	390 ($\frac{\$}{m^2}$)			[65]
Heat exchanger endplate	950($\frac{\$}{module}$)			[65]
Chiller	200 ($\frac{\$}{kWh}$)			[68]
Pump	9052.35 $\left(\frac{\$}{unit}\right)$			[143]
Pump	271.57 $\left(\frac{\$}{liter/s}\right)$	1 $\left(\frac{liter}{s}\right)$	0.9	[143]
Blower	675.36	1 kW	0.5135	[146]

***** For CGMD membrane, the gap conductivity is increased by filling the gap with conductive material such as metal mesh, metal foam, or using finned condenser surface. [51]. We assumed the specially designed finned copper surface in reference [51] with thermal conductivity of 10 $\frac{W}{m.K}$ is used in CGMD. This process incure additional cost per square meter of membrane area to the system. Since this CGMD is developed in the lab scale we don't have any data about the amount and total cost of the material used to obtain thermal conductivity of in the gap. Therefore, for

the purpose of this study, we assumed the same price used for heat exchanger to be applicable to the conductive material filling per unit of area.

Table 5. Operating cost data- MD

Operating cost		Ref.
Steam	$0.008\ \left(\frac{\$}{\text{kg}}\right)$	[66]
Electricity	$0.069\left(\frac{\$}{\text{kwh}}\right)$	[66]
Membrane replacement	Every four years	Assumed
Pretreatment cost	$0.058\ \left(\frac{\$}{\text{kg feed}}\right)$	[65]

Appendix B . Single Stage MD

Our modeling closely follows the approaches described in references [51, 53, 72, 96, 147-149], as summarized in tables A.5. and A.6, followed by correlations in table A.7.

It is worth noting that we assume that only the active layer contributes to mass transfer, as demonstrated in [100], and that the support layer has a negative impact on heat transfer, as described in [101].

Table 6. Heat balance equations for single stage MD systems

Heat flux for $z \in Z$					
	DCMD	AGMD	PGMD/CGMD	SGMD	VMD
Convective heat -hot channel	$q^z_{conv_h} = h^z_h\left(T^z_{h_b} - T^z_{h_m}\right)$				
Convective heat -hot channel	$q^z_{conv_c} = h^z_h\left(T^z_{c_m} - T^z_{c_b}\right)$				-
Conductive heat-membrane	$q^z_{cond_m} = \frac{k_m}{\delta_m}\left(T^z_{h_m} - T^z_{c_m}\right)$	$q^z_{cond_m} = \frac{k_m}{\delta_m}\left(T^z_{h_m} - T^z_{g_m}\right)$		$q^z_{cond_m} = \frac{k_m}{\delta_m}\left(T^z_{h_m} - T^z_{a_m}\right)$	-
Conductive heat-gap	-	$q^z_{cond_g} = \frac{k_g}{\delta_g - \delta_{ff}}\left(T^z_{g_m} - T^z_{ff}\right)$	$q^z_{cond_g} = \frac{k_g}{\delta_g}\left(T^z_{g_m} - T^z_{cw}\right)$	-	-
Conductive heat-falling film		$q^z_{cond_{ff}} = \frac{k_w}{\delta_{ff}}\left(T^z_{ff} - T^z_{cw}\right)$			
Vapor expansion heat	-	-	-	-	$q^z_{exp} = RT^z_{h_m}\log\left(\frac{P_{h_m}}{P_{vac}}\right)$

Table 6 (continued)

Heat of evaporation/condensation	$q_e^z(T) = J^z H_e^z(T)$				
Heat of condensation in air channel	-				$q_c^z(T) = Jc^z H_e^z(T)$
Heat balances for $z \in Z$					
	DCMD	AGMD	PGMD/CGMD	SGMD	VMD
Heat balace1	$q_{conv_h}^z = q_{cond_m}^z + q_e^z(T_{h_m}^z) + C_p^z(T_{h_m}^z - T_{h_b}^z)$				$q_{conv_h}^z = q_{exp}^z + q_e^z(T_{h_m}^z) + C_p^z(T_{h_m}^z - T_{h_b}^z)$
Heat balance2	$q_{conv_c}^z = q_{cond_m}^z + q_e^z(T_{c_m}^z) + C_p^z(T_{c_m}^z - T_{c_b}^z)$	$q_{conv_c}^z = q_{cond_{ff}}^z + C_p^z(T_{ff}^z - T_{cp}^z)$	$q_{conv_c}^z = q_{cond_m}^z + q_e^z(T_{g_m}^z)$	$q_{conv_a}^z = q_{cond_m}^z + C_{pv}^z(T_{h_m}^z - T_{a_b}^z)$	-
Heat balance 3	-	$q_{cond_m}^z = q_{cond_g}^z$	$q_{cond_m}^z + q_e^z(T_{g_m}^z) = q_{cond_g}^z$	-	-
Heat balance 4		$q_{cond_{ff}}^z = \frac{k_w}{\delta_{ff}}(T_{ff}^z - T_{cp}^z)$			
Enthalpy balance for $z \in Z$					
	DCMD	AGMD	PGMD/CGMD	SGMD	VMD
Enthalpy balance-hot channel	$q_{conv_h}^z L^z W = M_{h_{in}}^z C_p^z(T_{h_{in}}^z - T_{h_{out}}^z)$				
Enthalpy balance-cold channel	$q_{conv_c}^z L^z W = M_{c_{in}}^z C_p^z(T_{c_{out}}^z - T_{c_{in}}^z)$			$q_{conv_c}^z L^z W + q_c^z(T_{a_b}^z) = (M_{a_{in}}^z C_{pa}^z + m_{v_{in}}^z C_{pv}^z) \times (T_{a_{out}}^z - T_{a_{in}}^z)$	-

Table 6 (continued)

Enthalpy balance-heater	$M_s h_{v_s} = (M_f + M_{rec}) C_p \left(T_{c_{hx_{out}}} - T^z_{h_{in}}\right)$, Z=1				$M_s h_{v_s} = (M_f + M_{rec}) C_p (T_{mix} - T^z_{h_{in}})$, Z=1
Enthalpy balance-external heat exchanger/ condenser	$(M_f + M_{rec}) C_p \left(T_{c_{hx_{out}}} - T_{mix}\right) = M^z_{c_{in}} C_p \left(T_{h_{hx_{in}}} - T$ $z = lastz$	-	-	$(M_f + M_{rec}) C_p \left(T_{c_{hx_{out}}} - T_{mix}\right) = M^z_{a_{in}} (T^{firstz}_{a_{out}} - T^{lastz}_{a_{in}}) + M_{p_{tot}} h_v (T_{sat})$	$(M_f + M_{coolant}) C_p \left(T_{c_{hx_{out}}} - T_{mix}\right) = M_{p_{tot}} h_v (T_{sat_{vac}})$
Chiller energy demand	$Q_{ch} = M^z_{c_{in}} C_p \left(T_{h_{hx_{in}}} - T_{ch_{out}}\right)/COP$ $z = lastz$	$Q_{ch} = M_{rec} C_p (T^z_{h_{out}} - T_{ch_{out}})/COP$ $z = lastz$			$Q_{ch} = M_{coolant} C_p (T_{ch_{in}} - T_{ch_{out}})/COP$
Heat transfer area	$A_{hx,cond,heater} = \frac{Q_{hx} LMTD}{U_{hx}}$				

Table 7. Mass balance equations and correlations for single stage MD systems

Mass balance					
	DC MD	AGMD	PGM D/CGMD	SGMD	V MD
Hot channel	$M^z_{h_{in}} = M_{rec} + M_f \quad z = 1$ $M^z_{h_{out}} = M^z_{h_{in}} - M^z_p \quad z \in Z$ $M^j_{h_{out}} = M_{rec} + M_{rej} \quad z = lastz$ $M^z_{h_{out}} X^z_{h_{out}} = M^z_{h_{in}} X^z_{h_{out}} \quad z \in Z$				

Table 7 (continued)

Cold channel $z \in Z$	$M_{c_{in}}^{z} + M_{p}^{z} = M_{c_{out}}^{z}$	$M_{c_{in}}^{z} = M_{c_{out}}^{z} = M_{h_{in}}^{z} = M_{rec} + M_{f}$	$M_{a_{in}}^{z} = M_{a_{out}}^{z}$ $M_{v_{in}}^{z} + M_{p}^{z} = M_{v_{out}}^{z} + M_{p}^{z}$	$M_{v_{in}}^{z} + M_{p}^{z} = M_{v_{out}}^{z}$
Permeate mass $z \in Z$	$M_{p}^{z} = J^{z} L^{z} W$ $M_{p_{tot}} = \sum_{z} M_{p}^{z}$			
Mass flux				
	DCMD	AGMD	PGMD/CGMD	SGMD	VMD
Permeate flux	$J^{z} = B\left(P_{sat_{h_m}}^{z} - P_{sat_{h_c}}^{z}\right)$	$J^{z} = B\left(P_{sat_{h_m}}^{z} - P_{sat_{ff}}^{z}\right)$	$J^{z} = B\left(P_{sat_{h_m}}^{z} - P_{sat_{g_m}}^{z}\right)$	$J^{z} = B\left(P_{sat_{h_m}}^{z} - P_{a_b}^{z}\right)$	$J^{z} = B\left(P_{sat_{h_m}}^{z} - P_{vac}^{z}\right)$
Air channel partial vapor pressure	-	-	-	$P_{a_b} = \frac{n_v}{n_a + n_v} P_T$: $P_{a_b} \leq P_{sat_{a_b}}$	-
Saturation pressure	$P_{sat} = \alpha \times \exp\left(23.5377 - \frac{4016.3632}{T + 273.15 - 38.6339}\right)$				
Permeability coefficient	$B = \frac{B_0}{\delta_m}$	$B = \left(\frac{\delta_m}{B_0} + \frac{\delta_g - \delta_{ff}}{B_a}\right)^{-1}$	$B = \frac{B_0}{\delta_m}$	$B = \left(\frac{\delta_m}{B_0} + \frac{d_{h_a}}{B_a sh}\right)^{-1}$	$B = \frac{B_0}{\delta_m}$
air gap/channel permeability coefficient	-	$B_a = \frac{D_{ab} M_w}{R T_{ave}}$		-	-
Diffusion coefficient	-	$D_{ab} = \frac{1.895 \times 10^{-5} \times T_{ave}^{2.072}}{P_T}$		-	-

Table 7 (continued)

Falling film thickness		$J^z = \frac{\rho_l(\rho_l - \rho_v)g\delta_f^2}{\mu}\frac{d\delta_f}{dz}$			
Concentration polarization	$X_m^z = X_b^z \exp\left(\frac{J^z}{k_{mass}\rho}\right)$				

Table 8. Correlations used in modeling MD process

Brine heat capacity	$C_p = 15.556m^2 - 241.78m + 4116.9$	[48]
Brine viscosity	$\mu = 2.239 \times 10^{-4} m^{0.2306}$	[48]
Brine density	$\rho = 1028.58 + 38.23m - 1.043m^2$	[48]
Brine thermal conductivity	$K = 0.6465 - 00581 \times 10^{-3}m - 0.000154 \times 10^{-4}m^2$	[48]
Effective thermal conductivity of a porous medium	$k_{eff} = \frac{k_{gas}(1 + 2\beta(1-\epsilon))}{1 - \beta(1-\epsilon)}$ $\beta = \left(k_{solid} - k_{gas}\right) / \left(k_{solid} + 2k_{gas}\right)$	[150]
Brine activity coefficient	$\alpha = 1 - 0.03112m - 0.001482m^2$	[151]
Hydraulic diameter	$d_h = \frac{4\varepsilon d_f \delta_{sp}}{\left(2d_f + 4(1-\varepsilon)\delta_{sp}\right)}$	[152]
Velocity	$V = \frac{M_{in}}{\left(W_m \delta_{sp} \varepsilon \rho\right)}$	
Reynolds number	$Re = \frac{\rho V d_h}{\mu}$	
Prandtl's number	$Pr = \frac{\mu C_p}{k}$	
Schmidt number	$Sc = \frac{\mu}{\rho . D}$	
Sherwood number	$Nu = 0.162Re^{0.656}Sc^{0.333}$	
Membrane Nusselt number	$Nu = 0.162Re^{0.656}Pr^{0.333}$	[153]

Table 8 (continued)

Condenser Nusselt number	$Nu = 0.37Re^{0.67}Pr^{0.33}$	[146]
Mass transfer coefficient	$k_{mass} = \frac{D.Sh}{d_h}$	
Pressure drop	$PD = \left(0.42 + \frac{189.3}{Re}\right)\frac{\rho V^2}{2d_h}$	[154]
Enthalpy of evaporation	$H_e = 2501.897149 - 2.407064037\ T + 1.92217\ \times 10^{-3}T - 1.5863 \times 10^{-5}T$	[155]
Saturated water enthalpy	$H_{sl} = -0.033635409 + 4.20557011\ T - 6.200339 \times 10^{-4}T^2 + 4.459374 \times 10^{-6}T^3$	[155]

Table 9. Detailed treatment cost split for various single stage MD configurations

		AGMD	DCMD	CGMD	PGMD	SGMD	VMD
Capital costs	Chiller	0.03	0.08	0.08	0.28	0.08	0.13
	Heat exchangers	0.01	0.91	0.011	0.03	1.33	0.05
	Membrane and modules	0.38	0.06	0.279	0.14	0.17	0.04
	Installations (pumps and pipes)	0.09	0.11	0.08	0.101	0.07	0.04
	Blower	-	-	-	-	0.01	-
	Vacuum pump	-	-	-	-	-	0.01

Table 9 (continued)

Operating costs	Chilling	1.16	2.79	2.64	9.48	2.59	4.33
	Heating	1.77	3.87	3.81	13.13	3.94	6.59
	Membrane replacement	0.85	0.14	0.63	0.31	0.38	0.09
	Pump	0.08	0.5	0.51	0.93	0.04	0.03
	Blower	-	-	-	-	1.05	-
	Vacuum pump	-	-	-	-	-	0.01
	Others	0.05	0.05	0.05	0.05	0.05	0.05

Appendix C . Multistage MD

Our modeling closely follows the approaches described in references [51, 53, 72, 96, 147-149], as summarized in tables A.5. and A.6, followed by correlations in table A.7.

It is worth noting that we assume that only the active layer contributes to mass transfer, as demonstrated in [100], and that the support layer has a negative impact on heat transfer, as described in [101].

Table 10. Heat balance equations for multistage MD systems

Heat flux for $z \in Z$, $i \in I$				
	DCMD	AGMD	PGMD/CGMD	VMD
Convective heat -hot channel	$q_{conv_h}^{i,z} = h_h^{i,z}\left(T_{h_b}^{i,z} - T_{h_m}^{i,z}\right)$			
Convective heat -cold channel	$q_{conv_c}^{i,z} = h_c^{i,z}\left(T_{c_m}^{i,z} - T_{c_b}^{i,z}\right)$			-
Conductive heat-membrane	$q_{cond_m}^{i,z} = \frac{k_m}{\delta_m}\left(T_{h_m}^{i,z} - T_{c_m}^{i,z}\right)$	$q_{cond_m}^{i,z} = \frac{k_m}{\delta_m}\left(T_{h_m}^{i,z} - T_{g_m}^{i,z}\right)$		-
Conductive heat-gap	-	$q_{cond_g}^{i,z} = \frac{k_g}{\delta_g - \delta_{ff}}\left(T_{g_m}^{i,z} - T_{ff}^{i,z}\right)$	$q_{cond_g}^{i,z} = \frac{k_g}{\delta_g}\left(T_{g_m}^{i,z} - T_{cw}^{i,z}\right)$	-
Conductive heat- falling film	-	$q_{cond_{ff}}^{i,z} = \frac{k_w}{\delta_{ff}}\left(T_{ff}^{i,z} - T_{cw}^{i,z}\right)$	-	-

Table 10 (continued)

Vapor expansion heat	-	-	-	$q_{exp}^{i,z} = RT_{h_m}^{i,z} \log\left(\frac{P_{h_m}^{i,z}}{P_{vac}}\right)$
Heat of evaporation/condensation	$q_e^{i,z}(T) = J^{i,z} H_e^{i,z}(T)$			
Heat flux balances for $z \in Z$, $i \in I$				
	DCMD	AGMD	PGMD/CGMD	VMD
Heat balace1	$q_{conv_h}^{i,z} = q_{cond_m}^{i,z} + q_e^{i,z}(T_{h_m}^{i,z}) + C_p^{i,z}(T_{h_m}^{i,z} - T_{h_b}^{i,z})$			$q_{conv_h}^{i,z} = q_{exp}^{i,z} + q_e^{i,z}(T_{h_m}^{i,z}) + C_p^{i,z}(T_{h_m}^{i,z} - T_{h_b}^{i,z})$
Heat balance2	$q_{conv_c}^{i,z} = q_{cond_m}^{i,z} + q_e^{i,z}(T_{c_m}^{i,z}) + C_p^{i,z}(T_{c_m}^{i,z} - T_{c_b}^{i,z})$	$q_{conv_c}^{i,z} = q_{cond_{ff}}^{i,z} + C_p^{i,z}(T_{ff}^{i,z} - T_{cp}^{i,z})$	$q_{conv_c}^{i,z} = q_{cond_m}^{i,z} + q_e^{i,z}(T_{g_m}^{i,z})$	-
Heat balance 3	-	$q_{cond_m}^{i,z} = q_{cond_g}^{i,z}$	$q_{cond_m}^{i,z} + q_e^{i,z}(T_{g_m}^{i,z}) = q_{cond_g}^{i,z}$	-
Heat balance 4	-	$q_{cond_{ff}}^{i,z} = q_{cond_g}^{i,z} + q_e^{i,z}(T_{ff}^{i,z})$	-	-
Enthalpy balance for $z \in Z$, $i \in I$				
	DCMD	AGMD	PGMD/CGMD	VMD
Enthalpy balance-hot channel	$q_{conv_h}^{i,z} L^{i,z} W^i = M_{h_{in}}^{i,z} C_p^{i,z}(T_{h_{in}}^{i,z} - T_{h_{out}}^{i,z})$			
Enthalpy balance-cold channel	$q_{conv_c}^{i,z} L^{i,z} W^i = M_{c_{in}}^{i,z} C_p^{z}(T_{c_{out}}^{i,z} - T_{c_{in}}^{i,z})$			-

Table 10 (continued)

Enthalpy balance- heater	$M_s^i h_{v_s} = (M_f^i + M_{rec}^i) C_p \left(T_{h_{in}}^z - T_{c_{hx_{out}}}^i\right)$, Z=1	$M_s^i h_{v_s} = (M_f^i + M_{rec}^i) C_p (T_{h_{in}}^{i,z} - T_{c_{out}}^{i,z})$, Z=1		$M_s h_{v_s} = \left(M_f^{plant} + M_{rec}\right) C_p \left(T_{c_{hx_{out}}}^i - T_{h_{in}}^{i,z}\right)$, Z=1, i=1
Enthalpy balance- external heat exchanger/ condenser	$(M_f^i + M_{rec}^i) C_p \left(T_{c_{hx_{out}}}^i - T_{mix(f,rec)}\right) = M_{c_{in}}^{i,z} C_p \left(T_{h_{hx_{in}}}^i - T_{h_{hx_{out}}}^i\right)$ z = lastz	-	-	$\left(M_f^{plant} + M_{coolant}\right) C_p \left(T_{c_{hx_{out}}}^i - T_{c_{hx_{in}}}^i -\right) = (M_{p_{stage}}^i + M_{flash}^i) H_e^{i,z} (T_{sat_{vac}}^i)$, i = lasti $\left(M_f^{plant} + M_{rec}\right) C_p \left(T_{c_{hx_{out}}}^i - T_{c_{hx_{in}}}^i -\right) = (M_{p_{stage}}^i + M_{flash}^i) H_e^{i,z} (T_{sat_{vac}}^i)$, i ≠ lasti
Chiller energy demand	$Q_{ch}^i = M_{c_{in}}^{i,z} C_p \left(T_{h_{hx_{out}}}^i - T_{ch_{out}}\right)/COP$ z = lastz	$Q_{ch}^i = M_{h_{out}}^{i,z} C_p (T_{h_{out}}^z - T_{ch_{out}})/COP$ z = lastz		$Q_{ch}^i = M_{coolant} C_p (T_{ch_{in}} - T_{ch_{out}})/COP$, i = lasti
Heat transfer area	$A_{i,hx/cond/heater} = \frac{Q_{i,hx} LMTD}{U_{hx}}$			
Equivalent work of separation	$SEC_{eq} = \frac{H_{turbine}^{steam} - H_{condenser}^{steam}}{3.6 \times GOR} \eta_{turbine} + \frac{Q_{ch}^i \times \rho}{M_f^{plant} \times 3600 \times RR}$			

Table 11. Mass balance equations and correlations for multistage MD systems

Mass balance $z \in Z$, $i \in I$				
	DCMD	AGMD	PGMD/CGMD	VMD
Overall mass balance	$M_f^i = M_{p_{stage}}^i + M_{rej}^i$			
Hot channel	$M_{h_{out}}^{i,z} = M_{h_{in}}^{i,z} - M_p^{i,z}$ $M_{h_{out}}^{i,z} X_{h_{out}}^{i,z} = M_{h_{in}}^{i,z} X_{h_{out}}^{i,z}$ $M_{h_{out}}^{i,z-1} = M_{h_{in}}^{i,z}, \quad z \neq 1$ $X_{h_{out}}^{i,z-1} = X_{h_{in}}^{i,z}, \quad z \neq 1$			
Hot channel inlet	$M_{h_{in}}^{i,z} = M_f^i + M_{rec}^i$, z=1 $M_{h_{in}}^{i,z} X_{h_{in}}^{i,z} = M_f^i X_f^i + M_{rec}^i X_{rec}^i, \quad z = 1$			$M_{h_{in}}^{i,z} = M_f^{plant} + M_{rec}$, i=1, z=1 $M_{h_{in}}^{i,z} X_{h_{in}}^{i,z} = M_f^{plant} X_f^{plant} + M_{rec} X_{rec}$, $i = 1, z = 1$
Hot channel outlet	$M_{h_{out}}^{i,z} = M_{rej}^i + M_{rec}^i$, $z = lastz$			$M_{h_{out}}^{i,z} = M_{rej}^i + M_{rec}$, $z = lastz, i = lasti$

Table 11 (continued)

Cold channel	$M_{c_{in}}^{i,z} + M_{p}^{i,z} = M_{c_{out}}^{i,z}$ $M_{c_{out}}^{i,z} = M_{c_{in}}^{i,z-1}$, $z \neq 1$	$M_{c_{in}}^{i,z} = M_{c_{out}}^{i,z} = M_{h_{in}}^{i,z}$ $M_{c_{out}}^{i,z} = M_{h_{in}}^{i,z}$, $z = 1$ $M_{c_{out}}^{i,z} = M_{c_{in}}^{i,z-1}$, $z \neq 1$		$M_{v_{in}}^{i,z} + M_{p}^{i,z} = M_{v_{out}}^{i,z}$ $M_{v_{out}}^{i,z} = M_{v_{in}}^{i,z-1}$, $z \neq 1$
Permeate mass	$M_{p}^{i,z} = J^{i,z} L^{i,z} W$ $M_{p_{tot}} = \sum_{i} \sum_{z} M_{p}^{i,z}$ $M_{p_{stage}}^{i} = \sum_{z} M_{p}^{i,z}$			
Flashed vapor	-			$M_{flash}^{i,z} \times H_{e}^{i,z}(T_{sat_{vac}}^{i}) = M_{p_{stage}}^{i-1} \times C_{p_f}^{z} \times (T_{sat_{vac}}^{i-1} - T_{sat_{vac}}^{i})$, $i \neq 1$
	DCMD	AGMD	PGMD/CGMD	VMD
Permeate flux	$J^{i,z} = B\left(P_{sat_{h_m}}^{i,z} - P_{sat_{c_m}}^{i,z}\right)$	$J^{i,z} = B\left(P_{sat_{h_m}}^{i,z} - P_{sat_{ff}}^{i,z}\right)$	$J^{i,z} = B\left(P_{sat_{h_m}}^{i,z} - P_{sat_{g_m}}^{i,z}\right)$	$J^{i,z} = B\left(P_{sat_{h_m}}^{i,z} - P_{vac}^{i,z}\right)$
Saturation pressure	$P_{sat} = \alpha \times \exp\left(23.5377 - \frac{4016.3632}{T + 273.15 - 38.6339}\right)$			
Permeability coefficient	$B = \frac{B_0}{\delta_m}$	$B = \left(\frac{\delta_m}{B_0} + \frac{\delta_g - \delta_{ff}}{B_a}\right)^{-1}$	$B = \frac{B_0}{\delta_m}$	$B = \frac{B_0}{\delta_m}$
Air gap/channel permeability coefficient	-	$B_a = \frac{D_{ab} M_w}{R T_{ave}}$	-	-
Diffusion coefficient	-	$D_{ab} = \frac{1.895 \times 10^{-5} \times T_{ave}^{2.072}}{P_T}$	-	-

Table 11 (continued)

Falling film thickness	-	$J^{i,z} = \frac{\rho_l(\rho_l - \rho_v)g\delta_f^2}{\mu}\frac{d\delta_f}{dz}$	-	-
Concentration polarization	$X_m^{i,z} = X_b^{i,z}\exp\left(\frac{J^{i,z}}{k_{mass}\rho}\right)$			

Table 12. Stages connections and stages- multistage MD

	DCMD	AGMD	PGMD/CGMD	VMD
Mass connection	$M_{rej}^{i-1,lastz} = M_f^i,\ i \neq 1$ $X_{rej_{out}}^{i-1,lastz} = X_f^i,\ i \neq 1$			$M_{h_{out}}^{i-1,lastz} = M_f^i$ $X_{h_{out}}^{i-1,lastz} = X_f^i$
Temperature connection	$T_{h_{out}}^{i-1,lastz} = T_f^i$	$T_{ch_{out}}^{i-1,lastz} = T_f^i$		$T_{h_{out}}^{i-1,lastz} = T_f^i$
VMD's condensers cold side	-			$T_{c_{hx_{in}}}^i = T_{c_{hx_{out}}}^{i+1}$, $M_{c_{hx_{in}}}^i = M_f^{plant} + M_{rec}$, $i \neq lasti$
VMD's condensers cold side	-			$T_{h_{hx_{in}}}^i =$ $T_{h_{hx_{out}}}^i = T_{sat_{vac}}^i$, $M_{h_{hx_{in}}}^i = (M_{p_{stage}}^i + M_{flash}^i$

Table 13.Detailed treatment cost split for various multistage MD configurations

		AGMD	DCMD	CGMD	PGMD	VMD
Capital costs	Number of stages	5	8	8	16	12
	Chiller	0.02	0.04	0.03	0.08	0.03
	Heat exchangers	0.01	0.79	0.01	0.03	0.37
	Membrane and modules	0.37	0.11	0.41	0.27	0.09
	Installations (pumps and pipes)	0.23	0.37	0.24	0.46	0.26
	Vacuum pump	-	-	-	-	0.003
Operating costs	Chilling	0.58	1.37	1.08	2.8	0.97
	Heating	1.96	1.96	1.86	4.25	1.44
	Membrane replacement	0.84	0.24	0.94	0.6	0.2
	Pump	0.06	0.25	0.26	0.28	0.09
	Vacuum pump	-	-	-	-	0.03
	Others	0.05	0.05	0.05	0.05	0.05

Figure 39. Operating and capital cost as a function of number of stages

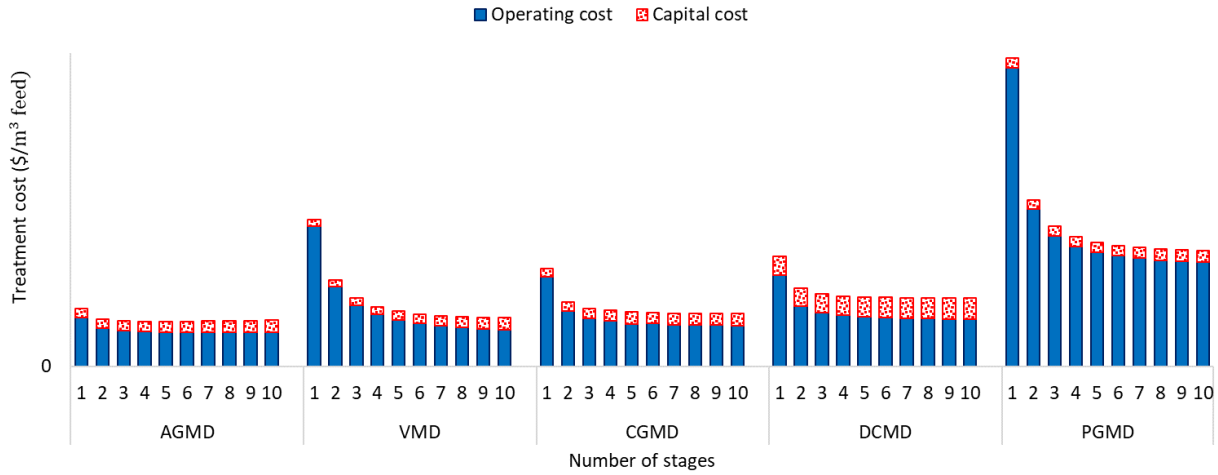

Figure 40. Stage heat recovery and thermal efficiency for various MD configuration at their optimum number of stages

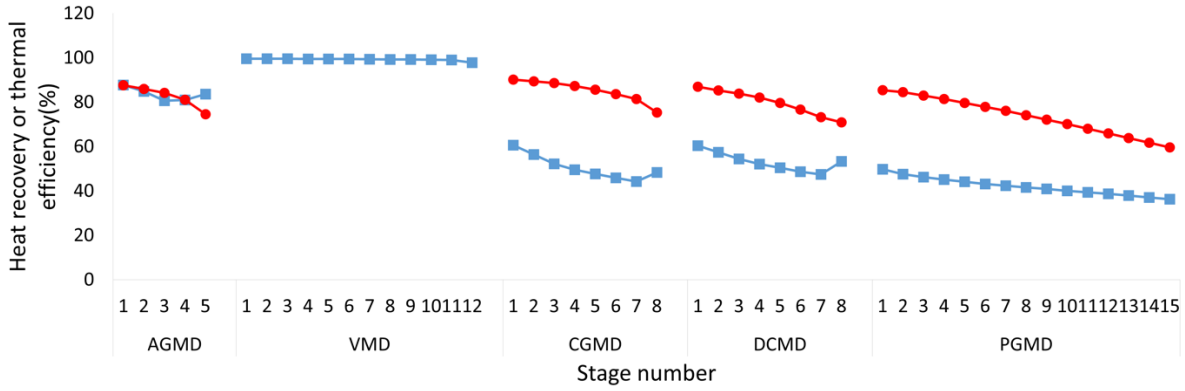

Figure 41. Water recovery distribution as a function of number of stages.

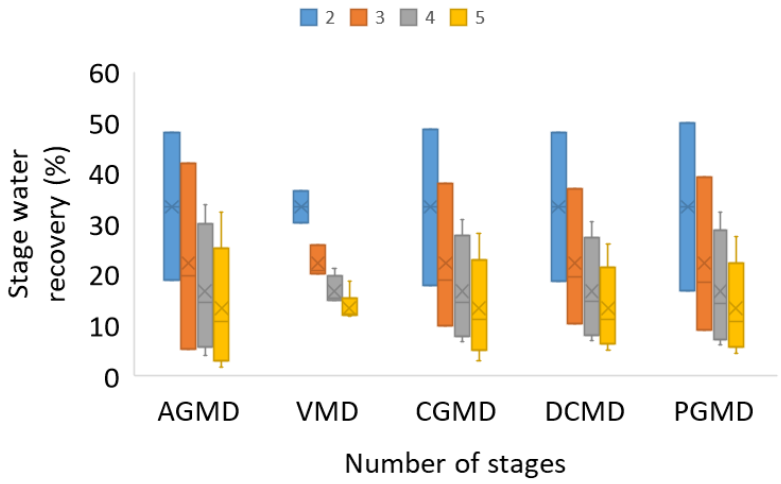

Figure 42. Stage specific area for various MD configurations at their studied number of stages

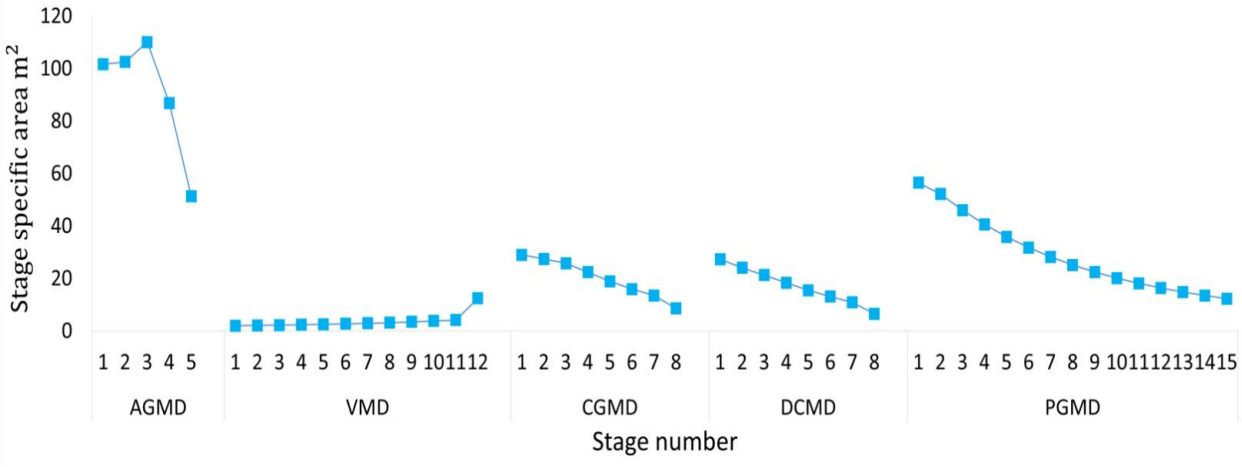

Appendix D . OARO

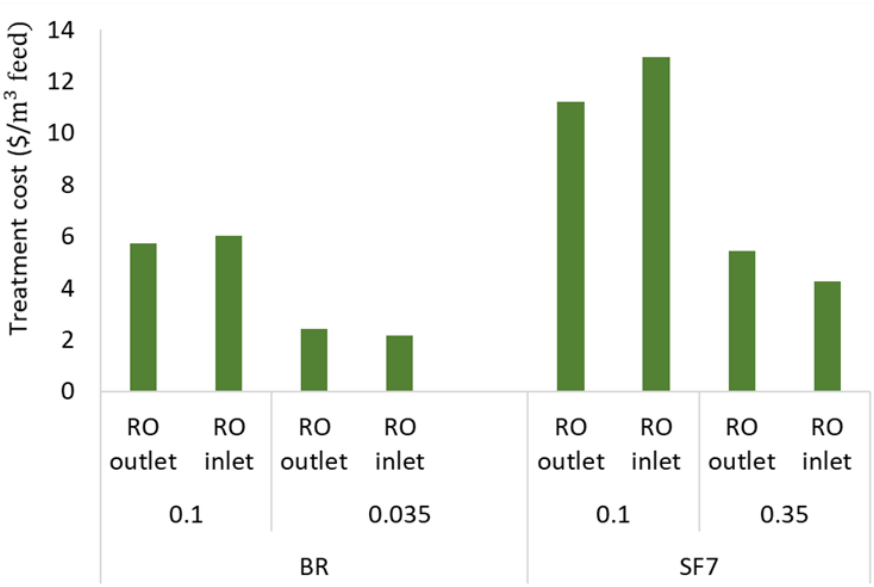

b)

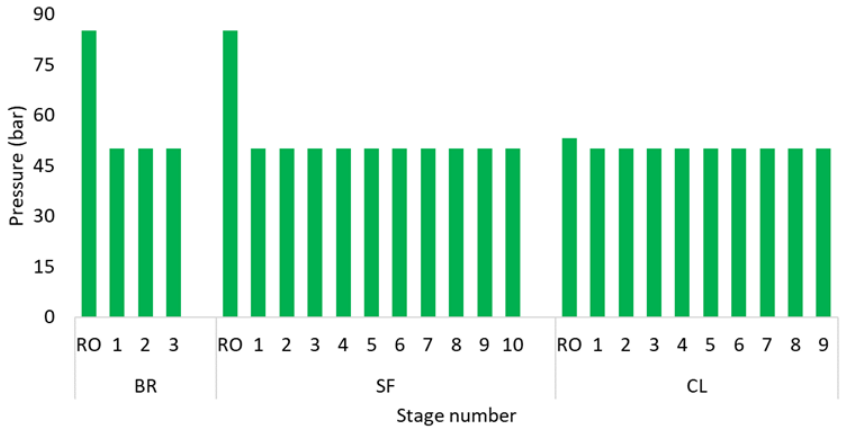

c)

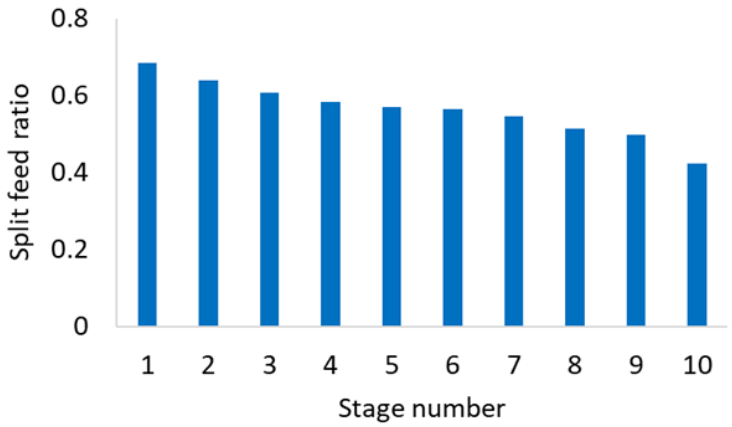

Figure 43. a) Treatment cost of BR and SF configurations versus feed entrance location; b) applied hydraulic pressure at concentrating inlet of each stage of BR, CL, and SF configurations; and c) Feed split ratio of each stage of SF configuration.

Table 14. OARO operating and capital cost breakdown- OARO

		BR-OARO	SF-OARO	CL- OARO
Capital costs	Number of stages	3	10	9
	Membrane	1.332	1.350	1.511
	High pressure pump	0.01	0.01	0.02
	Low pressure/booster pump	0.296	0.716	1.217
	ERD devices	0.020	0.027	0.031
Operating costs	Electricity	0.881	0.913	1.399
	Membrane replacement	2.490	2.523	2.824
	Others	0.054	0.072	0.091

Table 15. Plant characteristics and annual cost estimation

Produced water temperature (°C)	20
Produced water salinity (%)	10
Reject brine salinity (%)	30
Plant capacity (kg/s)	10
Maximum brine salinity (%)	30
Maximum RO permeate salinity (%)	0.05
Plant life (year)	20
Interest rate (5)	5

Table 16. Membrane properties- OARO

		Ref
CFRO membrane water permeability coefficient $\left(\frac{L}{m^2h-bar}\right)$	2.49	[122]
RO membrane water permeability coefficient $\left(\frac{L}{m^2h-bar}\right)$	1.51	[116, 156]
CFRO membrane salt permeability coefficient $\left(\frac{L}{m^2h}\right)$	0.39	[122]
RO membrane salt permeability coefficient $\left(\frac{L}{m^2h}\right)$	0.12	[116, 156]
CFRO membrane burst pressure (bar)	50	[122]
RO membrane burst pressure (bar)	85	[116]
CFRO membrane structural parameter (μm)	564	[122]

Table 17. Capital cost data- OARO

Capital Cost	Base price	Base capacity	Scale up coefficient	Ref.
CFRO Membrane	50 $(\frac{\$}{m^2})$			[116]
RO Membrane (DCMD)	30 $(\frac{\$}{m^2})$			[116, 156]
High pressure pump	3134.76	$1\frac{m^3}{h}$	0.54	[116]
Low pressure/booster pump	8000 $(\frac{\$}{pump})$	1 pump	1	[65]
Low pressure/booster pump	240	$1\frac{m^3}{h}$	0.9	

Table 18. Operating cost data- OARO

Operating cost		Ref.
Electricity	$0.069\left(\frac{\$}{kwh}\right)$	[66]
Membrane replacement	15% of initial membrane area/year	[157]
Labor and chemical cost	3 % of initial investment/year	[157]

Table 19. Overall mass balance- OARO

	COMRO	BR-OARO	SF-OARO	CL-OARO
Total mass balance	$M_f^{plant} = M_{rej} + M_d$			$M_f^{plant} = M_{rej} + M_d + M_{pg}$
Total salt balance	$M_f^{plant} X_f^{plant} = M_{rej} X_{rej} + M_d M_d$			$M_f^{plant} X_f^{plant} = M_{rej} X_{rej} + M_d M_d + M_{pg} X_{c_{out}}^{i-1,lastz}$, i=lasti
Reject salinity and flowrate	$M_{rej} = M_{c_{out}}^{lasti,lastz}$, $X_{rej} = X_{c_{out}}^{lasti,lastz}$			$M_{rej} = M_{c_{out}}^{lasti,lastz}$, $X_{rej} = X_{c_{out}}^{lasti,lastz}$
Permeate salinity and flowrate	$M_d = M_{d_{out}}^{firsti,firstz}$, $X_d = X_{d_{out}}^{firsti,firstz}$			

Table 20. Equations of mass and energy balance between slices of one stage- OARO

Water flux	$J_w^{i,z} = a_w\left(P_c^{i,z} - P_d^{i,z} - OP_{c_m}^{i,z} + OP_{d_m}^{i,z}\right)$
Salt flux	$J_s^{i,z} = a_s\left(C_{c_m}^{i,z} - C_{d_m}^{i,z}\right)$
Concentrating side mass balance	$M_{C_{out}}^{i,z} = M_{C_{in}}^{i,z} - \left(J_w^{i,z} \times \rho_w + J_s^{i,z}\right)L^{i,z}W^i,$ $M_{C_{in}}^{i,z} = M_{C_{out}}^{i,z-1}$
Diluting side mass balance	$M_{d_{in}}^{i,z} = M_{d_{out}}^{i,z} - \left(J_w^{i,z} \times \rho_w + J_s^{i,z}\right)L^{i,z}W^i,$ $M_{d_{in}}^{i,z} = M_{d_{out}}^{i,z+1}$
Concentrating side salt balance	$M_{C_{out}}^{i,z}X_{C_{out}}^{i,z} = M_{C_{in}}^{i,z}X_{C_{in}}^{i,z} - J_s^{i,z}L^{i,z}W^i,$ $X_{C_{in}}^{i,z} = X_{C_{out}}^{i,z-1}$
Diluting side salt balance	$M_{d_{in}}^{i,z}X_{d_{in}}^{i,z} = M_{d_{out}}^{i,z}X_{d_{out}}^{i,z} - J_s^{i,z}L^{i,z}W^i,$ $X_{d_{in}}^{i,z} = X_{d_{out}}^{i,z+1}$
Concentrating side pressure change	$P_{C_{in}}^{i,z} - P_{C_{out}}^{i,z} = PD_c^{i,z}L^{i,z},$ $P_{C_{in}}^{i,z} = P_{C_{out}}^{i,z-1} + \Delta P_{bs_c}^{i,z}$
Diluting side pressure change	$P_{d_{in}}^{i,z} - P_{d_{out}}^{i,z} = PD_d^{i,z}L^{i,z},$ $P_{d_{in}}^{i,z} = P_{d_{out}}^{i,z+1} + \Delta P_{LP_d}^{i,z},$ $PD_d^{first i,z} = 0$

Table 21. Equations of mass and energy balance between stages- OARO

	COMRO	BR-OARO	CL-OARO	SF-OARO
Concentrating side inlet mass flow rate	$M_{c_{in}}^{i,firstz} = M_{c_{out}}^{i-1,lastz}$, $i \neq firsti$	$M_{c_{in}}^{i,firstz} = M_{c_{out}}^{i-1,lastz} + M_f^i$, $i \neq firsti$	$M_{c_{in}}^{i,firstz} = M_{d_{out}}^{i+1,firstz}$, $i \neq lasti$	$M_{c_{in}}^{i,firstz} = \left(M_{c_{out}}^{i-1,lastz} + M_{d_{out}}^{i+1,firstz} + M_f^i\right) \times SR$, $i \neq lasti, firsti$
	$M_{c_{in}}^{i,firstz} = M_{d_{out}}^{i+1,firstz}$, $i = firsti$	$M_{c_{in}}^{i,firstz} = M_{d_{out}}^{i+1,firstz} + M_f^i$, $i = firsti$	$M_{c_{in}}^{i,firstz} = M_f^{plant}$, $i = lasti$	$M_{c_{in}}^{i,firstz} = \left(M_{c_{out}}^{i-1,lastz} + M_f^i\right) \times SR$, $i = lasti$
				$M_{c_{in}}^{i,firstz} = \left(M_{d_{out}}^{i+1,firstz} + M_f^i\right) \times SR$, $i = firsti$
Diluting side inlet mass flow rate	$M_{d_{in}}^{i,lastz} = M_{d_{out}}^{i+1,firstz}$, $i \neq lasti, firsti$	$M_{d_{in}}^{i,lastz} = M_{d_{out}}^{i+1,firstz}$, $i \neq lasti, firsti$	$M_{d_{in}}^{i,lastz} = M_{c_{out}}^{i-1,lastz} + M_{rec}^{i-1} - M_{rec}^{i}$, $i \neq lasti, i > 2$	$M_{d_{in}}^{i,lastz} = \left(M_{c_{out}}^{i-1,lastz} + M_{d_{out}}^{i+1,firstz} + M_f^i\right) \times (1 - SR)$, $i \neq lasti, firsti$
	$M_{d_{in}}^{i,lastz} = M_f^{plant}$, $i = lasti$	$M_{d_{in}}^{i,lastz} = M_{rec}$, $i = lasti$	$M_{d_{in}}^{i,lastz} = M_{c_{out}}^{i-1,lastz} + M_{rec}^{i-1} - M_{pg}$, $i = lasti$	
			$M_{d_{in}}^{i,lastz} = M_{c_{out}}^{i-1,lastz} - M_{rec}^{i}$, $i = 2$	$M_{d_{in}}^{i,firstz} = \left(M_{c_{out}}^{i-1,lastz} + M_f^i\right) \times (1 - SR)$, $i = lasti$

Table 21 (continued)

Concentrating side inlet salinity	$X_{c_{in}}^{i,firstz} = X_{c_{out}}^{i-1,lastz}$, $i \neq firsti$	$M_{c_{in}}^{i,firstz} X_{c_{in}}^{i,firstz} = M_{c_{out}}^{i-1,lastz} X_{c_{out}}^{i-1,lastz} + M_f^i X_f^{plant}$, $i \neq firsti$	$X_{c_{in}}^{i,firstz} = X_{d_{out}}^{i+1,firstz}$, $i \neq lasti$	$M_{c_{in}}^{i,firstz} X_{c_{in}}^{i,firstz} = \left(M_{c_{out}}^{i-1,lastz} X_{c_{out}}^{i-1,lastz} + M_{d_{out}}^{i+1,firstz} X_{d_{out}}^{i+1,firstz} + M_f^i X_f^{plant}\right) \times SR$, $i \neq lasti, firsti$
	$X_{c_{in}}^{i,firstz} = X_{d_{out}}^{i+1,firstz}$, $i = firsti$	$M_{c_{in}}^{i,firstz} X_{c_{in}}^{i,firstz} = M_{d_{out}}^{i+1,firstz} X_{d_{out}}^{i+1,firstz} + M_f^i X_f^{plant}$, $i = firsti$	$X_{c_{in}}^{i,firstz} = X_f^{plant}$, $i = lasti$	$M_{c_{in}}^{i,firstz} X_{c_{in}}^{i,firstz} = \left(M_{c_{out}}^{i-1,lastz} X_{c_{out}}^{i-1,lastz} + M_f^i X_f^{plant}\right) \times SR$, $i = lasti$
				$M_{c_{in}}^{i,firstz} X_{c_{in}}^{i,firstz} = \left(M_{d_{out}}^{i+1,firstz} X_{d_{out}}^{i+1,firstz} + M_f^i X_f^{plant}\right) \times SR$, $i = firsti$
Diluting side inlet salinity	$X_{d_{in}}^{i,lastz} = X_{d_{out}}^{i+1,firstz}$, $i \neq lasti, firsti$	$X_{d_{in}}^{i,lastz} = X_{d_{out}}^{i+1,firstz}$, $i \neq lasti, firsti$	$M_{d_{in}}^{i,lastz} X_{d_{in}}^{i,lastz} = M_{c_{out}}^{i-1,lastz} X_{c_{out}}^{i-1,lastz} + M_{rec}^{i-1} X_{c_{out}}^{i-2,lastz} - M_{rec}^i X_{c_{out}}^{i-1,lastz}$, $i \neq lasti, i > 2$	$M_{d_{in}}^{i,lastz} X_{d_{in}}^{i,lastz} = \left(M_{c_{out}}^{i-1,lastz} X_{c_{out}}^{i-1,lastz} + M_{d_{out}}^{i+1,firstz} X_{d_{out}}^{i+1,firstz} + M_f^i X_f^{plant}\right) \times (1 - SR)$, $i \neq lasti, firsti$

Table 21 (continued)

	$X_{d_{in}}^{i,lastz} = X_f^{plant}$, i = lasti	$X_{d_{in}}^{i,lastz} = X_{rej}$, i = lasti	$M_{d_{in}}^{i,lastz} X_{d_{in}}^{i,lastz} = M_{c_{out}}^{i-1,lastz} X_{c_{out}}^{i-1,lastz} + M_{rec}^{i-1} X_{c_{out}}^{i-2,lastz} - M_{pg} X_{c_{out}}^{i-1,lastz}$, i = lasti	
			$M_{d_{in}}^{i,lastz} X_{d_{in}}^{i,lastz} = M_{c_{out}}^{i-1,lastz} X_{c_{out}}^{i-1,lastz} - M_{rec}^{i} X_{c_{out}}^{i-1,lastz}$, i = 2	$M_{d_{in}}^{i,firstz} X_{d_{in}}^{i,firstz} = \left(M_{c_{out}}^{i-1,lastz} X_{c_{out}}^{i-1,lastz} + M_f^i X_f^{plant}\right) \times (1 - SR)$, i = lasti
Feed inlet	-	$M_f^i = M_f^{plant}$, i=feed inlet $M_f^i = 0$, i ≠ feed inlet	-	$M_f^i = M_f^{plant}$, i=feed inlet $M_f^i = 0$, i ≠ feed inlet
Concentrating side stage inlet pressure	$P_{C_{in}}^{i,firstz} = P_{C_{out}}^{i-1,lastz} - \Delta P_{ERD}^{i-1} + \Delta P_{HP+ERD}^{i}$, i = 2	$P_{C_{in}}^{i,firstz} = P_{C_{out}}^{i-1,lastz} - \Delta P_{ERD}^{i-1} + \Delta P_{HP}^{i}$, i = 2	$P_{C_{in}}^{i,firstz} = 1 + \Delta P_{HP+ERD}^{i}$	$P_{C_{in}}^{i,firstz} = 1 + \Delta P_{HP+ERD}^{i}$
	$P_{C_{in}}^{i,firstz} = P_{C_{out}}^{i-1,lastz} - \Delta P_{ERD}^{i-1} + \Delta P_{HP+ERD}^{i}$, i ≠ 2	$P_{C_{in}}^{i,firstz} = P_{C_{out}}^{i-1,lastz} - \Delta P_{ERD}^{i-1} + \Delta P_{HP}^{i}$, i ≠ 2		

Table 21 (continued)

Diluting side stage inlet pressure	$P_{d_{in}}^{i,lastz} = P_{C_{out}}^{i+1,firstz} + \Delta P_{LP_d}^{i,lastz}$, $i \neq lasti$	$P_{d_{in}}^{i,lastz} = P_{C_{out}}^{i+1,firstz} + \Delta P_{LP_d}^{i,lastz}$, $i \neq lasti$	$P_{d_{in}}^{i,lastz} = 1 + \Delta P_{LP_d}^{i,lastz}$	$P_{d_{in}}^{i,lastz} = 1 + \Delta P_{LP_d}^{i,lastz}$
	$P_{d_{in}}^{i,lastz} = 1 + \Delta P_{LP_d}^{i,lastz}$, $i = lasti$	$P_{d_{in}}^{i,lastz} = 1 + \Delta P_{LP_d}^{i,lastz}$, $i = lasti$		

*Inlet salinity and flowrate of the dilute/permeate side of the initial RO stage is set to zero for all configurations

Table 22. Power consumption calculation- OARO

<table>
<tr><th></th><th colspan="2">COMRO</th><th colspan="2">BR-OARO</th><th colspan="2">CL-OARO</th><th colspan="2">SF-OARO</th></tr>
<tr><td>Stage total HP pump power consumption</td><td colspan="4">$$TP_{HP}^{i} = \left(\frac{M_{c_{in}}^{i,firstz}\Delta P_{HP+ERD}^{i}}{\rho_{c_{in}}^{i,firstz}} - \frac{M_{c_{out}}^{i,lastz}\left(P_{C_{out}}^{i,lastz}-1\right)\eta_{px}}{\rho_{c_{out}}^{i,lastz}}\right)\frac{1}{36\,\eta_p},\quad i = firsti$$
$$TP_{HP}^{i} = \left(\frac{M_{c_{in}}^{i,firstz}\Delta P_{HP+ERD}^{i}}{\rho_{c_{in}}^{i,firstz}} - \frac{M_{c_{out}}^{lasti,lastz}\left(P_{C_{out}}^{lasti,lastz}-1\right)\eta_{px}}{\rho_{c_{out}}^{lasti,lastz}}\right)\frac{1}{36\,\eta_p},\quad i = 2$$
$$TP_{HP}^{i} = \left(\frac{M_{c_{in}}^{i,firstz}\Delta P_{HP+ERD}^{i}}{\rho_{c_{in}}^{i,firstz}}\right)\frac{1}{36\,\eta_p},\quad i > 2$$</td><td colspan="4">$$TP_{HP}^{i} = \left(\frac{M_{c_{in}}^{i,firstz}\Delta P_{HP+ERD}^{i}}{\rho_{c_{in}}^{i,firstz}} - \frac{M_{c_{out}}^{i,lastz}\left(P_{C_{out}}^{i,lastz}-1\right)\eta_{px}}{\rho_{c_{out}}^{i,lastz}}\right)\frac{1}{36\,\eta_p}$$</td></tr>
<tr><td>Stage total LP/booster pump power consumption</td><td colspan="8">$$TP_{LP/bs}^{i} = \sum_{z}\frac{M_{c/d_{in}}^{i,z}\Delta P_{LP_d}^{i,z}}{36\,\rho_{d_{in}}^{i,z}\eta_p}$$</td></tr>
<tr><td>Total unit power consumption</td><td colspan="8">$$TUP = \frac{\rho_f^{plant}}{M_f^{plant}}\sum_{i}\left(TP_{HP}^{i} + TP_{LP/bs}^{i}\right)$$</td></tr>
</table>

Table 23. Correlations

Brine viscosity	$\mu = 2.239 \times 10^{-4} m^{0.2306}$	[48]
Brine density	$\rho = 1028.58 + 38.23m - 1.043m^2$	[48]
Osmotic pressure	$OP = \frac{iRT}{M_w} C(3.33 \times 10^{-6} C^2 + 1.78 \times 10^{-4} C + 0.918)$	[116]
Hydraulic diameter	$d_h = \frac{4\varepsilon d_f \delta_{sp}}{(2d_f + 4(1-\varepsilon)\delta_{sp})}$	[152]
Velocity	$V = \frac{M_{in}}{(W_m \delta_{sp} \varepsilon \rho)}$	
Reynolds number	$Re = \frac{\rho V d_h}{\mu}$	
Prandtl's number	$Pr = \frac{\mu C_p}{k}$	
Schmidt number	$Sc = \frac{\mu}{\rho . D}$	
Sherwood number	$Sh = 0.2 Re^{0.57} Sc^{0.4}$	[158]
Mass transfer coefficient	$k_{mass} = \frac{D . Sh}{d_h}$	
Pressure drop	$PD = \left(0.42 + \frac{189.3}{Re}\right) \frac{\rho V^2}{2 d_h}$	[154]
CP coefficient-concentrating side	$A^{i,z} = J_w^{i,z} \times \left(\frac{S}{D} + \frac{1}{k_{mass}}\right)$	[116]
CP coefficient-Diluting side	$B^{i,z} = \frac{J_w^{i,z}}{k_{mass}}$	[116]

Appendix E . MVR

a)

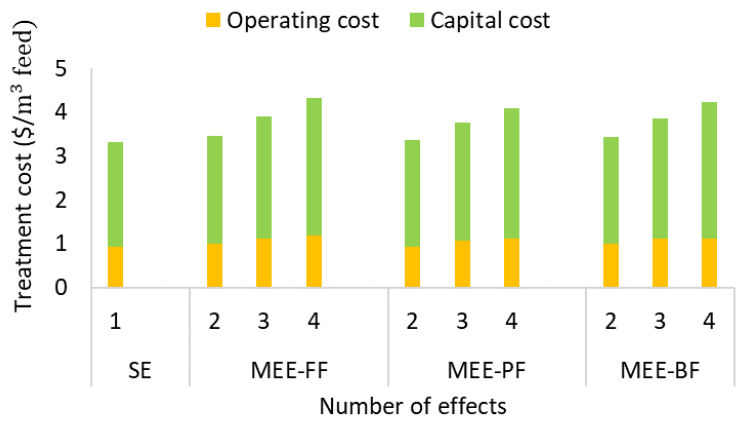

b)

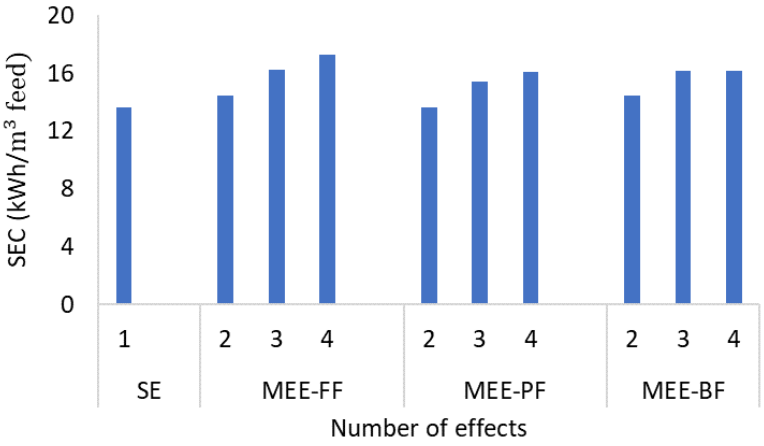

c)

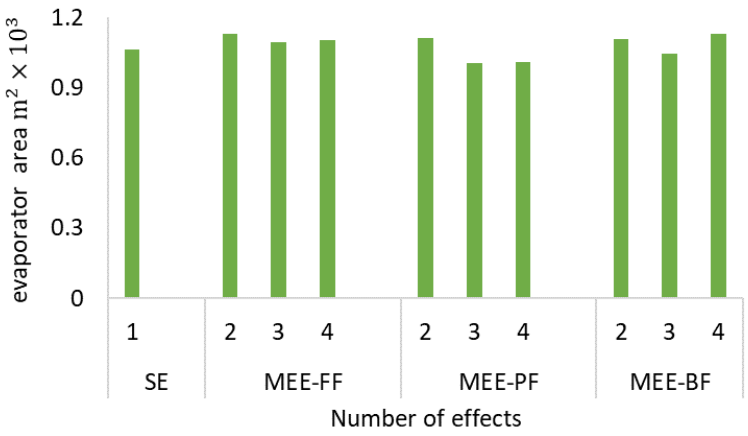

Figure 44. a) operating and capital costs, b) specific energy consumption, and c) evaporator area for various MVR configurations

Table 24. MVR mass and energy balance equations

	Forward feed	Backward feed	Parallel feed
	Mass balances		
Total distillate	$M_{d_{total}} = \sum_z M_d^z$		
Effect feed	$M_f^z = M_b^{z-1}$	$M_f^z = M_b^{z+1}$	$M_{fin} = \sum_z M_f^z$
Effects mass balance	$M_f^z = M_v^z + M_b^z$		
Effect heating vapor	$M_v^z = M_d^{z-1}$ z>1 $M_v^1 = M_d^{lastz}$ z=1		
Effect distillate	$M_d^z = M_{df}^z + M_{db}^z$ z>1 $M_d^z = M_{db}^z$ z=1	$M_d^z = M_{db}^z$	$M_d^z = M_{df}^z + M_{db}^z$ z>1 $M_d^z = M_{db}^z$ z=1
Total mass balance	$M_f^1 = M_{d_{total}} + M_{rej}^{lastz}$	$M_f^{lastz} = M_{d_{total}} + M_{rej}^1$	$\sum_z M_f^z = M_{d_{total}} + \sum_z M_{rej}^z$
Total salt balance	$M_f^1 \times x_f^1 = M_{rej}^{lastz} \times x_{rej}^{lastz}$	$M_f^{lastz} \times x_f^{lastz} = M_{rej}^1 \times x_{rej}^1$	$\sum_z M_f^z \times x_f^z = \sum_z M_{rej}^z \times x_{rej}^z$
Effect salt balance	$M_f^z \times x_f^z = M_{rej}^z \times x_{rej}^z$	$M_f^z \times x_f^z = M_{rej}^z \times x_{rej}^z$	$M_f^z \times x_f^z = (M_{rej}^z + M_{df}^z) \times x_{rej}^z$

Table 24 (continued)

Energy balance			
Effect condenser temperature	$T_v^z = T_d^{z-1}$		
Effect top brine temperature	$T_b^z = T_d^z + BPE$		
Effect flashed vapor	$M_{df}^z \times h_{lv_b}^{\ z} = M_f^z \times C_{p_f}^z \times \left(T_b^z - T_b^{z-1}\right)$	-	$M_{df}^z \times h_{lv_b}^{\ z} = C_{p_{rej}}^{z-1} \times \left(T_b^z - T_b^{z-1}\right) \times \sum_1^{z-1} M_{rej}^{z-1}$
Evaporator/condenser energy balance (first effect)	$M_{db}^z \times h_{lv_b}^{\ z} + M_f^z \times C_{p_f}^z \times \left(T_b^z - T_f^{ph}\right) = M_v^z \times h_{lv_v}^{\ z} + M_v^z \times C_{p_v}^z \times \left(T_{sup}^z - T_v^z\right)$	$M_{db}^z \times h_{lv_b}^{\ z} + M_f^z \times C_{p_f}^z \times \left(T_b^z - T_b^{z+1}\right) = M_v^z \times h_{lv_v}^{\ z} + M_v^z \times C_{p_v}^z \times \left(T_{sup}^z - T_v^z\right)$	$M_{db}^z \times h_{lv_b}^{\ z} + M_f^z \times C_{p_f}^z \times \left(T_b^z - T_f^{ph}\right) = M_v^z \times h_{lv_v}^{\ z} + M_v^z \times C_{p_v}^z \times \left(T_{sup}^z - T_v^z\right)$
Evaporator/condenser energy balance (middle effects)	$M_{db}^z \times h_{lv_b}^{\ z} = M_v^z \times h_{lv_v}^{\ z}$ $z > 1$	$M_{db}^z \times h_{lv_b}^{\ z} + M_f^z \times C_{p_f}^z \times \left(T_b^z - T_b^{z+1}\right) = M_v^z \times h_{lv_v}^{\ z}$	$M_{db}^z \times h_{lv_b}^{\ z} + M_f^z \times C_{p_f}^z \times \left(T_b^z - T_f^{ph}\right) = M_v^z \times h_{lv_v}^{\ z}$
Evaporator/condenser energy balance (last effect)	-	$M_{db}^z \times h_{lv_b}^{\ z} + M_f^z \times C_{p_f}^z \times \left(T_b^z - T_f^{ph}\right) = M_v^z \times h_{lv_v}^{\ z}$	-
Compressor work	$W_{comp} = \frac{\gamma}{\gamma - 1} \times \frac{M_d^{lastz} \times R}{\eta_{comp} \times M_w} \times \left(T_e^{lastz} + 273.15\right) \times \left(CR^{\frac{\gamma-1}{\gamma}} - 1\right)$		
Isentropic compression	$\frac{\left(T_{is}^{comp} + 273.15\right)}{\left(T_e^{lastz} + 273.15\right)} = CR^{\frac{\gamma-1}{\gamma}}$		
Non ideal isentropic compression (superheated temperature)	$T_s = T_e^{lastz} + \frac{T_{is}^{comp} - T_e^{lastz}}{\eta_{is}}$		
Distillate heat exchanger	$M_{f1} \times C_{p_f} \times \left(T_f^{in} - T_f^{ph1}\right) = M_b^{lastz/firstz} \times C_{p_b}^{lastz/firstz} \times \left(T_b^{lastz/firstz} - T_b^{out}\right)$		
Brine heat exchanger	$M_{f2} \times C_{p_f} \times \left(T_f^{in} - T_f^{ph2}\right) = M_d^{Total} \times C_{p_d}^{Total} \times \left(T_d^{lastz} - T_d^{out}\right)$		
Evaporator heat transfer	$A_{evap} = \frac{Q_{evap} \times (T_d^z - T_b^z)}{U_{evap}}$		
Preheaters heat transfer	$A_{hx} = \frac{Q_{hx} LMTD_{hx}}{U_{hx}}$		
Objective function	$\min \sum UCC + \sum UOC$		

BIBLIOGRAPHY

1. Scanlon, B.R., et al., *Will water issues constrain oil and gas production in the United States?* Environmental science & technology, 2020. **54**(6): p. 3510-3519.

2. Brown, b., Kahan. A. *The U.S. leads global petroleum and natural gas production with record growth in 2018*. 2019; Available from: https://www.eia.gov/todayinenergy/detail.php?id=40973.

3. ; Available from: https://www.eia.gov/energyexplained/natural-gas/imports-and-exports.php.

4. Council, G.P., *Modern Shale Gas Development in the United States: A Primer, prepared for the US Department of Energy.* National Energy Technology Laboratory (NETL) with ALL Consulting (Oklahoma City, OK: April 2009), 2009: p. 13.

5. Abualfaraj, N., P.L. Gurian, and M.S. Olson, *Characterization of Marcellus shale flowback water.* Environmental Engineering Science, 2014. **31**(9): p. 514-524.

6. Estrada, J.M. and R. Bhamidimarri, *A review of the issues and treatment options for wastewater from shale gas extraction by hydraulic fracturing.* Fuel, 2016. **182**: p. 292-303.

7. Entrekin, S., et al., *Rapid expansion of natural gas development poses a threat to surface waters.* Frontiers in Ecology and the Environment, 2011. **9**(9): p. 503-511.

8. Coday, B.D. and T.Y. Cath, *Forward osmosis: Novel desalination of produced water and fracturing flowback.* Journal: American Water Works Association, 2014. **106**(2).

9. Pichtel, J., *Oil and gas production wastewater: Soil contamination and pollution prevention.* Applied and Environmental Soil Science, 2016. **2016**.

10. Olmstead, S.M., et al., *Shale gas development impacts on surface water quality in Pennsylvania.* Proceedings of the National Academy of Sciences, 2013. **110**(13): p. 4962-4967.

11. Brittingham, M.C., et al., *Ecological risks of shale oil and gas development to wildlife, aquatic resources and their habitats.* Environmental science & technology, 2014. **48**(19): p. 11034-11047.

12. Scanlon, B.R., et al., *Managing basin-scale fluid budgets to reduce injection-induced seismicity from the recent US shale oil revolution.* Seismological Research Letters, 2019. **90**(1): p. 171-182.

13. Marshall, A., *New wave of injection wells on the way in Ohio for fracking waste.* The Plain Dealer, 2012.

14. Tavakkoli, S., et al., *Shale gas produced water management using membrane distillation: An optimization-based approach.* Resources, Conservation and Recycling, 2020. **158**: p. 104803.

15. Tong, T. and M. Elimelech, *The global rise of zero liquid discharge for wastewater management: drivers, technologies, and future directions.* Environmental science & technology, 2016. **50**(13): p. 6846-6855.

16. Yaqub, M. and W. Lee, *Zero-liquid discharge (ZLD) technology for resource recovery from wastewater: A review.* Science of the total environment, 2019. **681**: p. 551-563.

17. Vane, L.M., *Water recovery from brines and salt-saturated solutions: operability and thermodynamic efficiency considerations for desalination technologies.* Journal of Chemical Technology and Biotechnology, 2017.

18. Shaffer, D.L., et al., *Desalination and reuse of high-salinity shale gas produced water: drivers, technologies, and future directions.* Environmental science & technology, 2013. **47**(17): p. 9569-9583.

19. Kaplan, R., et al., *Assessment of desalination technologies for treatment of a highly saline brine from a potential CO2 storage site.* Desalination, 2017. **404**: p. 87-101.

20. Singh, R., *Membrane technology and engineering for water purification: application, systems design and operation*. 2014: Butterworth-Heinemann.

21. Sarbatly, R. and C.-K. Chiam, *Evaluation of geothermal energy in desalination by vacuum membrane distillation.* Applied Energy, 2013. **112**: p. 737-746.

22. Dow, N., et al., *Pilot trial of membrane distillation driven by low grade waste heat: Membrane fouling and energy assessment.* Desalination, 2016. **391**: p. 30-42.

23. Basile, A. and C. Charcosset, *Integrated membrane systems and processes*. 2016: Wiley Online Library.

24. Cath, T.Y., V.D. Adams, and A.E. Childress, *Experimental study of desalination using direct contact membrane distillation: a new approach to flux enhancement.* Journal of Membrane Science, 2004. **228**(1): p. 5-16.

25. Shirazi, M., *Desalination of saline water using direct contact membrane distillation.* J. Appl. Chem. Res, 2011. **17**: p. 28-36.

26. Chen, W., et al., *High-flux water desalination with interfacial salt sieving effect in nanoporous carbon composite membranes.* Nature nanotechnology, 2018. **13**(4): p. 345-350.

27. Kesieme, U.K., et al., *Recovery of water and acid from leach solutions using direct contact membrane distillation.* Water science and technology, 2014. **69**(4): p. 868-875.

28. Xie, M., et al., *A forward osmosis–membrane distillation hybrid process for direct sewer mining: system performance and limitations.* Environmental science & technology, 2013. **47**(23): p. 13486-13493.

29. Gryta, M., K. Karakulski, and A. Morawski, *Purification of oily wastewater by hybrid UF/MD.* Water research, 2001. **35**(15): p. 3665-3669.

30. Kim, J., et al., *Osmotically enhanced dewatering-reverse osmosis (OED-RO) hybrid system: Implications for shale gas produced water treatment.* Journal of Membrane Science, 2018. **554**: p. 282-290.

31. Atia, A.A., N.Y. Yip, and V. Fthenakis, *Pathways for minimal and zero liquid discharge with enhanced reverse osmosis technologies: Module-scale modeling and techno-economic assessment.* Desalination, 2021. **509**: p. 115069.

32. Park, K. and D.R. Yang, *Cost-based feasibility study and sensitivity analysis of a new draw solution assisted reverse osmosis (DSARO) process for seawater desalination.* Desalination, 2017. **422**: p. 182-193.

33. Kim, J., D.I. Kim, and S. Hong, *Analysis of an osmotically-enhanced dewatering process for the treatment of highly saline (waste) waters.* Journal of Membrane Science, 2018. **548**: p. 685-693.

34. Peters, C.D. and N.P. Hankins, *Osmotically assisted reverse osmosis (OARO): Five approaches to dewatering saline brines using pressure-driven membrane processes.* Desalination, 2019. **458**: p. 1-13.

35. Chen, X. and N.Y. Yip, *Unlocking high-salinity desalination with cascading osmotically mediated reverse osmosis: Energy and operating pressure analysis.* Environmental science & technology, 2018. **52**(4): p. 2242-2250.

36. Bartholomew, T.V., et al., *Osmotically assisted reverse osmosis for high salinity brine treatment.* Desalination, 2017. **421**: p. 3-11.

37. Bouma, A.T., *Split-feed counterflow reverse osmosis for brine concentration.* Desalination, 2018. **445**: p. 280-291.

38. Ranade, V.V. and V.M. Bhandari, *Industrial wastewater treatment, recycling and reuse*. 2014: Butterworth-Heinemann.

39. Krishna, H.J., *Introduction to desalination technologies.* Texas water development, 2004. **2**.

40. Barbot, E., et al., *Spatial and temporal correlation of water quality parameters of produced waters from Devonian-age shale following hydraulic fracturing.* Environmental science & technology, 2013. **47**(6): p. 2562-2569.

41. Kondash, A.J., E. Albright, and A. Vengosh, *Quantity of flowback and produced waters from unconventional oil and gas exploration.* Science of the Total Environment, 2017. **574**: p. 314-321.

42. Clark, C.E. and J.A. Veil, *Produced water volumes and management practices in the United States*. 2009, Argonne National Lab.(ANL), Argonne, IL (United States).

43. Lutz, B.D., A.N. Lewis, and M.W. Doyle, *Generation, transport, and disposal of wastewater associated with Marcellus Shale gas development.* Water Resources Research, 2013. **49**(2): p. 647-656.

44. Ellsworth, W.L., *Injection-induced earthquakes.* Science, 2013. **341**(6142).

45. Horton, S., *Disposal of hydrofracking waste fluid by injection into subsurface aquifers triggers earthquake swarm in central Arkansas with potential for damaging earthquake.* Seismological Research Letters, 2012. **83**(2): p. 250-260.

46. Keranen, K.M., et al., *Sharp increase in central Oklahoma seismicity since 2008 induced by massive wastewater injection.* Science, 2014. **345**(6195): p. 448-451.

47. Lokare, O.R., et al., *Importance of feed recirculation for the overall energy consumption in membrane distillation systems.* Desalination, 2018. **428**: p. 250-254.

48. Swaminathan, J., *Design and operation of membrane distillation with feed recirculation for high recovery brine concentration.* Desalination, 2018. **445**: p. 51-62.

49. He, F., J. Gilron, and K.K. Sirkar, *High water recovery in direct contact membrane distillation using a series of cascades.* Desalination, 2013. **323**: p. 48-54.

50. Alkhudhiri, A., N. Darwish, and N. Hilal, *Membrane distillation: a comprehensive review.* Desalination, 2012. **287**: p. 2-18.

51. Swaminathan, J., et al., *Energy efficiency of permeate gap and novel conductive gap membrane distillation.* Journal of Membrane Science, 2016. **502**: p. 171-178.

52. Drioli, E., A. Ali, and F. Macedonio, *Membrane distillation: Recent developments and perspectives.* Desalination, 2015. **356**: p. 56-84.

53. Summers, E.K. and H.A. Arafat, *Energy efficiency comparison of single-stage membrane distillation (MD) desalination cycles in different configurations.* Desalination, 2012. **290**: p. 54-66.

54. Swaminathan, J., H.W. Chung, and D.M. Warsinger, *Energy efficiency of membrane distillation up to high salinity: Evaluating critical system size and optimal membrane thickness.* Applied energy, 2018. **211**: p. 715-734.

55. El Amali, A., S. Bouguecha, and M. Maalej, *Experimental study of air gap and direct contact membrane distillation configurations: application to geothermal and seawater desalination.* Desalination, 2004. **168**: p. 357.

56. Alklaibi, A.M. and N. Lior, *Comparative study of direct-contact and air-gap membrane distillation processes.* Industrial & engineering chemistry research, 2007. **46**(2): p. 584-590.

57. Eykens, L., et al., *How to select a membrane distillation configuration? Process conditions and membrane influence unraveled.* Desalination, 2016. **399**: p. 105-115.

58. Khalifa, A.E., *Water and air gap membrane distillation for water desalination–an experimental comparative study.* Separation and Purification Technology, 2015. **141**: p. 276-284.

59. Cheng, L., et al., *Comparative study of air gap and permeate gap membrane distillation using internal heat recovery hollow fiber membrane module.* Desalination, 2018. **426**: p. 42-49.

60. Noamani, S., et al., *Modeling of Air-Gap Membrane Distillation and Comparative Study with Direct Contact Membrane Distillation.* Industrial & Engineering Chemistry Research, 2020. **59**(50): p. 21930-21947.

61. Kesieme, U.K., et al., *Economic analysis of desalination technologies in the context of carbon pricing, and opportunities for membrane distillation.* Desalination, 2013. **323**: p. 66-74.

62. Al-Obaidani, S., et al., *Potential of membrane distillation in seawater desalination: thermal efficiency, sensitivity study and cost estimation.* Journal of Membrane Science, 2008. **323**(1): p. 85-98.

63. Sirkar, K.K. and L. Song, *Pilot-scale studies for direct contact membrane distillation-based desalination process*. 2009: US Department of the Interior, Bureau of Reclamation.

64. Schwantes, R., et al., *Techno-economic comparison of membrane distillation and MVC in a zero liquid discharge application.* Desalination, 2018. **428**: p. 50-68.

65. Hitsov, I., et al., *Economic modelling and model-based process optimization of membrane distillation.* Desalination, 2018. **436**: p. 125-143.

66. Tavakkoli, S., et al., *A techno-economic assessment of membrane distillation for treatment of Marcellus shale produced water.* Desalination, 2017. **416**: p. 24-34.

67. Carrero-Parreño, A., et al., *Optimization of multistage membrane distillation system for treating shale gas produced water.* Desalination, 2019. **460**: p. 15-27.

68. Bartholomew, T.V., et al., *Cost optimization of high recovery single stage gap membrane distillation.* Journal of Membrane Science, 2020. **611**: p. 118370.

69. Lokare, O.R., et al., *Integrating membrane distillation with waste heat from natural gas compressor stations for produced water treatment in Pennsylvania.* Desalination, 2017. **413**: p. 144-153.

70. Drud, A.S., *CONOPT—a large-scale GRG code.* ORSA Journal on computing, 1994. **6**(2): p. 207-216.

71. Sievers, M. and J.H. Lienhard, *Design of flat-plate dehumidifiers for humidification–dehumidification desalination systems.* Heat transfer engineering, 2013. **34**(7): p. 543-561.

72. Swaminathan, J., *Numerical and experimental investigation of membrane distillation flux and energy efficiency*. 2014, Massachusetts Institute of Technology.

73. Lin, S., N.Y. Yip, and M. Elimelech, *Direct contact membrane distillation with heat recovery: Thermodynamic insights from module scale modeling.* Journal of membrane science, 2014. **453**: p. 498-515.

74. Warsinger, D.M., et al., *Scaling and fouling in membrane distillation for desalination applications: a review.* Desalination, 2015. **356**: p. 294-313.

75. Guan, G., et al., *Achieving sustainable operation for hypersaline membrane distillation applications: A novel strategy based on the critical Reynolds number.* Desalination, 2021. **499**: p. 114833.

76. Warsinger, D.M., E.W. Tow, and J. Swaminathan, *Theoretical framework for predicting inorganic fouling in membrane distillation and experimental validation with calcium sulfate.* Journal of Membrane Science, 2017. **528**: p. 381-390.

77. Gregory, K.B., R.D. Vidic, and D.A. Dzombak, *Water management challenges associated with the production of shale gas by hydraulic fracturing.* Elements, 2011. **7**(3): p. 181-186.

78. Vidic, R.D., et al., *Impact of shale gas development on regional water quality.* Science, 2013. **340**(6134): p. 1235009.

79. Paugh, L.O. *Marcellus shale water management challenges in Pennsylvania*. in *SPE Shale Gas Production Conference*. 2008. OnePetro.

80. Brantley, S.L., et al., *Water resource impacts during unconventional shale gas development: The Pennsylvania experience.* International Journal of Coal Geology, 2014. **126**: p. 140-156.

81. Obkirchner, G.E., *Evaluating the Economic Impacts of Groundwater Pumping for Hydraulic Fracturing on Aquifer Stakeholders in the Eagle Ford Shale, Texas*. 2019.

82. Fontenot, B.E., et al., *An evaluation of water quality in private drinking water wells near natural gas extraction sites in the Barnett Shale Formation.* Environmental science & technology, 2013. **47**(17): p. 10032-10040.

83. Jackson, R.B., et al., *Increased stray gas abundance in a subset of drinking water wells near Marcellus shale gas extraction.* Proceedings of the National Academy of Sciences, 2013. **110**(28): p. 11250-11255.

84. Vengosh, A., et al., *A critical review of the risks to water resources from unconventional shale gas development and hydraulic fracturing in the United States.* Environmental science & technology, 2014. **48**(15): p. 8334-8348.

85. Burton Jr, G.A., et al., *Hydraulic "fracking": are surface water impacts an ecological concern?* Environmental Toxicology and Chemistry, 2014. **33**(8): p. 1679-1689.

86. Rassenfoss, S., *From flowback to fracturing: water recycling grows in the Marcellus shale.* Journal of Petroleum Technology, 2011. **63**(07): p. 48-51.

87. Veil, J.A., *Water management technologies used by Marcellus Shale Gas Producers*. 2010, Argonne National Lab.(ANL), Argonne, IL (United States).

88. Yazdan, M.M., et al., *Review on the evaluation of the impacts of wastewater disposal in hydraulic fracturing industry in the United States.* Technologies, 2020. **8**(4): p. 67.

89. Vane, L.M., *Water recovery from brines and salt-saturated solutions: operability and thermodynamic efficiency considerations for desalination technologies.* Journal of Chemical Technology & Biotechnology, 2017. **92**(10): p. 2506-2518.

90. Cheng, L.-H., P.-C. Wu, and J. Chen, *Numerical simulation and optimal design of AGMD-based hollow fiber modules for desalination.* Industrial & Engineering Chemistry Research, 2009. **48**(10): p. 4948-4959.

91. Mohammadi Shamlou, E., Vidic, R., Khanna, V., *Optimization-based Economic Comparison of Membrane Distillation Configurations for Application in Shale Gas Produced Water Treatment.* Desalination, 2021.

92. Swaminathan, J., *Unified framework to design efficient membrane distillation for brine concentration*. 2017, Massachusetts Institute of Technology.

93. Pangarkar, B.L. and M. Sane, *Performance of air gap membrane distillation for desalination of ground water and seawater*. World Academy of Science, Engineering, and Technology, 2011. **75**: p. 177-181.

94. Zhao, K., et al., *Experimental study of the memsys vacuum-multi-effect-membrane-distillation (V-MEMD) module*. Desalination, 2013. **323**: p. 150-160.

95. Gilron, J., L. Song, and K.K. Sirkar, *Design for cascade of crossflow direct contact membrane distillation.* Industrial & Engineering Chemistry Research, 2007. **46**(8): p. 2324-2334.

96. Chung, H.W., J. Swaminathan, and D.M. Warsinger, *Multistage vacuum membrane distillation (MSVMD) systems for high salinity applications.* Journal of Membrane Science, 2016. **497**: p. 128-141.

97. Summers, E. and J. Lienhard, *Cycle performance of multi-stage vacuum membrane distillation (MS-VMD) systems.* Proc. 2013 IDA World Congr. Desalin. Water Reuse, Tianjin, China, 2013.

98. Dudchenko, A.V., T.V. Bartholomew, and M.S. Mauter, *Cost optimization of multi-stage gap membrane distillation.* Journal of Membrane Science, 2021. **627**: p. 119228.

99. Lu, Y. and J. Chen, *Optimal design of multistage membrane distillation systems for water purification.* Industrial & Engineering Chemistry Research, 2011. **50**(12): p. 7345-7354.

100. Lee, J.-G., et al., *Performance modeling of direct contact membrane distillation (DCMD) seawater desalination process using a commercial composite membrane.* Journal of Membrane Science, 2015. **478**: p. 85-95.

101. Gryta, M., M. Tomaszewska, and A. Morawski, *Membrane distillation with laminar flow.* Separation and Purification Technology, 1997. **11**(2): p. 93-101.

102. Butkovskyi, A., et al., *Organic pollutants in shale gas flowback and produced waters: identification, potential ecological impact, and implications for treatment strategies.* Environmental science & technology, 2017. **51**(9): p. 4740-4754.

103. Conidi, C., et al., *Treatment of flue gas desulfurization wastewater by an integrated membrane-based process for approaching zero liquid discharge.* Membranes, 2018. **8**(4): p. 117.

104. Wales, M.D., et al., *Flue Gas Desulfurization (FGD) Wastewater Treatment Using Polybenzimidazole (PBI) Hollow Fiber (HF) Membranes.* Membranes, 2021. **11**(6): p. 430.

105. Mohamed, A., M. Maraqa, and J. Al Handhaly, *Impact of land disposal of reject brine from desalination plants on soil and groundwater.* Desalination, 2005. **182**(1-3): p. 411-433.

106. Panagopoulos, A. and K.-J. Haralambous, *Environmental impacts of desalination and brine treatment-Challenges and mitigation measures.* Marine Pollution Bulletin, 2020. **161**: p. 111773.

107. Angelini, P., et al., *Materials for separation technologies: Energy and emission reduction opportunities.* DOE, EERE Office, Washington, DC, 2005. **103**.

108. Shao, L., *Grand Challenges in Emerging Separation Technologies.* Frontiers in Environmental Chemistry, 2020. **1**: p. 3.

109. Vane, L., *Separations Versus Sustainability: There Is No Such Thing As a Free Lunch*, in *Sustainability in the Design, Synthesis and Analysis of Chemical Engineering Processes*. 2016, Elsevier. p. 35-65.

110. Jones, E., et al., *The state of desalination and brine production: A global outlook.* Science of the Total Environment, 2019. **657**: p. 1343-1356.

111. Ahunbay, M.G., S.B. Tantekin-Ersolmaz, and W.B. Krantz, *Energy optimization of a multistage reverse osmosis process for seawater desalination.* Desalination, 2018. **429**: p. 1-11.

112. Zhu, A., P.D. Christofides, and Y. Cohen, *Effect of thermodynamic restriction on energy cost optimization of RO membrane water desalination.* Industrial & Engineering Chemistry Research, 2008. **48**(13): p. 6010-6021.

113. El-Halwagi, M.M., *Synthesis of reverse-osmosis networks for waste reduction.* AIChE Journal, 1992. **38**(8): p. 1185-1198.

114. Lin, S. and M. Elimelech, *Staged reverse osmosis operation: Configurations, energy efficiency, and application potential.* Desalination, 2015. **366**: p. 9-14.

115. Mistry, K.H., et al., *Entropy generation analysis of desalination technologies.* Entropy, 2011. **13**(10): p. 1829-1864.

116. Bartholomew, T.V., N.S. Siefert, and M.S. Mauter, *Cost optimization of osmotically assisted reverse osmosis.* Environmental science & technology, 2018. **52**(20): p. 11813-11821.

117. Loeb, S. and M. Bloch, *Countercurrent flow osmotic processes for the production of solutions having a high osmotic pressure.* Desalination, 1973. **13**(2): p. 207-215.

118. Zhang, S. and T.-S. Chung, *Minimizing the instant and accumulative effects of salt permeability to sustain ultrahigh osmotic power density.* Environmental science & technology, 2013. **47**(17): p. 10085-10092.

119. Chou, S., R. Wang, and A.G. Fane, *Robust and high performance hollow fiber membranes for energy harvesting from salinity gradients by pressure retarded osmosis.* Journal of membrane science, 2013. **448**: p. 44-54.

120. Kim, Y.C. and M. Elimelech, *Adverse impact of feed channel spacers on the performance of pressure retarded osmosis.* Environmental science & technology, 2012. **46**(8): p. 4673-4681.

121. Song, X., Z. Liu, and D.D. Sun, *Energy recovery from concentrated seawater brine by thin-film nanofiber composite pressure retarded osmosis membranes with high power density.* Energy & Environmental Science, 2013. **6**(4): p. 1199-1210.

122. Straub, A.P., N.Y. Yip, and M. Elimelech, *Raising the bar: Increased hydraulic pressure allows unprecedented high power densities in pressure-retarded osmosis.* Environmental Science & Technology Letters, 2014. **1**(1): p. 55-59.

123. Shatat, M. and S.B. Riffat, *Water desalination technologies utilizing conventional and renewable energy sources.* International Journal of Low-Carbon Technologies, 2012. **9**(1): p. 1-19.

124. Kaplan, R., et al., *Assessment of desalination technologies for treatment of a highly saline brine from a potential CO 2 storage site.* Desalination, 2017. **404**: p. 87-101.

125. Jamil, M.A. and S.M. Zubair, *On thermoeconomic analysis of a single-effect mechanical vapor compression desalination system.* Desalination, 2017. **420**: p. 292-307.

126. El-Dessouky, H., H. Ettouney, and F. Al-Juwayhel, *Multiple effect evaporation—vapour compression desalination processes.* Chemical Engineering Research and Design, 2000. **78**(4): p. 662-676.

127. Darwish, M. and H.K. Abdulrahim, *Feed water arrangements in a multi-effect desalting system.* Desalination, 2008. **228**(1-3): p. 30-54.

128. Khademi, M., M. Rahimpour, and A. Jahanmiri, *Simulation and optimization of a six-effect evaporator in a desalination process.* Chemical Engineering and Processing: Process Intensification, 2009. **48**(1): p. 339-347.

129. Al-Mutaz, I.S. and I. Wazeer, *Comparative performance evaluation of conventional multi-effect evaporation desalination processes.* Applied Thermal Engineering, 2014. **73**(1): p. 1194-1203.

130. Sayyaadi, H. and A. Saffari, *Thermoeconomic optimization of multi effect distillation desalination systems.* Applied Energy, 2010. **87**(4): p. 1122-1133.

131. Xue, J., et al., *Analysis of thermal properties on backward feed multieffect distillation dealing with high-salinity wastewater.* Journal of Nanotechnology, 2015. **2015**.

132. Druetta, P., P. Aguirre, and S. Mussati, *Optimization of multi-effect evaporation desalination plants.* Desalination, 2013. **311**: p. 1-15.

133. Sagharichiha, M., et al., *Simulation of a forward feed multiple effect desalination plant with vertical tube evaporators.* Chemical Engineering and Processing: Process Intensification, 2014. **75**: p. 110-118.

134. Esfahani, I.J., S. Lee, and C. Yoo, *Evaluation and optimization of a multi-effect evaporation–absorption heat pump desalination based conventional and advanced exergy and exergoeconomic analyses.* Desalination, 2015. **359**: p. 92-107.

135. Onishi, V.C., et al., *Shale gas flowback water desalination: Single vs multiple-effect evaporation with vapor recompression cycle and thermal integration.* Desalination, 2017. **404**: p. 230-248.

136. Aly, G., *Computer simulations of multiple-effect FFE-VC systems for water desalination.* Desalination, 1983. **45**(2): p. 119-131.

137. Jamil, M.A. and S.M. Zubair, *Design and analysis of a forward feed multi-effect mechanical vapor compression desalination system: An exergo-economic approach.* Energy, 2017. **140**: p. 1107-1120.

138. Jamil, M.A. and S.M. Zubair, *Effect of feed flow arrangement and number of evaporators on the performance of multi-effect mechanical vapor compression desalination systems.* Desalination, 2018. **429**: p. 76-87.

139. Nafey, A.S., H.E.S. Fath, and A.A. Mabrouk, *Thermoeconomic design of a multi-effect evaporation mechanical vapor compression (MEE–MVC) desalination process.* Desalination, 2008. **230**(1-3): p. 1-15.

140. Elsayed, M.L., et al., *Performance modeling of MED-MVC systems: Exergy-economic analysis.* Energy, 2019. **166**: p. 552-568.

141. Helal, A. and S. Al-Malek, *Design of a solar-assisted mechanical vapor compression (MVC) desalination unit for remote areas in the UAE.* Desalination, 2006. **197**(1-3): p. 273-300.

142. Lokiec, F. and A. Ophir. *The mechanical vapor compression: 38 years of experience*. in *IDA World Congress-Maspalomas, Gran Canaria, Spain*. 2007.

143. Towler, G. and R. Sinnott, *Chemical engineering design: principles, practice and economics of plant and process design*. 2012: Elsevier.

144. Garrett, D., *Chemical Engineering Economics Van Nostrand Reinhold.* New York, 1989.

145. Turton, R., et al., *Analysis, synthesis and design of chemical processes*. 2008: Pearson Education.

146. Karanikola, V., et al., *Economic performance of membrane distillation configurations in optimal solar thermal desalination systems.* Desalination, 2019. **472**: p. 114164.

147. Alsaadi, A.S., et al., *Modeling of air-gap membrane distillation process: A theoretical and experimental study.* Journal of membrane science, 2013. **445**: p. 53-65.

148. Hitsov, I., et al., *Full-scale validated Air Gap Membrane Distillation (AGMD) model without calibration parameters.* Journal of membrane science, 2017. **533**: p. 309-320.

149. Karanikola, V., et al., *Sweeping gas membrane distillation: numerical simulation of mass and heat transfer in a hollow fiber membrane module.* Journal of Membrane Science, 2015. **483**: p. 15-24.

150. García-Payo, M.d.C. and M.A. Izquierdo-Gil, *Thermal resistance technique for measuring the thermal conductivity of thin microporous membranes.* Journal of Physics D: Applied Physics, 2004. **37**(21): p. 3008.

151. Hitsov, I., et al., *Modelling approaches in membrane distillation: A critical review.* Separation and Purification Technology, 2015. **142**: p. 48-64.

152. Da Costa, A., A. Fane, and D. Wiley, *Spacer characterization and pressure drop modelling in spacer-filled channels for ultrafiltration.* Journal of membrane science, 1994. **87**(1-2): p. 79-98.

153. Winter, D., *Membrane distillation: A thermodynamic, technological and economic analysis*. 2015: Shaker Verlag.

154. Guillen, G. and E.M. Hoek, *Modeling the impacts of feed spacer geometry on reverse osmosis and nanofiltration processes.* Chemical Engineering Journal, 2009. **149**(1-3): p. 221-231.

155. El-Dessouky, H.T. and H.M. Ettouney, *Fundamentals of salt water desalination*. 2002: Elsevier.

156. Lu, Y.-Y., et al., *Optimum design of reverse osmosis system under different feed concentration and product specification.* Journal of membrane science, 2007. **287**(2): p. 219-229.

157. Park, C., et al., *Stochastic cost estimation approach for full-scale reverse osmosis desalination plants.* Journal of Membrane Science, 2010. **364**(1-2): p. 52-64.

158. Koutsou, C.P., S.G. Yiantsios, and A.J. Karabelas, *A numerical and experimental study of mass transfer in spacer-filled channels: Effects of spacer geometrical characteristics and Schmidt number*. Journal of Membrane Science, 2009. **326**(1): p. 234-251.